Effects of Topography on 3D Seismic Ground Motion Simulation with an Application to the Valley of Aburrá in Antioquia, Colombia

Sometido en cumplimiento parcial de los requisitos para

el título de

Doctor en Ingeniería

Doriam L Restrepo

Universidad EAFIT
Escuela de Ingeniería
Medellín

December, 2013

To my parents

Acknowledgements

I am deeply indebted to my advisor Professor Jacobo Bielak. He was not only available to discuss our projects and to come up with bright ideas and suggestions, but his kindnesses, respect, and human touch made this whole experience unique. Professor, you gave me the chance to join your group, little did I know the enormous impact that this experience was going to bring up, for that, my everlasting gratitude to you.

Special acknowledgments to the members of my doctoral committee: Prof. Jacobo Bielak (Committee Chair), Prof. David O' Hallaron, Prof. Irving Oppenheim, Prof. Juan Diego Jaramillo, and Dr. Enrique Bazán. I want to express my deepest gratitude to Prof. Juan Diego Jaramillo from Universidad EAFIT who not only showed confidence in me, but also presented me the field of Elastodynamics, and dedicated me hours discussing theoretical concepts and breaking down the math in such a way that still amazes me. I must thank also to Prof. Juan David Gómez from Universidad EAFIT. Juan David, you set this off. You brought the idea to come to Carnegie Mellon, and helped me to materialize it. Thanks for the several fruitful discussions, your support, and for all your sincere and honest advice. Most important, thanks for your friendship.

My parents and siblings were also a continuous source of support. My special thanks to my sister Llaneth who has always been ready to support me and to back me up in every possible way. To my niece Manuela, thanks for your truly and sincere love. This goal is also the result of strong bonds created along the way. Ana, I cannot begin to offer words to express my gratitude and appreciation for tirelessly assist me in this effort. You surely have had to endure during this process. I am deeply grateful for your love and encouragement. To my friends Yigit Isbiliroglu, Haydar Karaoglu, and Ricardo Taborda, thanks for your comments, suggestions and enormous patience. I would like to thank to the amazing staff at Universidad EAFIT, with special affection to Félix Londoño, Alberto Rodriguez García, Julian Vidal Valencia, and to the members of the Applied Mechanics Research Group. Thanks to the staff at CEE for their continue assistance specially to Maxine Leffard, Cornelia Moore, and Donna Marano. I want to express my gratitude to Universidad EAFIT, Carnegie Mellon University, COLCIENCIAS (the Colombian Institute of Science and Technology), DNP (the Colombian National Planning Department), and to the Colombian Fulbright Program for the institutional and financial support that they provided me. Many thanks to LASPAU at Harvard University with special gratitude to Lisa M. Tapiero for being a constant source of help and support during this study.

Abstract

This dissertation presents a numerical scheme based upon the finite element framework for the numerical modeling of earthquake-induced ground motion in the presence of realistic topographic variations of the Earth's crust. We show that by adopting a non-conforming meshing scheme for the numerical representation of the surficial topography we can obtain very accurate representations of earthquake induced ground motion in mountainous regions. From the computational point of view, our methodology proves to be accurate, efficient, and more importantly, it allows us to preserve the salient features of multi-resolution cubic finite elements. We implemented the non-conforming scheme for the treatment of realistic topographies into Hercules, the octree-based finite-element earthquake simulator developed by the Quake Group at Carnegie Mellon University. We tested the benefits of the strategy by benchmarking its results against reference examples, and by means of convergence analyses. Our qualitative and quantitative comparisons showed an excellent agreement between results. Moreover, this agreement was obtained using the same mesh refinement as in traditional flat-free simulations.

Our approach was tested under realistic conditions by conducting a comprehensive set of deterministic 3D ground motion numerical simulations in an earthquake-prone region exhibiting moderate-to-strong surficial irregularities known as the Aburrá Valley in Antioquia - Colombia. We proposed a $50 \times 50 \times 25$ km^3 volume to perform our simulations, and four $M_{\mathrm{w}} = 5$ rupture scenarios along a segment of the Romeral fault; a significant source of seismic activity of Colombia. We created and used the Initial Velocity Model of the Aburrá Valley region (IVM-AbV) which takes geology as a proxy for shear-wave velocity. Each earthquake model was simulated using three different models: (i) realistic 3D structure with realistic topography; (ii) realistic 3D structure without topography; and (iii) homogeneous half space with realistic topography. Our results show how topographic irregularities greatly modify the ground response. In particular, they highlight the importance of the combined interaction between source-effects, focusing, soft-soil conditions, and 3D topography. We provide quantitative evidence of this interaction and show that topographic amplification factors at some locations can be as high as 500 percent, while some other areas experience reductions. These are smaller than the amplifications, on the order of up to 100 percent.

Contents

Acknowledgements ii

Abstract iii

List of Tables vi

List of Figures vii

1 Introduction 1
- 1.1 Field and Instrumental Evidence . . . 4
- 1.2 Numerical Evidence . . . 8
- 1.3 Large-Scale Numerical Simulations . . . 14

2 Conceptual Framework and Strategy 18
- 2.1 Non-Conforming Meshing Scheme for Solid-to-Vacuum Interfaces . . . 22
- 2.2 Numerical Integration. Quadrature Rule Approach . . . 25
  - 2.2.1 Lumped Mass Matrices . . . 26
- 2.3 Numerical Integration. Virtual Topography Scheme . . . 27
  - 2.3.1 Lumped Mass Strategy . . . 30

3 2D Verification. Partial integration Scheme. 32
- 3.1 Semi-Circular Hill over Homogeneous Half-Space . . . 34
- 3.2 Semi-Circular Hill plus Parabolic Mountain over Homogeneous Half-Space 38

4 3D Verification. Virtual Topography Scheme 43
- 4.1 Gaussian Hill. . . . 44
- 4.2 Hermitian Ridge . . . 48
- 4.3 Convergence Analysis . . . 50

5 The Region of Interest: The Aburrá Valley (Antioquia – Colombia) 54
- 5.1 Colombian Seismotectonic Setting . . . 54
- 5.2 The Aburrá Valley Seismic Setting . . . 56

5.3 Source and Material Models 59
5.3.1 Romeral Fault Rupture Scenarios 59
5.3.2 3D Seismic Velocity Model 60

6 3D Earthquake Ground Motion Simulations of The Aburrá Valley Region 65
6.1 Regional Effects 67
6.1.1 Wavefields Propagation 67
6.1.2 Topographic Amplification Factors 72
6.2 Local Response 84
6.2.1 Synthetic Waveforms along Vertical Sections 85
6.2.2 Topographic Amplification Factors on Vertical Sections 89
6.3 Synthetic Time Histories at RAVA and RAM Stations 92
6.3.1 Time Synthetics 93
6.3.2 Topographic Amplification Factors at RAVA-RAM Stations 94

7 Concluding Remarks 98

A Synthetics of ground motion at the stations of the RAM and RAVA seismic networks. Earthquake source No:1 102

Bibliography 105

List of Tables

2.1 Integration error bounds. After 1D expression from Zohdi and Wriggers (2001) 26

4.1 Mesh refinements for convergence analyses 52
4.2 Convergence rates for the VT and the Staircase-based mesh methods 52

5.1 Double-couple point sources parameters 60

6.1 Summary of simulation parameters and input data. 67

List of Figures

1.1 Symmetric infinite wedge under SH wave incidence . . . 13
1.2 Surface amplitudes for a circular-arc topography . . . 14

2.1 Nonconforming unstructured octant-mesh . . . 23
2.2 Cube to tetrahedra partition . . . 28

3.1 Semi-circular hill over homogeneous half-space . . . 34
3.2 Semi-circular hill - Enlarged view . . . 35
3.3 Semi-circular hill - Time histories . . . 35
3.4 Semi-circular hill - PGD . . . 36
3.5 Semi-Circular hill - Fourier spectral amplitudes . . . 37
3.6 Parabolic mountain plus Semi-circular hill . . . 38
3.7 Parabolic mountain plus Semi-circular hill - Enlarged view . . . 38
3.8 Parabolic Mountain plus Semi-circular Hill - Time histories (a) . . . 39
3.9 Parabolic Mountain plus Semi-circular Hill - Time histories (b) . . . 40
3.10 Parabolic mountain plus Semi-circular hill - PGD . . . 41
3.11 Parabolic mountain plus Semi-circular hill - Fourier spectral amplitudes . . . 41

4.1 Gaussian mountain subjected to a vertically incident SV wave . . . 44
4.2 Gaussian mountain - VT mesh . . . 45
4.3 Gaussian mountain - Time histories . . . 46
4.4 Hermitian ridge subjected to a vertically incident P-wave . . . 48
4.5 Hermitian ridge - VT mesh . . . 49
4.6 Hermitian ridge - Fourier amplitudes . . . 49
4.7 Hermitian ridge - Time histories . . . 50
4.8 Convergence rates for the Gaussian mountain and the Hermitian ridge . . . 51

5.1 Colombia's major tectonic domains . . . 57
5.2 Region of interest . . . 61
5.3 Map of surface shear-wave velocity . . . 63

6.1 Snapshots of the vertical component of velocity. Event 1 . . . 69
6.2 Snapshots of the vertical component of velocity. Event 2 . . . 71
6.3 Snapshots of the vertical component of velocity. Event 3 . . . 73
6.4 Snapshots of the vertical component of velocity. Event 4 . . . 74

6.5 PGV maps for events 1, and 2 77
6.6 PGV maps for events 3, and 4 78
6.7 PGA maps for events 1, and 2 80
6.8 PGA maps for events 3, and 4 81
6.9 Envelope of topographic amplification factors 83
6.10 Waveforms for vertical section 20N-20N 86
6.11 Waveforms for vertical section 30N-30N 88
6.12 Waveforms for vertical section 40N-40N 89
6.13 Topographic amplification factors along vertical sections 90
6.14 RAM and RAVA stations locations 92
6.15 Synthetic time histories from event 1 at RAVA and RAM stations 93
6.16 Topographic amplification factors from the RAVA and RAM stations 95
6.17 Topographic amplification maps from RAM and RAVA synthetic stations . 96

A.1 Time histories of the RAM and RAVA stations due to source 1 104

Chapter 1

Introduction

Seismic studies usually divide the influencing factors of earthquake ground motion into source, path, and site effects. This division, although arbitrary, has proven useful for the understanding of seismic ground motion. From these three factors, the so-called site effects have been widely accepted as major contributors to seismic wave amplification. This is explained in part by the uneven distribution of damage reported after large earthquakes (e.g., the Loma Prieta 1989, the Northridge 1994, the Kobe 1995), and by the well known sediment amplification usually explained numerically by one-dimensional (1D) soils models. Indeed, assuming only impedance contrast effects from a stack of horizontal homogeneous layers subjected to a vertically incident plane wave, proved to give good results in many cases (Satoh et al., 1995). 1D modeling has certainly shed light on the impact of soft soil deposits on ground motion amplification, and has propelled the large variety of soil classifications in current seismic standards. 1D modeling however, represents in many cases an oversimplification which can fail dramatically in its predictions when used in more general scenarios. Today, it is widely accepted that changes in amplitude, frequency content, and spatial distribution of the free-surface wave fields are not limited to impedance contrast effects. Wave field interaction with material interfaces, basin geometry, and the three-dimensional nature of the problem further change the seismic response and damage

distribution of a site. Moreover, man-made structures i.e., soil-, and city-structure interaction can dramatically change the spatial distribution of ground motion.

A large variety of site effects influence the ground motion. Some of these effects manifest themselves only after the occurrence of large earthquakes. For instance, instrumental evidence after the Northridge earthquake reports that amplifications of the main shock were up to a factor of two smaller than those of the aftershocks, which implies significant nonlinearity during the main event (Field et al., 1997). The 17 January 1995 Hyogo-ken Nanbu earthquake, and the 1992 Landers aftershock sequence are examples that exhibited anomalous bands of damage clearly linked to basin-edge effects (e.g., Field, 1996; Pitarka et al., 1998). Basin-edge effect are consequence of focusing and constructive interference of waves originated at strong lateral discontinuities (Moczo and Bard, 1993). A similarly site effect triggering anomalous ground motion is subsurface focusing (e.g., Baher et al., 2002; Baher and Davis, 2003). Here, multipathing and focusing effects emerge from sharp subsurface structure instead. Gao et al. (1996) identifies subsurface focusing as largely responsible for the band of damage parallel to the Santa Monica mountains during the Northridge earthquake. Specifically, deeper geologic structures act as acoustic lenses, and consequently generate high amplification and surprisingly concentrated damage (Davis et al., 2000).

Another geometry-related factor of considerable significance is surface topography. To anticipate that surface topography might drive important modifications to the ground motion is, on the other hand, more intuitive than the foregoing factors. Ever since its first description the main features of topography effects have been well acknowledged. In general, field records exhibit a zone of amplification that takes place near mountain tops at frequencies corresponding to wavelengths comparable with the mountain's width, and within the range of frequencies of engineering interest 1 to 20 Hz. Reduction zones occur near the bottom or at concave topographic features such as canyons and hill toes. Finally, complex patterns

of amplification/de-amplification with significant differential motions along the slopes are also expected (e.g., Geli et al., 1988; Assimaki et al., 2005a; Maufroy et al., 2012). According to Bard (1997) these topographic effects are rather sensitive to: i) the incident angle, ii) focusing/defocusing effects of seismic waves along the mountain surface, and iii) the interference patterns between direct and diffracted waves. Numerical results are qualitatively consistent with instrumental evidence. Models provide comparable results in terms of the frequency at which maximum amplification occurs and its spatial distribution. There are, however, significant differences with respect to the levels of anticipated ground motion. Some studies report amplitudes that go up to $10\times$ the theoretical estimates. Among the sources of discrepancy, some authors attribute these to 3D effects (e.g., Bouchon and Barker, 1996), soil stratigraphy and material heterogeneity (e.g., Assimaki et al., 2005a), and neighbouring topography (e.g., Geli et al., 1988).

Consequently, seismic effects by surface topography although well documented are still not fully understood. The large number of factors that in addition to the merely geometric changes add up to aggravate the ground motion in mountainous regions call for more general approaches. 3D numerical simulations appear then as important candidates to assess wave field variations especially in regions lacking strong motion information. Large-scale earthquake simulations must capture the most important aspects at the rupture zone, the variations of the wave fields in their transit through the crustal structure, the effects of the near-surface velocity gradient as well as surface topography.

The main objective of this dissertation is to develop an efficient and accurate numerical framework based on Hercules (Tu et al., 2006); the finite element code developed by the Quake group, for solving end-to-end earthquake simulations considering the presence of realistic topography and to apply it to a realistic situation in the Aburrá Valley in Colombia. Our first task is to construct the velocity model for the region, and then seek answers to the following questions:

- To what extent does actual topography influence the amplitudes, frequency characteristics, spatial distribution, and duration of the ground motion during earthquakes?
- How large are the variations in the amplitudes of the ground motion in the presence of topography when these are compared with traditional flat-free surface models?
- How sensitive are the topographic effects to the focal mechanism exhibited by the source?

As mentioned, in this thesis the application will be focused on the Aburrá Valley region (Colombia). The valley is a moderate intra-mountain depression located at the north end of the central range of the Colombian Andes. According to the national seismic code the region is considered to have a moderate seismic hazard (NSR-10, 2010). Geological evidence, however, suggests important tectonic activity along its main structural systems (GSM, 2006). Residual soils and hill-slope deposits occupy most of the valley slopes. The elongated narrow region has a total length of 60 km. It expands at the city of Medellín reaching about 7 km across, narrowing down again 18 km north-east following the river's natural course. The north and east parts of the valley are surrounded by older erosion structures known as the Santa Elena (2750 m.a.s.l) and the San Pedro (2800 m.a.s.l) land surfaces (Aristizábal et al., 2005). The valley houses about 3.2 million people. This corresponds to 7% of the country's population. The slopes of the mountains are the zones that compose most of the residential and development sites of the region.

1.1 Field and Instrumental Evidence

A large number of catastrophic earthquakes have shown a clear pattern of damage suffered by buildings located at the top of mountainous regions when compared with similar structures in flat zones. Classical examples of macroseismic observations are: the Lambesc

earthquake (1909 France), the Friuli earthquake (1976 Italy), the Irpina earthquake (1980 Italy), the Egion earthquake (1995 Greece), and the Athens (1999 Greece) earthquake (e.g., Paolucci, 2002). The L'Aquila (2009 Italy), and the Haiti (2010 Haiti) earthquake appear also as recent examples of anomalous amplifications and severe structural damage at the top and/or steep slopes of the hills (e.g., Çelebi et al., 2010; Hough et al., 2011).

Data recorded after the occurrence of explosions or seismic events of large magnitude provide crucial information regarding the factors that influence ground motion in mountainous regions. Even though the first strong motion accelerogram was recorded after the 10 March 1933 Long Beach, California earthquake (Trifunac, 2012), the first quantitative *hints* regarding the impact of topography were stumbled upon in 1968 after the Nevada Test Site (NTS) nuclear detonation (Davis and West, 1973). NTS events were recorded by instruments (not intended to study the impact of topography) deployed in and around the city of Tonopah, Nevada. Results from stations deployed on the top of the mountains exhibited larger amplifications than those placed in the city (flat area). More compelling evidence came three years later by the $\mathrm{M_L}$ 6.4 1971 San Fernando earthquake. The unexpectedly large peak ground acceleration $\mathrm{PGA} = 1.25\mathrm{g}$ (Trifunac and Hudson, 1971) registered at a site located on a sharp ridge near the Pacoima Dam (CA) abutment was promptly related to topographic amplification. Specifically, Boore (1972) identified wavelengths of predominant seismic energy of the same order as the dimensions of the topographic structure, which implies significant effects at the crest of the mountain.

The first data set exposing topographic amplification in a populated urban center was presented by Çelebi (1987) five months after the $\mathrm{M}_L = 7.8$ Central Chile earthquake. Spectral ratios derived from field experiments in Viña del Mar showed that amplifications from both topographic asperities and geologic variations took place at the ridges of Canal Beagle during the main event and the aftershocks. The frequency-dependent amplification correlates closely with the excessive level of damage experienced in buildings located throughout the

ridges after the main event. The 1 October 1987 Whittier Narrows ($M_L = 5.9$), California earthquake is another case in which topographic effects were detected in a metropolitan area. As an example, Kawase and Aki (1990) report a significant concentration of damage in buildings located on the slopes of the hills in the northern part of the city of Whittier (CA). The directional distribution of energy presents a direct correlation with a dominant incident SV wave. Moreover, numerical findings show that amplification is nearly independent of the fault type. Thus, the authors concluded that amplifications of critically incident vertical shear waves from topographic irregularities could have triggered the non-conventional level of damage experienced. Combined effects of critically incident waves and topographic irregularities have been also reported by other studies (e.g., Nava et al., 1989; Aki, 1993).

The 1989 Loma Prieta, and the 1994 Northridge earthquakes revealed also important ground amplifications consistent with the surface topography phenomenon (e.g., Hartzell et al., 1994; Spudich et al., 1996; Bouchon and Barker, 1996). Hartzell et al. (1994) conducted studies of aftershocks of the Loma Prieta earthquake recorded from a set of seven, three-component seismographs deployed on the Robinwood Ridge (CA). Results obtained using correlation-techniques, particle diagrams, and spectral ratios, presented a topographic effect in the 1.0 to 3.0 Hz range with amplification from 1.5 up to 4.5. Spudich et al. (1996) conducted a similar study using aftershocks of the 1994 Northridge earthquake registered on a mild hill (15m high) located at the Tarzana site (CA), and reported a top/base amplification of 4.5 at 3.2 Hz. The 3.2Hz resonant frequency is in good agreement with theoretical estimates (e.g., Bouchon, 1973); however, the 4.5 amplitude does not correlate with the hill's shape ratio (0.19). This reveals an interaction between the irregular ground surface and the three-dimensional geological structure of the site.

Several examples of seismic activity worldwide also highlight the relevance of site effects from topographic irregularities. As examples of these, Lovati et al. (2011) presents site

response analyses for the Narni ridge (Italy) by analyzing 642 seismic events, most of them related with the 2009 L'Aquila sequence. Results from SSR (standard spectral ratio), and HVSR (horizontal over vertical spectral ratio) exhibited topographic site effects in the 3-4.5 Hz range, with amplifications of up to 4.5 in the minor direction on the mountain. Maximum amplifications along the perpendicular direction of the mountain are consistent with other studies (e.g., Buech et al., 2010). The 1995 Kozani earthquake (Greece) brought to evidence serious damages in structures placed on the hills (Nguyen and Gatmiri, 2007). Moderate to severe damages were reported on the hill of Nocera Umbra (Italy) as a consequence of the $\mathrm{M_w} = 5.7$ and the $\mathrm{M_w} = 6.0$ Umbria–Marche earthquakes of 1997 September 26 (Donati et al., 2001). It is worth to mention that even when topographic amplification of 4 were reported, the poor quality construction of the historical centre might have played an important role in the level of damage reported (e.g., Pischiutta et al., 2010).

Topographic effects in the amplitudes and frequency content of the ground motion along hill slopes was also observed by Davis and West (1973); LeBrun et al. (1999),and Buech et al. (2010). Of particular importance, due to the large values of amplification obtained, is the seismic field experiment conducted by Buech et al. (2010). These authors make use of data gathered from a seismic array placed at an isolated ridge in the Southern Alps of New Zealand. Their results present amplifications at the crest of the ridge as high as $10\times$ compared to the ground motion at the foothill. The largest peak ground values were obtained in the mountain minor axis (perpendicular to the elongation of the hill). The vertical component on the other hand, exhibited the smallest peak ground motion. The authors highlight also the key role of topographic amplifications on the overall stability and degradation of rock blocks at the slopes of the mountain. Other experimental studies conducted under similar field conditions report amplification factors of 2 or 3 (e.g., Pedersen et al., 1994; Chávez-García et al., 1996). The reason for the differences in the level of amplification reported is still unknown (LeBrun et al., 1999).

1.2 Numerical Evidence

Ever since the first instrumental observations revealed the effects of surface topography on the characteristics of ground motion, scientists started to unfold the basic features of the phenomenon by analytically studying modest topographic configurations. Among these early approaches, Gilbert and Knopoff (1960) exposed the seismic-wave topographic scattering in 2D topographic profiles using the Born approximation. The 3D extension was presented later on by Hudson (1967). This approach was applied to study small slope cavities or inclusions at the free surface of a half-space. This form of first-order approximation method proved to be in good agreement with early instrumental findings. Perturbation methods however, are restricted to zones away from the topographic irregularity, which precludes its use for more general estimates. Prompted by observations of the 1971 San Fernando earthquake, Boore (1972, 1973) conducted the first finite-difference (FD) analysis focused at presenting numerical evidence of the influence of local topography on the intense PGA recorded at the Pacoima Dam area. The site was characterized as a 2D model, and only SH-waves at a fixed incident angle was considered. Because the surface fault passes beneath the site the SH plane wave approximation is difficult to satisfy since it ignores the significant contribution of free surface waves (Trifunac and Hudson, 1971). Despite the oversimplifications of the model, and qualitative nature of its findings, Boore's results are in general agreement with observations, and constitute one of the first set of numerical evidence linked with topographic site effects. Quantitative findings were presented by Bouchon (1973) by synthesizing results obtained by the Aki-Larner technique (Aki and Larner, 1970). He considered a complete set of P, SV, and SH obliquely incident waves acting on relatively realistic topographic profiles. The main findings were a systematic amplification at the top of about 50% for normal P-, normal S-, and the vertical component of P-incident waves respectively. More significant amplifications (100%) were also reported for the horizontal component of obliquely incident SV waves. An attenuation zone along

the flanks of the topographies was also consistently found.

The Aki-Larner technique was also utilized by Bard (1982), and Geli et al. (1988) in an effort to explain discrepancies between field observations and numerical findings, as well as to give new insights into the scattering of seismic waves by the presence of curved surfaces. The use of the Aki-Larner technique allowed the consideration of more realistic conditions in terms of the geometry of the topographic profiles, type of incoming waves, angles of incidence, internal layering, and neighbouring topography. Findings regarding the role of the type of incident wave in the characteristics of ground motion reveal that the pattern of amplification exhibits a larger effect on secondary (S) waves than for primary (P) waves. Furthermore, when these waves are obliquely incident, the expected zone of amplification at the crest is observed, although shifted toward the side of the ridge opposite to the upcoming waves. Mountain slopes in general undergo either amplifications or reductions depending on the station location, although the differential motion in those zones is always important as a result of the rapidly varying amplitude and phase. Subsurface layering on the other hand, complicates matters drastically. Surprisingly, its effects on crest/base amplification appear to be smaller than those generated by neighbouring topography (Geli et al., 1988).

Inherent inadequacies of the Aki-Larner technique to simulate locally upcoming waves precludes its use in large slope configurations topographies (Sánchez-Sesma and Campillo, 1991). In the past, numerous alternative methods were proposed to solve this deficiency. It appears that since the early 1980s, integral equation (IEM) based techniques i.e., the direct boundary element method (DBEM), or the indirect boundary element method (IBEM) were the dominant strategies for solving scattering problems caused by simple topographic irregularities (e.g., Sánchez-Sesma, 1983; Gaffet and Bouchon, 1989; Sánchez-Sesma and Campillo, 1991; Reinoso et al., 1997; Luzón et al., 1997). By approximating the scattering field of a vertically incident P-wave by wave functions that are solutions of the Navier's

equations, Sánchez-Sesma (1983) proves that the vertical component of motion at the tip of a symmetrical ridge exhibits amplifications larger than $3\times$ the amplitude of the incident wave. In the same direction, Gaffet and Bouchon (1989) investigate the effect of the steepness of a gentle 2D hill to vertically incident P-, and SV-waves, as well as the effect to an internal explosion. Their results present a sharp amplification at the ridge. The level of amplification is larger for the SV case (3.1 for a shape ratio $h/l = 0.5$), which is in agreement with other studies. Sánchez-Sesma and Campillo (1991) present the salient features of the topographic effects experienced by a 45^o triangular mountain, and a semi-elliptical mountain subjected to obliquely incident P- and SV-waves. Results for the triangular mountain exhibit an amplification of about 4 at the left rim. Surprisingly the same amplification level is found for the semi-elliptical mountain for a 30^o incident P-wave. Two highly idealized 3D mountains, namely, a dome-shaped mountain (Reinoso et al., 1997), and a horse-shoe-shaped mountain (Reinoso et al., 1997; Luzón et al., 1997) were analyzed by DBEM, and IBEM approaches respectively. Different incident plane waves scenarios were considered. Results from the simulations exhibit the already expected amplification pattern at the top of the mountains ($2\times$ the free-field value for SV-0^o). A consistently topographic effect was reported almost at every surface point for large frequencies. The edges of the mountains exhibited the larger impact for the dome-shaped mountain. An important generation of Rayleigh waves was reported for the horse-shoe shaped mountain. Indeed, IEM proved to be very effective at modeling linear unbounded domains. Such a methods are attractive mainly because they only require discretization on the boundary, which drives small meshes and very few number of equations. Additionally, they are highly efficient at modeling outgoing waves through infinity, which is crucial at conducting seismic ground motion simulations. IEM however, are usually computational expensive. This is explained by the fully populated and non-symmetric nature of their matrices. Moreover, from the extensive number of validation studies considering the effects of topography, only a small group of these studies are based upon IEM techniques and all of them limited to isolated

ridges (Kawase and Aki, 1990; Bouchon and Barker, 1996; Chávez-García et al., 1996; LeBrun et al., 1999). In addition they are capable in practice to deal only with simple crustal structures and cannot model efficiently realistic heterogeneous regions. Thus, to date, IEM have been restricted mostly to simple topographic shapes (e.g., Kamalian et al., 2003; Zhou and Chen, 2006; Mogi and Kawakami, 2007; Kamalian et al., 2007; Nguyen and Gatmiri, 2007; Kamalian et al., 2008; Sohrabi-Bidar et al., 2009, 2010; Sohrabi-Bidar and Kamalian, 2013).

Perhaps the most well-known method for numerical simulation in the engineering community is the finite element method (FEM). Although FEM allows a full description of arbitrary geometries, which is a significant feature in the numerical modeling of topographic scattering, its use in seismology has been limited. Former FEM studies appear in the late 1990s. Among those studies, Athanasopoulos et al. (1999) aimed at reproducing the effects of the 1999 Egion earthquake by analizing a 2D ground profile section across the town. Nonlinearity was considered through a linear-equivalent approach. His findings show a dramatic amplification (290%) at the elevated part of the town. An even more dramatic amplification (460%) was reported at the fringe of the slope. Another set of FEM studies are the ones conducted in Greece after the 7 September 1999 Athens earthquake, which showed clear evidence of topographic effects. For instance, Gazetas et al. (2002) studied the impact of the earthquake in the region of Adámes, and reported topographic aggravation factors (TAF) around 1.4 over a significant band of frequencies. Assimaki and Gazetas (2004); Assimaki et al. (2005a), and Assimaki et al. (2005b) conducted a set of parametric studies over the cliff of a riverbank where intensive damage was reported. Moreover, the effects of soil-nonlinearity and soil-structure interaction were also considered. Results from the simulations exhibit the overall findings of previously reported cases, i.e., stronger amplifications at/or in the vicinity of the crest, and a lager topographic influence for incident SV waves. However, it was pointed out that geometry by itself could not

account for the observed level of topographic degradation, and highlighted the importance of factors such as the underlying layers on the overall behavior.

Theoretical tools have also helped to shed some light on topography induced site effects. Unfortunately, analytical findings are scarce, and mostly limited to very simple geometries. Additionally, because diffraction and scattering are not linked to mode conversion in the antiplane case, the available theoretical findings are limited to the propagation of SH waves. Notwithstanding, theoretical approaches are still needed as: 1) benchmark for numerical simulation, and 2) to clarify the underlying physics of some topographic profiles. As an example, Hudson (1967) presents an approach for 3D small inclusions at the free surface of a half-space. His work is based upon perturbation techniques presented by Gilbert and Knopoff (1960). The idea is to replace the irregularity by an equivalent stress distribution. Although perturbation theory was believed to be constrained to inclusions of small slopes, further developments show good agreement between scattered Rayleigh waves and observations even for slope angles as large as 25° or 30° (Hudson and Boore, 1980). A pioneering theoretical study by Sánchez-Sesma (1985) presents analytical solutions for a homogeneous, symmetric wedge-shaped domain under obliquely incident SH waves. This study predicts relative amplifications at the apex with respect to the incident wave as high as $\frac{2}{\nu}$, where the ridge angle is $\nu\pi$ ($0 < \nu < 2$) For the particular case of $\nu = \frac{1}{2}$ a closed form solution in the frequency domain can be easily found following simple ray theory concepts.

$$U_y = 2\left(\cos\left(\frac{\omega x}{\beta}\right) + \cos\left(\frac{\omega z}{\beta}\right)\right), \tag{1.1}$$

where ω is the frequency of excitation. Graphically, eqn. (1.1) depicts focusing effects at both the interior and the free boundaries of the wedge as well as the expected constant maximum for all frequencies at the apex (4 times the amplitude of the incident wave at the

apex). More general situations such as incidence of P-, S-, or Rayleigh-waves is a challenge due to the strong diffraction effects from the boundaries.

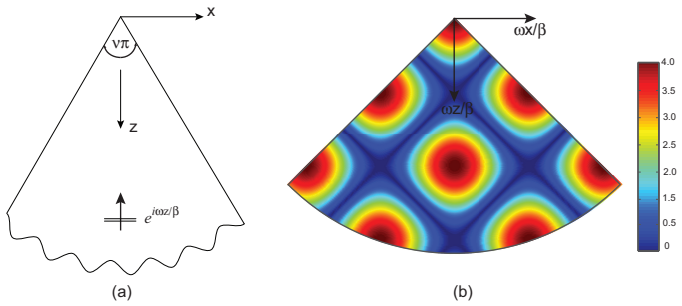

Figure 1.1: (a) Symmetrical infinite wedge under incidence of vertical *SH* waves. (b) Magnitude of the displacement in the frequency domain (ω) for a $45°$ symmetrical wedge with shear wave velocity β. The amplification at the tip of the wedge is four times the amplitude of the incident wave.

Recent analytical efforts have further highlighted the importance of theoretical work in the study of geometric focusing and scattering of SH plane waves by convex topography (e.g., Tsaur and Chang, 2009; Tsaur, 2011). Figure 1.2 presents results of maximum surface amplitudes for different h/a ratios in a circular-arc topography presented by Tsaur and Chang (2009). In this work, the authors use the wavefunction expansion method plus the region matching technique to derive a series solution. Four different incident angles ($\alpha = 0°, 30°, 60°, 90°$) were analyzed. Every simulation is based upon an incident SH Ricker's pulse with non-dimensional frequency $\eta = \frac{2a}{\lambda} = 4$, where λ is the wavelength of the incident wave. Notice that for $\alpha = 0°$, increasing the mountain ratio h/a enhances the amplification and de-amplification of motions on the convex surface. The largest amplification takes place near the mountain's foot rather than at its top. For oblique incidence, the surface amplitude shifts towards the right-hand flank, which is in agreement with results from other studies (e.g., Bouchon, 1973). A remarkable feature revealed by the analytical results is the highly oscillatory pattern displayed by the free-surface amplitude. Even for distances as far as x/a=$\pm$4 (x/λ=$\pm$8 for η=4) the solution shows pronounced oscillations around the free-field amplification value $|u| = 2$. This result is significant for defining the

domain size, and location of the absorbing boundaries in domain discretization numerical techniques.

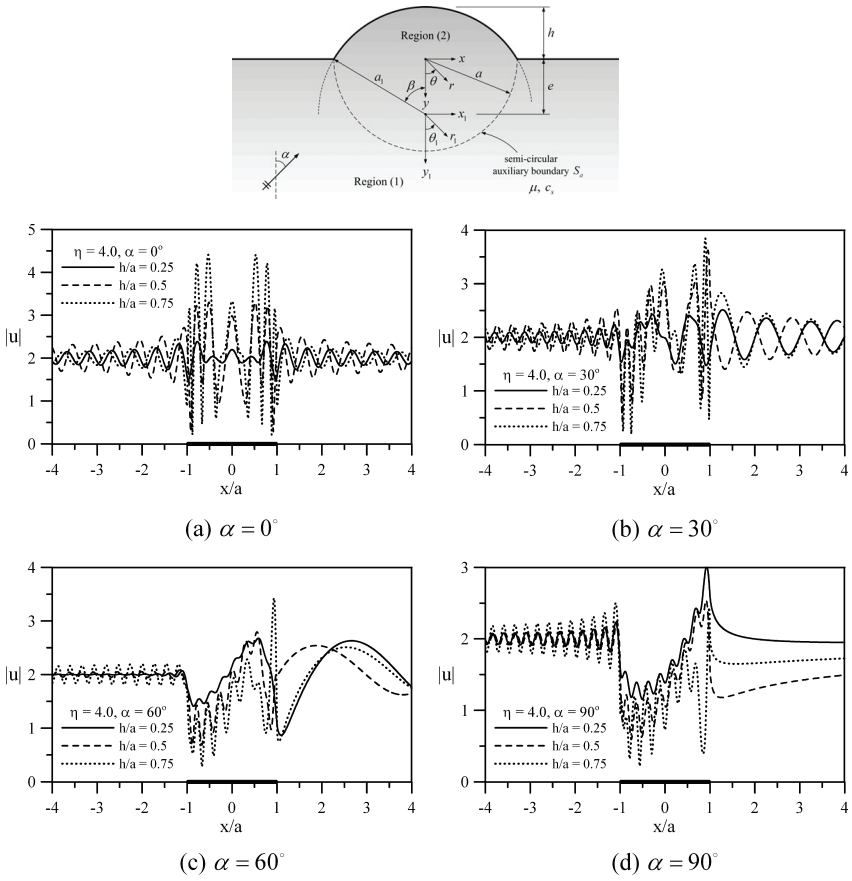

Figure 1.2: Surface amplitudes for different h/a ratios in a circular-arc topography (see top figure), and non-dimensional frequency $\eta = 4$, under four incident angle α scenarios of a SH plane wave (after Tsaur and Chang, 2009).

1.3 Large-Scale Numerical Simulations

Realistic regions of the crustal structure may include complex mountain ranges with highly heterogeneous subsurface structures and enclose or be located near to rupture zones of expected major earthquakes. Because a large number of highly populated metropolitan areas are located in these regions, large-scale 3D numerical simulations have been used increasingly to estimate the expected ground motions; especially when actual strong ground

motion data is scarce or non-existent. Large-scale simulations have been treated computationally mainly through three numerical schemes: finite differences (FDM), finite element (FEM), and more recently by means of spectral finite elements (SEM) methods. Starting with the Frankel and Vidale (1992) study, the FDM became the preferred numerical tool for large scale simulations (e.g., Frankel, 1993; Olsen and Archuleta, 1996; Pitarka et al., 1998; Sato et al., 1999). However, in cases of irregular topography, the well-known intrinsic inadequacies of the FDM for representing both complicated 3D geometries and accurate free surface conditions, impose a strong constraint only partially overcome at the expense of high computational cost (Komatitsch and Vilotte, 1998). In contrast, the FEM and the SEM can not only easily manage heterogeneous media with irregular internal stratigraphy, or even non-linear material behavior, but also automatically satisfy the free-traction boundary condition. Because of the latter, FEM and SEM schemes have been largely conducted during the last two decades with notable results (e.g., Seriani and Priolo, 1994; Bao et al., 1996; Faccioli et al., 1997; Bao et al., 1998; Komatitsch and Vilotte, 1998; Seriani, 1998; Bielak et al., 1999; Komatitsch et al., 2004; Bielak et al., 2005). Therefore, both approaches are excellent alternatives for performing large-scale simulations including realistic surface topography.

The FEM and SEM have proved to be accurate and extremely versatile numerical schemes for the study of wave propagation problems at a regional scale. Komatitsch et al. (2004) simulate ground motions for the 9 September 2001 M_{w} 4.2 Hollywood earthquake, and the 3 September 2002 M_{w} 4.2 Yorba Linda earthquake via SE schemes. The model employed uses a un-structured mesh covering a volume of 516 km $\times$ 507 km $\times$ 60 km of Southern California tailor-made to satisfy a maximum frequency, $f_{\max} = 0.5$ Hz. Macroscopic structures as the San Gabriel mountains are also included. The study does not determine in full extent the topographic impact; instead, their findings are focused on comparisons between filtered synthetics and recorded data. A good agreement between simulated records and

field data was exhibited at every network station including even those located at the San Gabriel mountains.

By means of FEM simulations, Ma et al. (2007) studies the effects of a simulated M_{w} 7.5 earthquake on the Mojave segment of the San Andreas fault. The region of study covers an area of Southern California of 209.6 km $\times$ 120 km $\times$ 46 km. Results are limited to the frequency band $f_{\max}$= 0.5Hz. Under the simulated conditions, ground motion reductions of up to 20% - 30% in most areas of the San Bernardino Valley, the Chino Basin, and the Los Angeles Basin can take place as a result of the "shielding" effect from the San Gabriel mountains. This alleged shielding effect can, however, be reverted if shallow earthquakes occur inside the basin. In this case, the surface topography surrounding the basin will reflect the energy into the basin, therefore increasing the ground motion amplitudes.

Different locations in the northern Taiwan region have been extensively studied via SE simulations (e.g., Lee et al., 2008, 2009a,b). In Lee et al. (2008), the low-velocity sedimentary Taipei basin as well as the surrounding surface topography were included in a SE domain of 101.9 km $\times$ 87.5 km $\times$ 102.89 km of $f_{\max}$= 1.0Hz. The study considers a small, local earthquake M_{L} 3.8 as a point source located near the south eastern edge of the basin. Simulation results show that topography can change PGA values in mountainous areas by $\pm 50\%$ when compared to the response of a half-space model. A second study on the Taipei basin simulates the interaction between large-scale topography and the sedimentary basin for various rupture scenarios (Lee et al., 2009a). The evidence for shallow earthquakes shows that the mountain range scatters the surface waves; as a result, the ground motions in the Taipei basin are decreased. In contrast, for deep-hypocenter earthquakes, peak ground velocity (PGV) could increase by as much as 50% due to the interaction of surface waves with the surface mountains. Finally, Lee et al. (2009b) focused on investigating the effects of high resolution surface topographic information over the synthetic wave-forms. The study is based upon a small-scale domain 4.2 km $\times$ 3.9 km $\times$ 4.6 km in northern Taiwan using

two surface resolution meshes, 2m (HR) and 40m (MR) respectively. A hypothetical earthquake represented by a double-couple point source was considered. Results from the HR model present a more complex distribution of PGA values with larger values near the top of mountain and ridges, and lower values in the valleys than those from the MR model. The results also highlight the strong dependence of topography with source frequency content, the complex patterns of reflected and scattered waves, and the significant increment in the duration of shaking produced by mountains.

Chapter 2

Conceptual Framework and Strategy

Large-scale, physics-based earthquake simulations of flat-free surface domains have been mainly conducted via the finite difference method (FDM), (e.g., Frankel, 1993; Olsen and Archuleta, 1996; Pitarka et al., 1998; Sato et al., 1999; Graves and Pitarka, 2010). The simplicity, easy computational implementation, and relative accuracy, surely account for the widespread use of FDM schemes in studying interior complex geological models without topography. The finite element method (FEM) has also gained an increasing interest among researchers. (e.g., Bao et al., 1998; Bielak et al., 1999, 2005; Moczo et al., 2007a; Taborda and Bielak, 2013). This is explained because of the intrinsic capabilities of FEM schemes to represent traction-free boundary conditions, and continuity between material interfaces, even though larger computational resources are usually needed. The FEM allows irregular elements of any size and shape, therefore, can naturally conform to any geometry. However, its computational efficiency in end-to-end earthquake simulation deeply rely on the use of uniform un-structured grids.

The use of unstructured meshes of uniform elements (e.g., Koketsu et al., 2004; Tu et al., 2006; Haber et al., 2012), present a very appealing feature in large scale end-to-end FEM earthquake simulation. Since every mesh element is a cube, one needs to compute only a

single template stiffness matrix at the beginning of the simulation. Then, at running time, this matrix is scaled for every element depending on its size and material properties. This results in a substantial reduction in memory requirements. Such a strategy, however, inevitably leads to non-conforming schemes. Consequently, internal material interfaces are usually assumed as staircase boundaries in which the accuracy of FEM schemes relies on small element sizes. From the extensive number of FDM, and FEM validation studies, it appears that such a simplification in modeling interior regions is minor. Evidence of the latter was recently provided by Pelties et al. (2010). His study reports the dependence of the numerical error of regular square-shaped 2D meshes by comparing their results with triangular meshes that honor the internal boundaries. By changing the mesh size, material contrast and frequency characteristics of the wavefields, the authors provided empirical rules to ensure the reliability of the staircase approximation. For material contrasts of up to 0.5 for instance, a discritization of five elements per shortest dominant wavelength exhibits acceptable responses in spite of complex material interfaces. Stronger impedance contrast on the other hand, can drive meshes up to 12 points per wavelength (PPW). Because FEM meshes are often tailored to accommodate 12 PPW, conclusions from Pelties et al. (2010) studies validate the use of stair-like meshes to represent internal material interfaces. External topographies (free-surface boundaries), or elastic-acoustic coupling, on the other hand, lead to an impractical mesh refinement, and should, if possible, be treated by conforming the targeted geometry.

Modeling a complex domain at a regional scale including a mesh that honors the topography, is still not an easy undertaking. Sharp interfaces, the vast computational resources needed, and the broad range of geological scenarios make the problem far from being a ”single-button” procedure (Casarotti et al., 2008). Because seismologists have traditionally favored the FDM over other approaches (Moczo et al., 2007b), recent alternatives have been developed to address the intrinsic inadequacies of FDM schemes at representing complicated 3D geometries, or accurate free surface conditions (e.g., Zhang and Chen, 2006;

Lan and Zhang, 2011; AlMuhaidib et al., 2011; Zhang et al., 2012). These new approaches reduce the prohibitively dense spatial samples present in past studies where up to 60 PPW have been reported (e.g., Hayashi et al., 2001; Bohlen and Saenger, 2006). Despite these advances, there is still a lack of consensus about the best strategy to be adopted. Moreover, 3D studies that involve strong discontinuities and strong heterogeneities need further investigation. These shortcomings make FDM still difficult to be used in practical scenarios with surface topography.

As previously mentioned, high-order finite element methods in the form of the spectral finite element method SFEM (e.g., Seriani and Priolo, 1994; Faccioli et al., 1997; Komatitsch and Vilotte, 1998; Komatitsch et al., 2005), have emerged as highly accurate tools for performing high-resolution simulations of seismic wave propagation at global, regional, and continental scales (e.g., Komatitsch and Tromp, 2002a,b; Lee et al., 2009a,b; Stupazzini et al., 2009; Cupillard et al., 2012). The SFEM is based on high-order Lagrange polynomials in conjunction with a Gauss-Lobatto-Legendre (GLL) integration scheme. This automatically renders diagonal elemental mass matrices, resulting in a notable accuracy, and high-order convergence rates. Regarding the mesh, the SFEM is restricted to hexahedral elements. Such a feature allows honoring any internal or external boundary of the domain precisely, although places a significant computational burden. According to Casarotti et al. (2008), creating an unstructured all-hexahedral mesh, for a realistic heterogeneous domain, can require months even under expert supervision.

On the other hand, ongoing FEM developments within the framework of fracture- and micro-mechanics, such as the XFEM or the GFEM methods, highlight the advantages of using non-conforming (possibly regular un-structured) meshes for simulating highly heterogeneous materials with an acceptable level of accuracy and reasonable computational cost (e.g., Belytschko and Black, 1999; Moës et al., 1999; Strouboulis et al., 2000; Fries

and Belytschko, 2010; Zohdi and Wriggers, 2008). In the XFEM/GFEM, enrichment functions are added to the classical FEM approximation to account for cracks or discontinuities (Mohammadi, 2008). This enrichment simplifies matters drastically since the mesh of complex domains does not need to match the geometry. The occurrence of different materials within any given finite element is managed by: (i) numerical homogenization techniques (e.g., Moës et al., 2003; Toulemonde et al., 2008), (ii) decomposition of elements (e.g., Daux et al., 2000; Strouboulis et al., 2000; Sukumar et al., 2001), or, (iii) it is managed at the integration point level (e.g., Zohdi and Wriggers, 2001, 2008). In particular, the latter authors present rules to quantify the degree of the Gauss quadrature scheme to be used in finite elements that exhibit an integrand discontinuity. These rules along with unaligned meshes schemes have recently been used in related areas such as soil-structure interaction (Park et al., 2013). It is evident then, that because the contrast vacuum/soil is nothing but an extreme case of material interface, conclusions from studies of multi-phase materials should also be valid in a surface topography context.

The following section focuses at presenting a numerical alternative for seismic wave propagation simulation in heterogeneous media including realistic surface topography via FEM. Two strategies for managing the finite elements in the neighborhood of the targeted topography are presented. In particular this work can be seen as an extension of ideas originated in the fracture- and micro-mechanics framework applied to the realm of end-to-end earthquake ground motion simulation. The first strategy will be based upon a treatment at the integration point level, while the second one could be categorized as a semi-decomposition technique. Theoretically, both strategies are general, and can be used irrespective of the dimensionality of the problem. Here, however, we favor the first strategy for analysing 2D wave propagation problems, while reserve the second scheme for 3D large-scale simulations. The 3D strategy will be based upon non-conforming octree-based meshes from Hercules (Tu et al., 2006); the octree-based finite element parallel software developed by the Quake group at Carnegie Mellon University. Hercules was originally intended to handle

flat free-surfaces based upon an explicit central difference time forward scheme, and trilinear spatial discretization that renders a quadratic convergence rate for displacements in both space and time. Kinematic faulting is considered as a set of point sources whose displacements (slips) are prescribed. Classical Lysmer-type local absorbing boundary conditions (Lysmer and Kuhlemeyer, 1969) are considered at the exterior boundaries of the computational domain. Free surface conditions are satisfied naturally because of the variational formulation. Domain discretization is performed by means of an octree mesh generator.

2.1 Non-Conforming Meshing Scheme for Solid-to-Vacuum Interfaces

The ground displacements in the i-th direction u_i within a computational domain Ω with external boundary Γ (see Fig. 2.1) are governed by the Navier's equation of elastodynamics;

$$(\lambda + \mu)u_{k,ki} + \mu u_{i,kk} + b_i = \rho \ddot{u}_i \ . \tag{2.1}$$

In eqn. (2.1) λ, μ, and ρ denote the Lamè constant, shear modulus, and density respectively, while b_i represents the body force in direction i. In order to obtain a discrete representation of eqn. (2.1), it is assumed that an arbitrary domain Ω can be represented in terms of a set of non-overlapping cubic elements Ω_e of the type shown in Fig. 2.1, such that:

$$\Omega = \cup\, \Omega_e^* \quad \Gamma = \cup\, \Gamma_e^* \ , \tag{2.2}$$

where $\Omega_e^* = \Omega_e$ for interior elements and is equal to the real portion of Ω enclosed by Ω_e for exterior elements. Likewise, Γ_e^* corresponds to the portion of Γ enclosed by Ω_e for exterior elements.

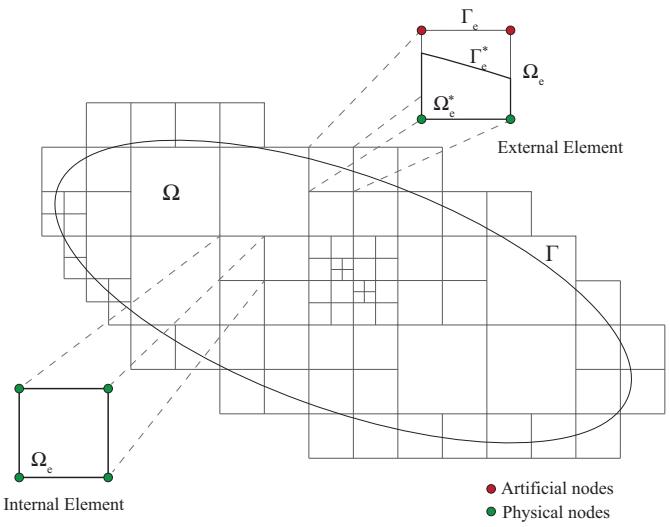

Figure 2.1: Nonconforming unstructured octant-mesh (2D version).

Adopting the same strategy followed by Daux et al. (2000) for the treatment of voids and holes by means of the XFEM, we assume a displacement approximation for the trial function in Ω of the form:

$$\mathbf{u}^h(\mathbf{x},t) = \sum_{i \in I} \phi_i(\mathbf{x}) g(\mathbf{x}) \mathbf{u}_i \ , \tag{2.3}$$

in which I is the set of all the nodes in the mesh, $\phi_i(\mathbf{x})$ is the standard finite element global base function associated with the i-th node, $\mathbf{u}_i$ is the vectorial degree of freedom at node i, and $g(\mathbf{x})$ is the so-called enrichment function (Daux et al., 2000) defined as:

$$g(\mathbf{x},t) = \begin{cases} 1 & \text{if } \mathbf{x} \in \Omega \\ 0 & \text{if } \mathbf{x} \notin \Omega \ . \end{cases} \tag{2.4}$$

Adopting eqn. (2.3) as the trial function in a spatial Galerkin discretization by finite elements of eqn. (2.1) produces a system of ordinary differential equations of the form:

$$\mathbf{M}\ddot{\mathbf{u}} + \mathbf{K}\mathbf{u} = \mathbf{P} \ , \tag{2.5}$$

where $\mathbf{M}$ is the mass matrix, $\mathbf{K}$ is the stiffness matrix, $\mathbf{P}$ is the vector field of effective forces, and $\mathbf{u}$ is the vector of nodal displacements. $\mathbf{M}$ and $\mathbf{K}$ are sparse matrices. Redefining the global shape functions as:

$$\psi_i(\mathbf{x}) = g(\mathbf{x})\phi_i(\mathbf{x}) \,, \tag{2.6}$$

the (*i*,*j*)th 3×3 block matrices in $\mathbf{M}$ and $\mathbf{K}$ are:

$$\mathbf{m}_{ij} = \int_\Omega \rho\psi_i\psi_j\mathbf{I}\,\mathrm{d}\Omega \,, \tag{2.7}$$

$$\mathbf{k}_{ij} = \int_\Omega (\mu+\lambda)\nabla\psi_i\nabla\psi_j^\intercal\,\mathrm{d}\Omega + \int_\Omega \mu\nabla\psi_i^\intercal\nabla\psi_j\mathbf{I}\,\mathrm{d}\Omega \,. \tag{2.8}$$

Equations (2.7) and (2.8) preserve the conventional form encountered in linear elastodynamics under a FEM framework (e.g., Bao et al., 1998). More important, because of the use of the enrichment function $g(\mathbf{x})$, equations 2.7 and 2.8 properly handle the actual boundary of the domain and the traction-free condition in Γ. For nodes within Ω both expressions reduce to those from the classical FEM scheme because the enrichment function is simply $g(\mathbf{x}) = 1$. For external nodes, equations (2.7) and (2.8) are still valid as long as the integrals are evaluated over the actual portions of Ω enclosed by the cubic finite element. As was pointed out by Fries and Belytschko (2010), the treatment of voids and holes by XFEM ideas renders the same result as in the classical FEM framework as long as the zones of empty material in the element are excluded from the integral of the weak form. It is important to mention however, that since the displacement field is expressed in terms of physical- and non-physical nodes (green, and red nodes in Fig. 2.1), the numerical scheme cannot strictly be tagged as an ordinary FEM analysis.

2.2 Numerical Integration. Quadrature Rule Approach

Inherent to non-conforming meshing schemes is the evaluation of discontinuous integrands. The evaluation of eqn. (2.8), and eqn. (2.7) has traditionally been computed numerically using standard quadrature rules. For interior elements the numerical integration is straightforward. Moreover, because internal elements exhibit cubic shapes (squares in 2D), scalability holds. Therefore, the stiffness and mass matrices need to be computed only once. For external elements on the other hand, the scalability is precluded due to variations of $g(\mathbf{x})$ in regions close to Γ. The main idea is then to use a sufficient number of Gauss points to achieve proper accuracy. An example of this is the work of Benowitz and Waisman (2013). Under the framework of XFEM the authors presented results of arbitrarily shaped inclusions in 2D linear elasticity using a Gaussian quadrature of order 20. No comments were made on how that large quadrature order was obtained.

Better insights regarding the accuracy of quadrature rules in dealing with discontinuous functions were presented by Zohdi and Wriggers (2001, 2008). Here, the error bound in the integration of a discontinuous function is expressed by the largest quadrature weight w_i and the maximum distance $\zeta_i - \zeta_{i+1}$ between two neighbouring Gauss points. For the 1D case, the least-square curve fit reported gives:

$$\text{error bound} \approx 5.07 G^{-1.82}, \tag{2.9}$$

where G is the number of quadrature points. The extension to the 3D case is straightforward. The corresponding errors are shown in Table 2.1.

The last result proves that by using an adequate number of Gauss points integrals eqn. (2.8), and eqn. (2.7) can be computed accurately even for the 3D situation. The applicability and the reliability of the proposed numerical scheme was recently proven right in the

Integration error bound behaviour for a 3D step function unit discontinuity.

Gauss rule	error bound(%) = $\frac{\left(5.07G^{-1.82}\right)^3}{8} \times 100\%$
$2 \times 2 \times 2$	37
$3 \times 3 \times 3$	4
$4 \times 4 \times 4$	0.8
$5 \times 5 \times 5$	0.2
$10 \times 10 \times 10$	0.006

Table 2.1: Integration error bounds. After 1D expression from Zohdi and Wriggers (2001)

framework of 3D soil-structure numerical modeling by Park et al. (2013). Soil-structure interaction is another challenge of crucial importance in earthquake, and civil engineering. Through numerical examples the authors concluded that finite elements with discontinuities accurately consider the characteristics of the soil profile, and can be used to predict the dynamic response of building structures when subjected to earthquake ground excitation in soft soils.

2.2.1 Lumped Mass Matrices

For the time-integration algorithm, Hercules uses a central difference explicit time-marching scheme that avoids the need for solving the coupled system of equations after lumping $\mathbf{M}$. Given that eqn. (2.7) renders full mass matrices, the decoupling of the exterior degrees of freedom cannot be performed without further simplification. In this study, this is accomplished by replacing eqn. (2.7) by an equivalent lumped-mass elemental matrix of the form:

$$m_{ij}^{k} = m_o \left(\frac{\int_{\Omega_e^*} \left(N_k\right)^2 \mathrm{d}\Omega_e^*}{\int_{\Omega_e^*} N_s N_s \, \mathrm{d}\Omega_e^*} \right) \delta_{ij}, \quad m_o = \int_{\Omega_e^*} \rho \, \mathrm{d}\Omega_e^* \,, \tag{2.10}$$

where k denotes the node of the octant, N_j is the local shape function associated with node j which satisfies the conventional zero-one property, m_o is the total mass of the element,

and Ω_e^* is the volume occupied by the element. The equivalent mass matrix is formed by: (i) preserving the actual mass held by the external element; and (ii) keeping the ratio of the trace elements in the consistent element mass matrix. The nodal mass associated with the i-th node of interest is obtained in the conventional way by adding up the contributions from all the elements adjacent to the node.

2.3 Numerical Integration. Virtual Topography Scheme

The error bounds presented in Section 2.2 provide a convenient way for dealing with integrals that involve discontinuous functions. Two major drawbacks appear, however, in 3D large-scale realistic situations. First, because each exterior finite element encloses a different portion of the topography within, each stiffness and mass matrix must be computed and stored independently. Consequently, the overall computational efficiency and simulation time is affected. Second, in cases where any exterior finite element covers only a small portion of the topography, strong artifacts appear due to the small lumped mass values linked to the element nodes. Therefore, the required time step in the numerical integration scheme is greatly affected.

To avoid this difficulty, this dissertation follows a simple strategy. The idea is to further divide all the exterior topographic elements (TpElm) into tetrahedra elements. Splitting ideas, or the use of the special features exhibited by triangles and/or tetrahedra in non-conforming meshing schemes have been used by many authors in a variety of scenarios (e.g., Kim and Swan, 2003; Rozycki et al., 2008; Dréau et al., 2010; Dunant et al., 2013). Of particular importance due to the similarities in splitting octree-based meshes, is the study of Kim and Swan (2003). These authors combine a unit cell homogenization technique together with octree-based meshes in a FEM framework to predict the mechanical behavior of woven composite textiles.

Our division, however, is not intended to follow the decomposition scheme of XFEM where elements are partitioned into sub-domains that align with the domain boundaries in order to carry out the integrals over them. Our local partition specifically divide the cubic element into five, still non-conforming tetrahedra elements in order to better approximate the geometry and mechanical contribution of the topographic feature Fig. 2.2.

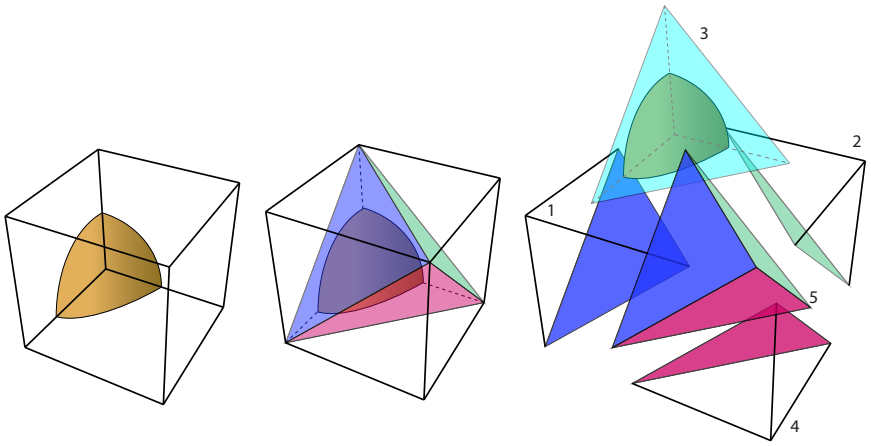

Figure 2.2: Cubic topographic element partitioned into five non-conforming linear tetrahedral elements.

As can be seen from Fig. 2.2, the proposed partition ensures that no additional nodes are created within each parent cube. Additionally, it is also clear that empty tetrahedra are eliminated from any further computations. This further assures numerical stability. The division at the topographic element level admits writing down the stiffness matrix of the exterior element as the contribution from its five tetrahedral elements:

$$\mathbf{k}_{ij}^{\mathrm{TpElm}} = \sum_{s=1}^{\#\ \mathrm{Tetrahedra}} \int_{\Omega_s} (\mu+\lambda)\nabla\psi_i\nabla\psi_j^{\intercal}\,\mathrm{d}\Omega_s + \int_{\Omega_s} \mu\nabla\psi_i^{\intercal}\nabla\psi_j\mathbf{I}\,\mathrm{d}\Omega_s. \tag{2.11}$$

It is understood that the summation symbol in eqn. (2.11) stands for the proper assembly of each tetrahedron contribution to the nodal stiffness.

The most salient feature of such a partition is, however, related with the calculation of the stiffness matrices in eqn. (2.8). Since each tetrahedron is linear, gradients in eqn. (2.11)

turn into constants which are taken out of the integrals. As a result, the evaluation of the stiffness integrals reduces merely to computing the volume occupied by each tetrahedron.

$$\mathbf{k}_{ij}^{\mathrm{TpElm}} = \sum_{s=1}^{\#\ \mathrm{Tetrahedra}} \left((\mu+\lambda)\nabla\psi_i\nabla\psi_j^{\intercal} + \mu\nabla\psi_i^{\intercal}\nabla\psi_j\mathbf{I}\right)_s \int_{\Omega_s} \mathrm{d}\Omega_s \ . \tag{2.12}$$

Multiplying, and dividing eqn. (2.12) by the full volume of each tetrahedron V_{full}^s gives:

$$\mathbf{k}_{ij}^{\mathrm{TpElm}} = \sum_{s=1}^{\#\ \mathrm{Tetrahedra}} \left[\left((\mu+\lambda)\nabla\psi_i\nabla\psi_j^{\intercal} + \mu\nabla\psi_i^{\intercal}\nabla\psi_j\mathbf{I}\right)_s V_{\mathrm{full}}^s\right] \ \frac{\int_{\Omega_s}\mathrm{d}\Omega_s}{V_{\mathrm{full}}^s} \ . \tag{2.13}$$

The first factor between brackets in eqn. (2.13) is nothing but the complete stiffness matrix of the tetrahedron s, while the second term represents its void ratio $\varphi_s = \frac{\int_{\Omega_s}\mathrm{d}\Omega_s}{V_{\mathrm{full}}^s}$.

$$\mathbf{k}^{\mathrm{TpElm}} = \sum_{s=1}^{\#\ \mathrm{Tetrahedra}} \mathbf{k}_s^{\mathrm{FullTetrh}}\varphi_s. \tag{2.14}$$

From eqn. (2.14) it is clear that tetrahedral elements without any topography within will be automatically ruled out by φ as is expected intuitively, while the degree of participation of the remaining tetrahedra will be completely controlled by their void-ratios. Gauss quadrature rules are then needed only to compute these void-ratios. There is still another very important feature of eqn. (2.14). Since the void ratio modulates the contribution of each one of the five tetrahedra, eqn. (2.14) clearly shows that even for the case of irregular topography, scalability still holds.

2.3.1 Lumped Mass Strategy

Explicit step-by-step time integration methods have largely proven to be a reliable scheme for modeling structures in transient dynamic applications. It is also well known that the efficiency of explicit time integration schemes such as the central difference method heavily depend upon lumped mass techniques. By lumping the mass, the discrete representation of the balance equation does not involve the solution of any system of equations, thus, the computational cost is dramatically reduced. A regular concern in explicit dynamics however, is its stability. Since the central difference method is only conditionally stable, one must choose a time step Δt that satisfies the Courant–Friedrichs–Lewy condition. Under the absence of damping this condition yields:

$$\Delta t < \Delta t_{crit} = \frac{2}{\omega_{max}}\,, \tag{2.15}$$

where ω_{max} is the maximum natural frequency of the system. In practice ω_{max} is related with the highest eigenvalue of each mesh element taken independently. For conventional octree-based meshes Δt is traditionally taken as:

$$\Delta t = \frac{1}{c} * \min\left(\frac{h}{V_p}\right), \tag{2.16}$$

where h, and V_p stand for the element's size, and P-wave velocity respectively; c represents the Courant number, usually between 1, and 2. The minimum value in the whole mesh controls the time-step.

In our non-conforming meshing scheme, the time-step will be dominated by the tetrahedron element with the smallest material volume enclosed. The main concern is that these eigenvalues could reach very high values since the nodal lumped mass depend on the location of the enclosed volume. A way to overcome this difficulty is by assuming a uniform

lumped mass matrix for the tetrahedral elements. In other words, the material mass occupied by the tetrahedra is evenly distributed among its nodes as in traditional lumped mass schemes. This approach can be seen as a special case of the lumped mass matrix proposed by Menouillard et al. (2006) for a constant enrichment function $\phi = 1$. Later on Rozycki et al. (2008) also employed this special lumped matrix in related problems of explicit dynamics. For linear triangles/tetrahedra, the time-step stays as in eqn. (2.16) because the void factors of the stiffness and mass matrices cancel each other when computing the eigenvalues of the non-conforming tetrahedron (Rozycki et al., 2008).

To summarize, in our approach, which from now on will be called Virtual Topography, in addition to the generic stiffness matrix used for the cubic element, five additional generic stiffness matrices corresponding to the tetrahedral distribution shown in Fig. 2.2, are also computed and stored at the beginning of the simulation. For each topographic finite element, the five void-ratio factors are the only additional pieces of information needed; thus the increase of computational memory is insignificant. These void ratios are used to scale both the stiffness and the mass matrices of its corresponding tetrahedron. More important, because we also assume that scalability holds for the mass matrix, the traditional time-step from eqn. (2.16) is preserved. These characteristics are of paramount importance in dealing with large-scale earthquake simulations where the system of equations is usually composed of millions, sometimes even billions of equations that need to be solved thousands of times because of the time evolution of the wavefields. Since the Virtual Topography scheme is not constrained to follow the external topographic surface, it efficiently addresses the challenge of balancing the trade-off between accuracy and computational efficiency that is essential in earthquake simulation at regional scales. This is particularly significant as we incorporate topographic features into Hercules, our Quake group octree-based finite element code.

Chapter 3

2D Verification. Partial integration Scheme.

The methodology just described is used in two simple numerical experiments with idealized surficial irregularities in a 2D homogeneous half-space. Because 2D implementations are much easier than their 3D counterparts, the stiffness, and mass matrices will be computed following the Gauss quadrature scheme described in the first part of Chapter 2. Incident Rayleigh waves are chosen to represent the incoming wavefield because surficial irregularities have a larger effect in the propagation of surface waves than that of body waves due to the difference in their travel paths (Ma et al., 2007). Additionally, since Rayleigh waves present a more challenging scenario physically and numerically than incident body waves, this offers a more severe situation for testing the performance of the proposed numerical framework.

For the FEM approach, classical Lysmer-Kuhlemeyer (Lysmer and Kuhlemeyer, 1969) absorbing boundaries were implemented in all of the boundaries, except for the free surface of the domain; intrinsic material attenuation is omitted for simplicity; and a mass-threshold of 25 percent is imposed in the external elements to avoid numerical artifacts. That is, if the mass of the real portion of the domain held by an external element is smaller than 25 percent of the mass value of the full element, this element will no longer be considered as part of the simulation domain. Results from the proposed methodology are compared

with those obtained using DAMIAN (DAMIAN, 2010), a general 2D Boundary Element Method (BEM) tool developed by the Applied Mechanics Research Group at Universidad EAFIT (Medellín, Colombia) for modeling seismic-wave propagation and earthquake ground motion in homogeneous 2D regions. Using the solution of BEM as reference offers a high level of accuracy due to the Green's function-based nature of the BEM.

In both simulations, an incident Rayleigh wave traveling from the left side of the domain as a Ricker wavelet in time with characteristic frequency, $f_{\mathrm{c}} = 1$ Hz is considered as the seismic excitation. The incident wavelet is normalized in such a way that its horizontal component coincides with the shape of the Ricker pulse. The FEM and BEM meshes were discretized according to:

$$e_{min} = \frac{V_{s_{\min}}}{f_{\max}\mathrm{PPW}} \,, \tag{3.1}$$

in which e_{min} is the smallest element size. Equation (3.1) is expressed in terms of the minimum S-wave velocity $V_{s_{\min}}$ of the domain, the maximum frequency of the simulation $f_{\max}$, and the number of points per wavelength PPW. In these examples, a value of $\mathrm{PPW} = 10$ was used to assure a correct representation of the expected wavelengths. The Courant-Friedrichs-Lewy CFL condition of stability is guaranteed for the FEM simulation by using a time step:

$$\triangle t = \frac{e_{min}}{3V_{p_{\max}}} \,, \tag{3.2}$$

where $V_{p_{\max}}$ is the maximum P-wave velocity of the domain. This requirement is not needed for the BEM formulation although it was kept for consistency.

3.1 Semi-Circular Hill over Homogeneous Half-Space

Figure 3.1 illustrates a semi-circular hill of radius equal to the dominant wavelength λ_o:

$$\lambda_o = \frac{V_s}{f_{\max}} \,, \tag{3.3}$$

of the incoming wave, and the dimensions of the computational domain used for the analysis. The hill and half-space share the same S-wave velocity (V_s), P-wave velocity (V_p), and density (ρ).

Figure 3.2 shows a detailed view of the FEM mesh for the sub region of interest. The blue solid line represents the targeted shape of the semi-circular hill. The small red dots illustrate the 4×4 Gauss quadrature rule implemented for the numerical integration of equations (2.8), and (2.10) at the external elements. The error bound associated with the numerical integration scheme is $\approx 4\%$. This error could be easily reduced just by increasing the number of Gauss points although it will be shown that a remarkable accuracy is obtained with the adopted 4×4 rule. Receivers are denoted by the large green dots $\mathrm{S1}, \mathrm{S2}, ..., \mathrm{S5}$.

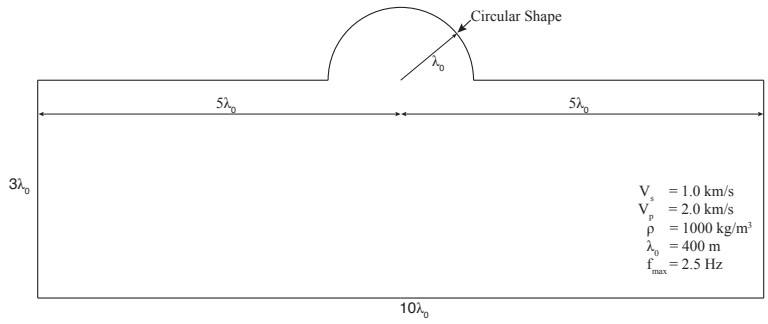

Figure 3.1: Computational domain of the semi-circular hill over homogeneous half-space

Results for the horizontal $\mathrm{U_x}$ and vertical $\mathrm{U_z}$ components of ground motion at the selected stations are shown in Fig. 3.3. Blue lines illustrate the results from the proposed FEM approach while red lines show the results from the BEM numerical scheme. Good agreement in the results can be observed for most of the stations. The proposed strategy, for instance,

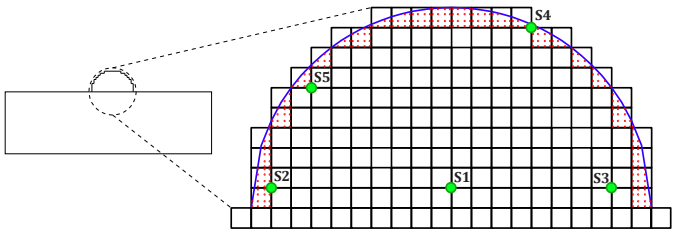

Figure 3.2: Detailed view of the FEM mesh at the region of interest. Red dots illustrate Gauss points used for the numerical integration at external elements. Green dots represent the selected internal receivers

reproduces almost wiggle-by-wiggle the response from the BEM formulation during the strong phase of the synthetics at all the stations near the base. For station $\mathrm{S4}$, a wiggle-by-wiggle agreement is still visible for the horizontal component of displacement. As to the vertical component, good agreement is achieved from a qualitative point of view, although the proposed strategy slightly over-predicts the maximum response at the specified location.

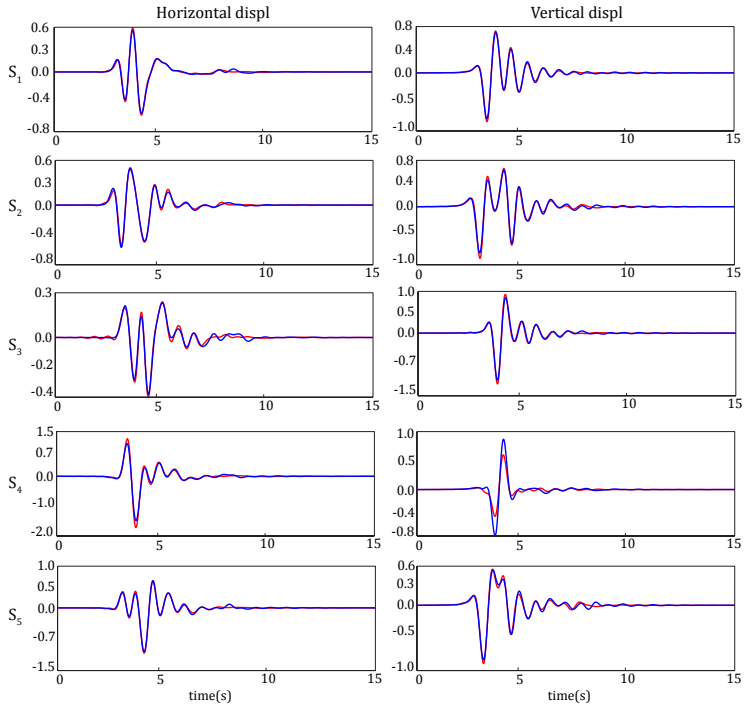

Figure 3.3: Displacements histories at stations $\mathrm{S1}, \mathrm{S2}, \mathrm{S3}, \mathrm{S4}, \mathrm{S5}$ throughout the semi-circular homogeneous hill. Blue lines illustrate the results from the proposed FEM approach while red lines show the results from the BEM numerical scheme.

Figure 3.4 presents the peak ground displacement (PGD) for the two components along the free surface. PGDs are normalized with respect to the corresponding component of the incident wave. The circular hill naturally divides the free surface into three regions. Results on the left side $(x/\lambda_o \leq -1)$, show variations only within one wave-length distance from the left foothill. In this zone, a mild amplification in both components is present at $\frac{x}{\lambda_o} \approx -1.5$. The larger reductions occur at the very left foot with an almost constant value of 0.7 for both components. On the surface of the hill $(-1 \leq x/\lambda_o \leq 1)$, large reductions/amplifications and strong spatial variability are observed. At the summit of the hill, the vertical PGD value is dramatically reduced to 30 percent of the vertical component of the incident field, while the horizontal PGD only experiences a modest amplification of 16 percent with respect to the incident component. The largest amplification of the horizontal component (1.5) occurs at about $x/\lambda_o \approx 1.5$ to the right of the hilltop. This shifting of the PGD from the hilltop is in agreement with results from other studies (Bouchon, 1973). Finally, on the right hand side of the foothill $(x/\lambda_o \geq 1)$, a noticeable shield effect such as that reported by Ma et al. (2007) is observed. Here, both PGD values are reduced, with larger changes once again close to the foot of the mountain and more evident for the horizontal component.

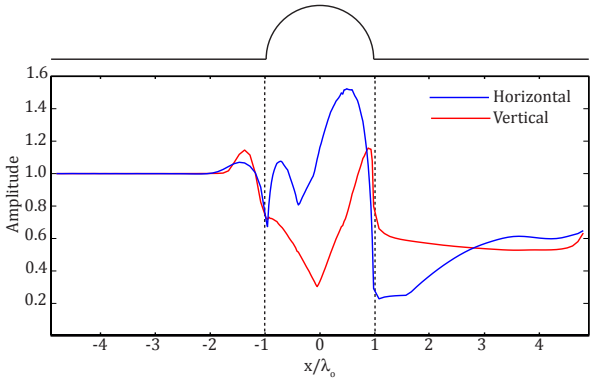

Figure 3.4: Distribution of peak ground displacement (PGD) over the free surface of the semi-circular hill over homogeneous half-space. Blue and red lines depict the relative amplification of the horizontal and vertical component of displacement with respect to the components of the incident Rayleigh wave.

New insights into the characteristics of the topographic system can be achieved by filtering-out the effects of the excitation using results in the frequency domain. Figure 3.5 presents

plots of frequency response as transfers functions (TF) relative to the amplitude of the incoming wave for the two components of displacement. These TF are presented as 2D contours of amplitude in terms of both frequency and location of selected receivers throughout the free surface. The 2D representations clearly depict spatial patterns of amplification. Such amplification greatly depends upon the position of the receiver. Over the reflected region ($x/\lambda_o \leq -1$) both components of displacement exhibit a stripe-like spatial pattern. For each frequency, the TF present several peaks and troughs. Some of the peaks in the vertical component are clearly associated with resonance frequencies. The spatial variation appears also to be more complex for the vertical component, although with smaller amplification values when compared with the horizontal results. Within the interior region $-1 \leq x/\lambda_o \leq 1$, two resonance frequencies are clearly distinguishable in the horizontal component contour, f $\approx$ 0.35Hz, and f $\approx$ 1.5Hz. Notice that f $\approx$ 1.5Hz is the frequency associated with the amplification of the horizontal component at $(x/\lambda_o \approx 0.5)$. In the transmitted region ($x/\lambda_o \geq 1$), some moderate diagonal stripes are present. The low and almost constant amplitude is evidence of (i) the shield effect of the hill, and (ii) a Rayleigh-like transmitted phase. In either case, the transmitted phases are substantially reduced by the topography, even at the receivers located near to the foothill.

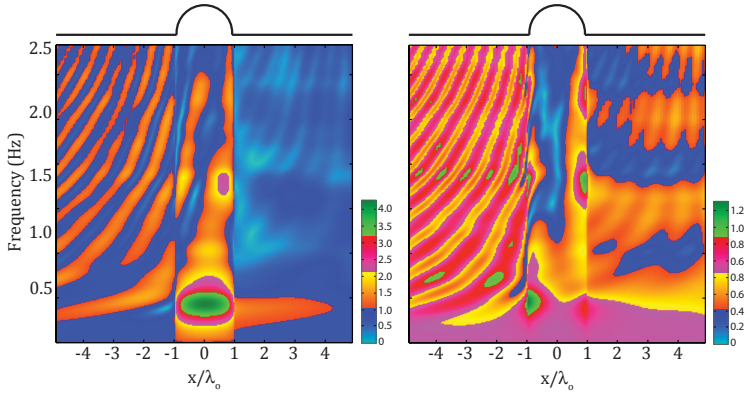

Figure 3.5: Transfer function amplitudes (TF) as function of position and frequency for both components of displacement. Left figure illustrates the TF amplitudes for the horizontal component of displacement. Right figure represents the TF amplitudes for the vertical component of displacement.

3.2 Semi-Circular Hill plus Parabolic Mountain over Homogeneous Half-Space

The second example consists of an idealized parabolic mountain merged with a semi-circular hill on a homogeneous half-space Fig. 3.6. An additional source of complexity is introduced in this simulation by including an impedance contrast between the half-space and the superficial scatterer. Figure 3.7 depicts a magnified view of the FEM mesh for the sub-region of interest. The solid blue line and the red dots represent the targeted surface and the Gauss' points used for the numerical integration at the finite elements on the mountain's boundary.

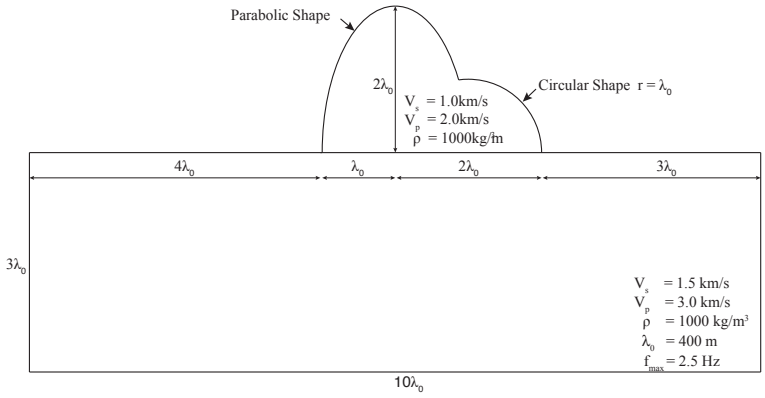

Figure 3.6: Computational domain for the parabolic ridge and semi-circular hill simulation.

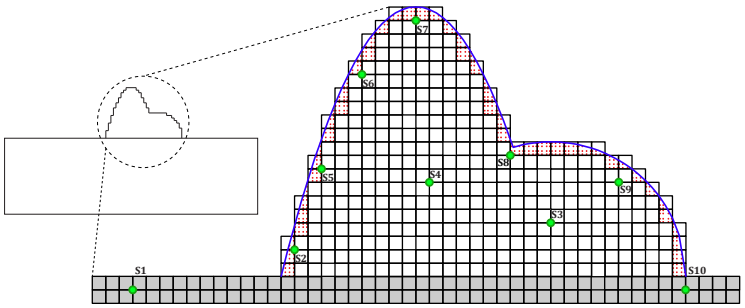

Figure 3.7: Enlarged view of the FEM mesh at the region of interest. Similarly as in Fig. 3.2 Red dots illustrate Gauss points used for the numerical integration at external elements. Green dots represent the selected internal receivers.

Figures 3.8 and 3.9 show a comparison between the synthetic displacements obtained with the FEM and the BEM schemes for the two components of motion at the selected receivers.

Here, excellent agreement was attained for all the stations reported. The proposed strategy is capable of reproducing the complex behaviour during the entire duration of the ground shaking, including all the main troughs and peaks during the strong phase of the ground shaking and the secondary peaks at the intermediate and final stages of the simulation. A better match among synthetics can be achieved if smaller elements are used for representing the targeted external surface.

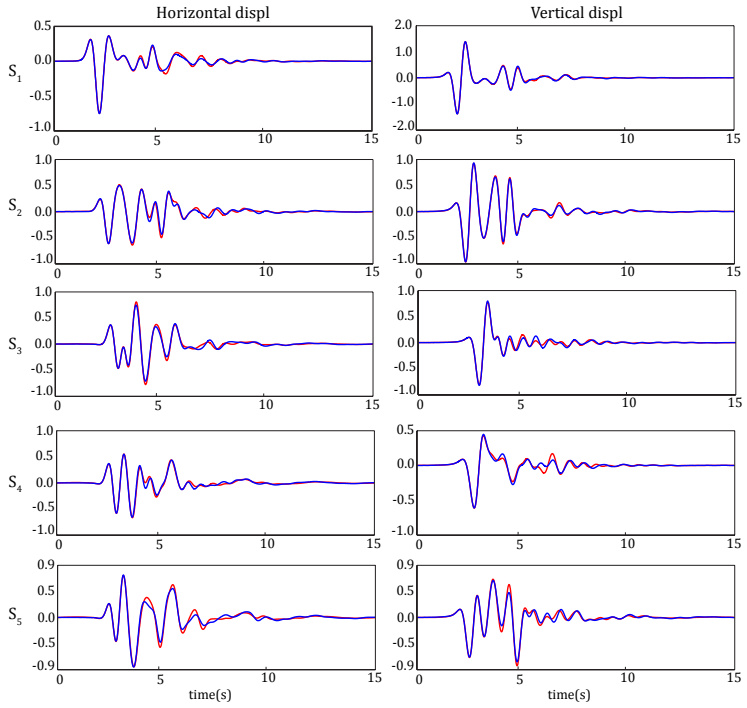

Figure 3.8: Comparison of surface displacement time histories at selected stations shown in Fig. 3.7. Blue lines represent the results from the proposed approach FEM. Red lines depict the results from BEM.

Figures 3.10 and 3.11 show the spatial variations of PGD and TF for the two components of motion across the region. In contrast to the previous example, the PGD exhibits a more stable pattern at both sides of the mountain. For $x/\lambda_o \leq -1$, no significant amplifications or reductions take place. For $x/\lambda_o \geq 2$, both components of displacement exhibit reductions with respect to the values from the incident field (Vertical=0.65 and Horizontal=0.40). These reductions are almost distance independent. The frequency characteristics

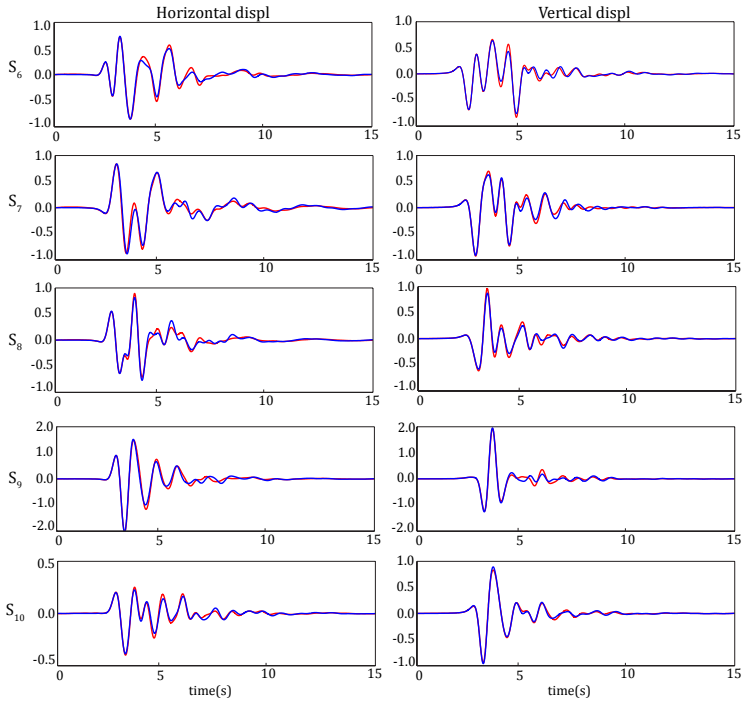

Figure 3.9: Comparison of surface displacement time histories at the additional selected stations shown in Fig. 3.7. Blue lines represent the results from the proposed approach. Red lines depict the results from BEM.

and spatial PGD changes exhibit a strong variation at the free surface of the mountain. Surprisingly, the largest amplification still occurs on the circular ridge, shifted to the right from its top. The values of the amplification however, differ substantially from the ones in the first example, reaching values as high as 2.2 and 1.6 for the horizontal and vertical components respectively. TF results present again a striped pattern across the reflected range, noticeable resonance frequencies at the mountain zone, and a clear shield effect in the transmitted region. In particular, the fundamental frequency for both components of displacement coincide (f $\approx$ 0.3Hz), although with major differences in the amplitude values (Fig. 3.10). Another interesting feature is the broader set of frequencies activated for the vertical motion at the mountain surface where a large cluster of harmonics spans almost the entire parabolic region of the domain.

The good fit exhibited by the synthetics suggests two important consequences for 2D scenarios. First, the idea of using virtual degrees of freedom is stable enough for representing

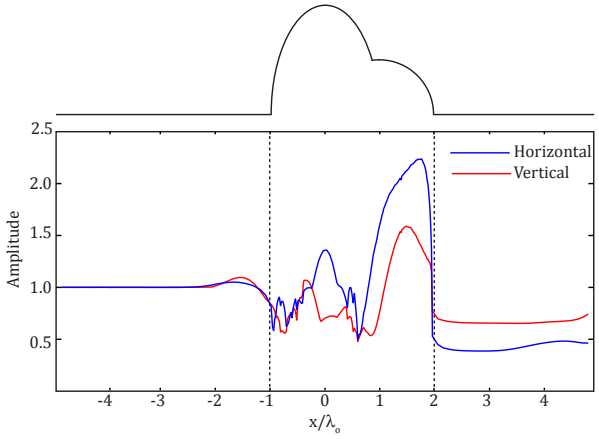

Figure 3.10: Distribution of peak ground displacement (PGD) for the parabolic mountain plus semi-circular hill over homogeneous half-space. Blue and red lines depict the relative amplification of the horizontal and vertical component of displacement with respect to the maximum values of the components of the incident Rayleigh wave.

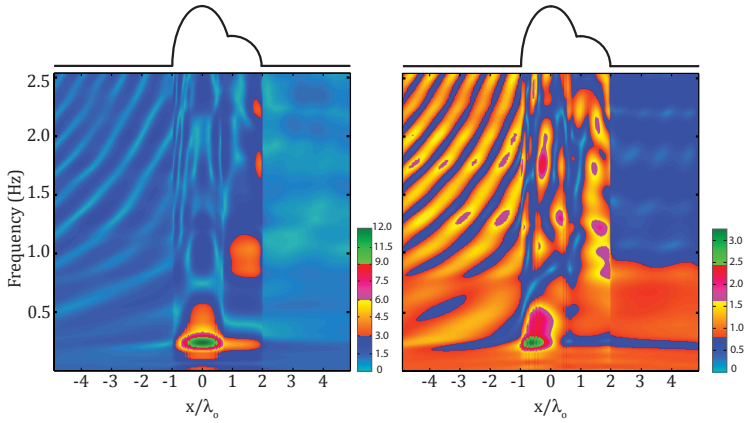

Figure 3.11: Transfer function amplitudes (TF) as function of position and frequency for both components of displacement. Horizontal component (left), Vertical component (right)

the physical response. Second, the stair-like boundary in which the proposed technique relies on, does not trigger any artificial source of scattered displacement by the corners of the external elements, otherwise, spurious high frequency oscillations would be noticeable in the displacement records. Both conditions establish reliability in the frequency characteristics of the signals in both amplitude and phase.

The foregoing examples are highly idealized due to characteristics such as their 2D nature, shapes of the surficial scatterers, and type of excitation. They, however, suggest that under the proposed modifications, quadtree-meshes i.e., stair-like external boundaries, can still be

used to represent realistic boundaries of external topographic irregularities with satisfactory accuracy.

Chapter 4

3D Verification. Virtual Topography Scheme

The verification of the proposed strategies for incorporating topographic features into seismic wave propagation takes on far greater significance in 3D simulations. For a strategy such as Virtual Topography (VT) to be accepted, it must not only be able to predict properly mode conversion effects, scattering, diffraction, and any other major wavefield characteristic, but it must also demonstrate its superior performance over the naive staircase approach. In this regard, this chapter is devoted to carrying out two simple parametric studies in order to illustrate the capabilities of the VT approach. The objective is to present results using VT, and to compare them with results previously reported by other authors. Of particular note will be to check the superior performance of VT in comparison with topography simulations based upon stair-shaped meshes. Topography modeling based upon stair-shaped meshes is perhaps the simplest strategy that one can follow. The inherent idea behind a staircase approach is that small enough element sizes will automatically lead to accurate results. This idea is by no means wrong, although it might necessitate an excessive mesh refinement. Therefore, quantitative evidence regarding its numerical performance will also be presented, as well as quantitative suggestions of the minimum number of points per wavelength (PPW) required to assure accurate results.

The performance of the VT approach is examined using two benchmark models. Namely, a Gaussian Hill subjected to a vertically incident SV-wave, and a Hermitian ridge subjected to a vertically incident P-wave. Both topographies are considered homogeneous and without intrinsic damping. In both simulations, the effective forces that drive the respective incident wavefields are computed based upon the Domain Reduction Method (DRM) (Bielak et al., 2003). Further evidence regarding the numerical stability of the VT approach is presented in terms of convergence tests.

4.1 Gaussian Hill.

The problem considered corresponds to a 3D Gaussian hill of homogeneous elastic material with P-wave V_p= 3200 m/s, S-wave V_s= 1847 m/s and density ρ = 2200 kg/m^3 (Fig. 4.1). The seismic source is a vertically incident SV-wave with a Ricker's pulse in time and a central wavelength $\lambda_s = 180$m ($f_c = 10.264$ Hz), polarized in the Y direction. The entire computational domain is 2km$\times$2km$\times$1km. Results are benchmarked with those reported by Komatitsch and Vilotte (1998), who use the spectral element method (SEM).

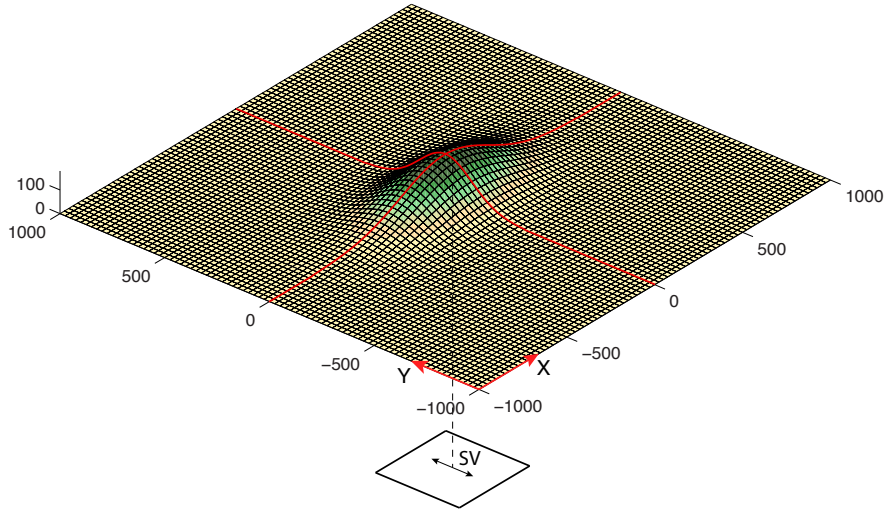

Figure 4.1: Gaussian mountain subjected to a vertically incident SV-wave polarized in the Y direction. The mountain is characterized by: $h_o \exp\left(-\frac{(x-x_o)^2}{2\sigma_x^2}\right) \exp\left(-\frac{(y-y_o)^2}{2\sigma_y^2}\right)$ where: h_o =180m, x_o=1000m, y_o=1000m, σ_x=250m, and σ_y=125m.

Figure 4.2 shows the portion of the mesh that contains the hill. The element size ($\Delta \mathrm{x} = 15.625\mathrm{m}$) corresponds to a prescribed refinement of PPW=11.52 PPW. As is clearly seen, the VT mesh preserves a distinctive staircase shape. Since VT is essentially a methodology to enrich the stiffness and mass matrices of the most external cubic elements, its mesh and the traditional stair-like mesh are visually equivalent.

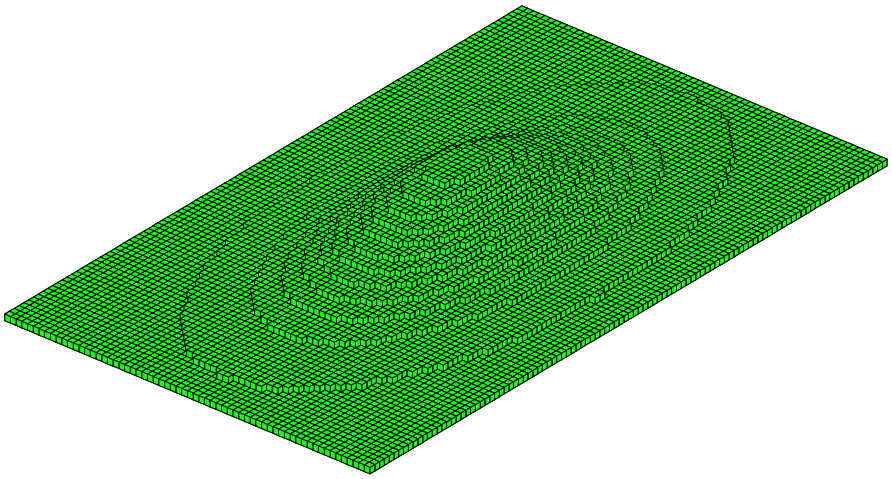

Figure 4.2: VT mesh for the homogeneous Gaussian mountain subjected to a vertically incident SV-wave. The computational domain is composed by elements of equal size $\Delta \mathrm{x} = 15.625\mathrm{m}$ ($\approx$ 12 PPW). In general, because VT relies in a stair-like background-mesh before computing the enriched mass and stiffness matrices, VT- and staircase-meshes are visually the same.

Synthetics of displacement for receivers placed throughout the minor and major axes of the ridge are presented in Fig. 4.3. The first column corresponds to the results reported by Komatitsch and Vilotte (1998). Results obtained by a traditional staircase scheme for meshes exhibiting different levels of refinement, i.e., 11.52–; 23.04–; and 46.08–PPW are depicted in the second, third, and fourth columns. The last column (5^{th} column) in Fig. 4.3 presents the synthetics of displacement obtained from the VT approach. A remarkable agreement is exhibited by the VT results when compared with the reference solution, and with that for the finest staircase mesh. Even more surprising is that such a level of accuracy was obtained with the same mesh resolution as in a traditional free-surface simulations.

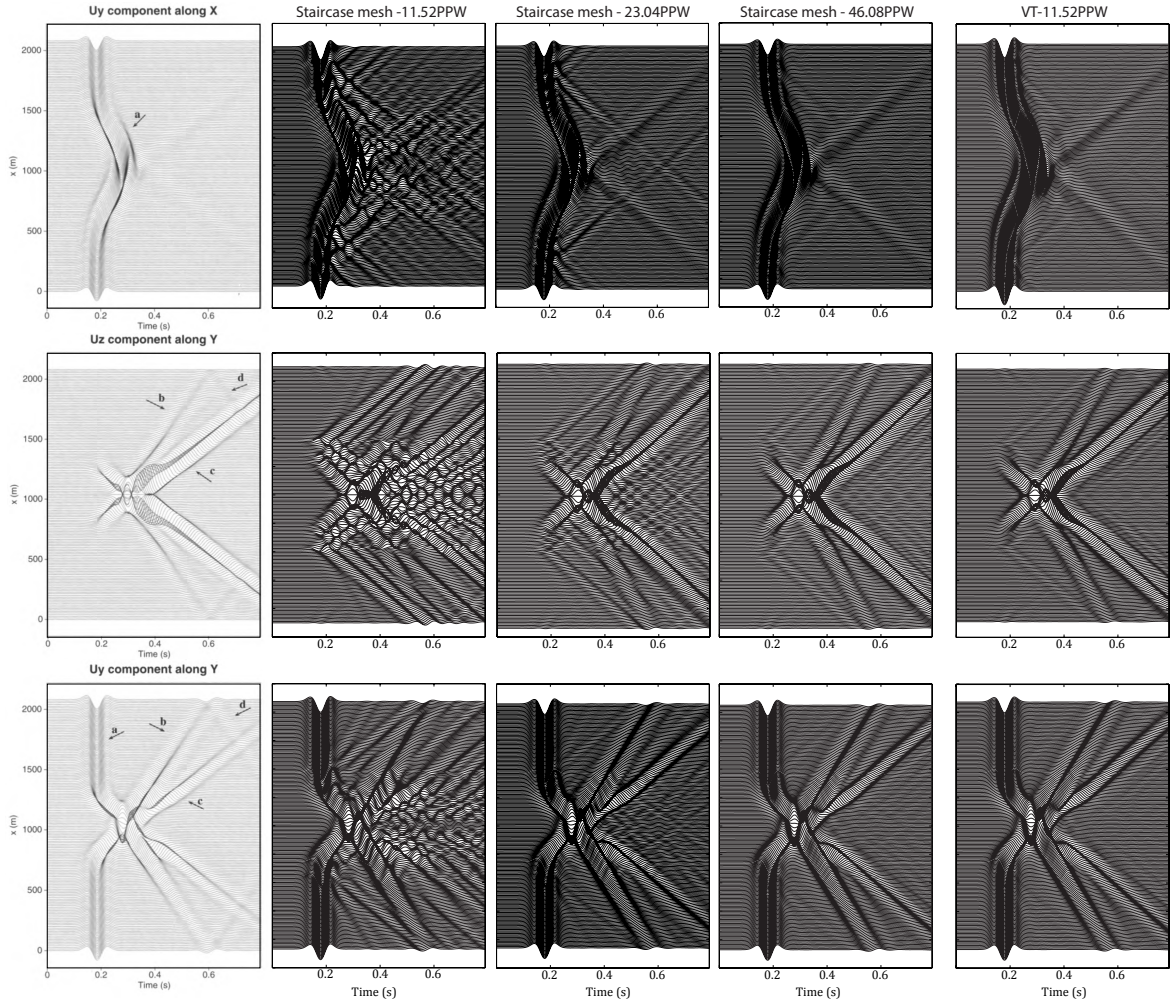

Figure 4.3: Histories of ground motion displacement from receivers placed at the free-surface of the Gaussian mountain (red lines in 4.1). First column depicts results reported by Komatitsch and Vilotte (1998). 2^{nd}, 3^{rd}, and 4^{th} columns represent results from stair-like meshes. The last column illustrates the results from the VT non-conforming scheme for a 11.52 PPW mesh.

The two diffracted phases created in the vicinity of the top of the mountain i.e., a P-wave, and a Rayleigh-wave are clearly identified by the VT results (see 3^{th} row on column 5th). In the same vein, the VT results seamlessly predicts the strong directivity effects exhibited by the 3D geometry of the topography as was pointed out by Komatitsch and Vilotte (1998). On the other hand, results from a stair-like approach using the same mesh resolution as in VT i.e., 11.52 PPW, creates strong artificial phases in every component of displacement (see 2^{nd} column of Fig. 4.3). These results are clearly unacceptable. By increasing the refinement of the staircase mesh to 23.04 PPW, the amplitude of the diffracted and scattered waves that were artificially created by the coarse mesh, exhibit now a considerable reduction although the degradation of the wavefields is still evident. This degradation is however not uniform. It appears that has a more significant effect over the X, and Z components than over the Y component. This can be seen as a hindering effect produced by the larger amplitude of the wavefields in the Y direction. A further refinement drives the staircase mesh to $\approx$50 PPW. For this kind of refinement a satisfactory match between results from VT and the solution reported by Komatitsch and Vilotte (1998) is finally reached.

Results from simulations based upon simple stair-like meshes require to go up to $\approx$50 PPW to obtain an accurate representation of the wavefields. This result is in agreement with findings from other studies where exceptionally high refinements are suggested. As an example, Ichimura et al. (2007) reported that in models where the external geometry follows a step-like pattern, the relative error in the Fourier components reaches 35 per cent even for mesh sizes of 1/60th of the minimum wavelength. For simple scenarios, such a level of refinement might not impose a significant constraint, especially with the computational capacity that is currently available. On the other hand, since doubling the number of PPW leads to an $8\times$ increment of the topographic elements, while simultaneously reducing by half the required time step of the overall simulation, a stair-shaped mesh tailor-made to accommodate $\approx$ 50 PPW would have $64\times$ more external elements that its $\approx$ 12 PPW counterpart. Additionally, such a mesh would demand a time-step reduction to 1/4

of the original time step. For end-to-end earthquake simulation, which generally demand vast computational resources, approaches based upon stair-like meshes clearly become cost prohibitive.

4.2 Hermitian Ridge

A second example is presented in Fig. 4.4. This problem was previously addressed by Sánchez-Sesma (1983). The topography corresponds to an axisymmetric isolated ridge of external profile $h(\xi) = h_o(1 - 3\xi^2 + 2\xi^3)$; $0 < \xi = \frac{r}{r_o} \leq 1.$; $h_o = 90$ m; and circular base $r_o = 180$ m. A vertically incident P-wave as a Ricker pulse in time of $f_c = 10$Hz, is considered as seismic source. The material properties of both, hill and half-space are: $V_p = 3600\text{m/s}$; $\frac{V_p}{V_s} = \sqrt{3.5}$; Poisson's ratio $\nu = 0.3$. Figure 4.5 illustrates the VT mesh (≈12 PPW) employed in the simulations.

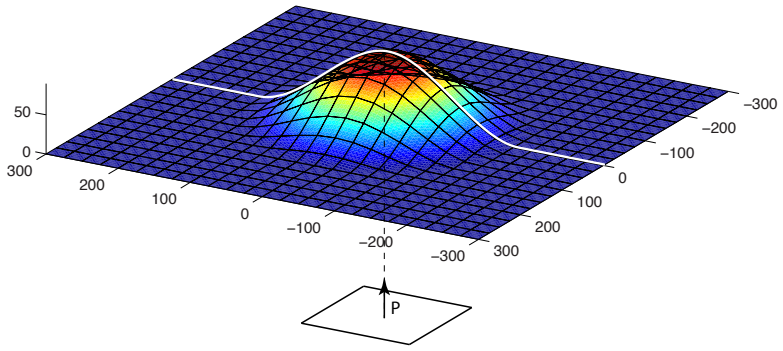

Figure 4.4: Isolated ridge subjected to a vertically incident P-wave. The ridge is a modest homogeneous hill of external profile $h_o(1 - 3\xi^2 + 2\xi^3)$; $0 < \xi = \frac{r}{r_o} \leq 1.$ h_o = 90m; circular base r_o = 180m. A vertically incident P-wave as a Ricker pulse in time of $f_c = 10$Hz, is considered as seismic source. The material properties of both, hill and half-space are: $V_p = 3600\text{m/s}$; $\frac{V_p}{V_s} = \sqrt{3.5}$; $\nu = 0.3$.

Sánchez-Sesma (1983) provided approximate solutions for one specific non-dimensional frequency of $\eta_q = \frac{r_o}{\lambda_p} = 0.5$, where λ_p represents the wavelength of the incident P-wave. In this verification, the time histories obtained by the VT scheme are further transformed to the frequency domain, and the Fourier amplitudes corresponding to $\lambda_p = 720\text{m}$ are normalized

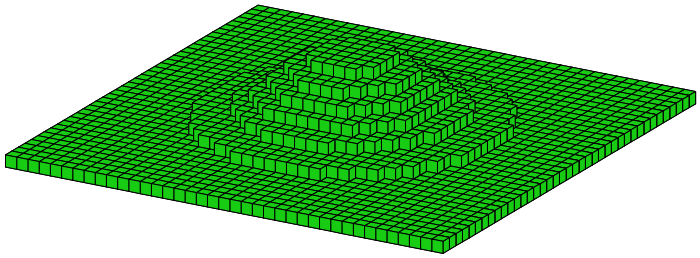

Figure 4.5: Finite element mesh of ≈12 PPW (Δx $=$ 15.625m) used for the numerical simulation of the isolated Hermitian ridge.

in order to compare them with the solutions from Sánchez-Sesma (1983). In general, results from both solutions are in good agreement as is depicted in Fig. 4.6. Regarding the vertical component, the pattern of amplification is exactly the same from both results, although VT results present slightly larger values that those from the reference solution in the ranges $\approx$ x$/r_o < 0.6$ and $\approx$ x$/r_o > 1.2$. For the horizontal Fourier amplitude, a larger deviation between the solutions is observed, although in general the VT results and the approximated reference solution are generally close.

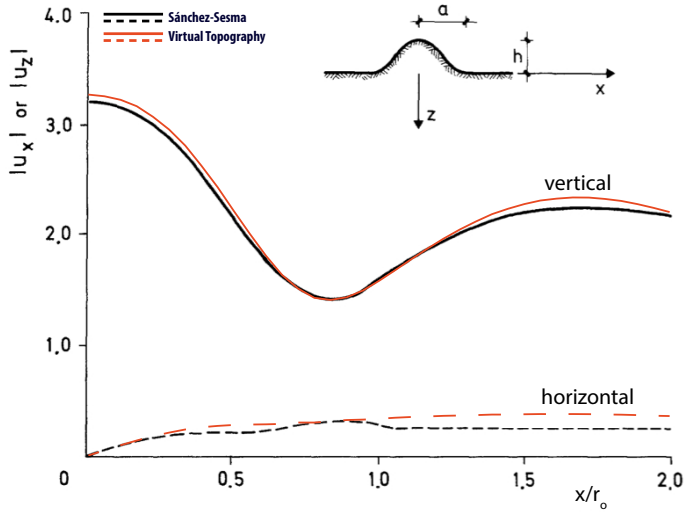

Figure 4.6: Comparison of the horizontal and vertical Fourier amplitudes at the free-surface of the ridge along the white line shown in Fig. 4.4 obtained from VT against the approximated results reported by Sánchez-Sesma (1983). The incoming wave is a vertically incident P-wave of wavelength $\lambda_p = 720$m. Results are presented as normalized distances (x/r_o) from the center of the ridge. The Fourier amplitudes come from histories of ground motion recorded at receivers placed along the white line at the free surface of the ridge (see Fig. 4.4).

A better insight of the characteristics of ground motion is gained by analyzing the synthetics of ground motion in Fig. 4.7. In terms of topography effects, the hill exhibits a modest effect on the free-surface motion. As can be seen, only two diffracted phases are created. These are clearly identifiable in the synthetics of horizontal component. The first phase (arrow a), is a diffracted P-wave. The second diffracted wave is a Rayleigh wave with a $1/\sqrt{r}$ decay. At the top of the hill the Rayleigh wave exhibits the dominant vertical amplitude. This amplitude reaches $1.3\times$ the free-field amplitude. Notice that the histories of displacement do not exhibit evidence of artificially created phases by the special treatment of the mesh.

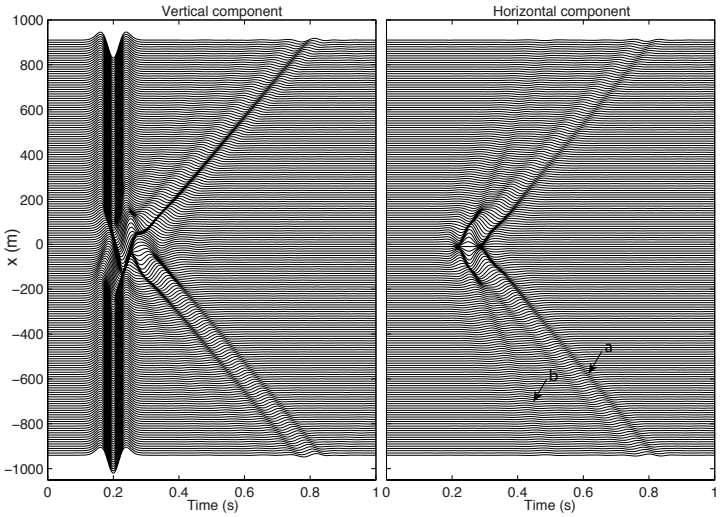

Figure 4.7: Synthetics of displacement at receivers placed at the surface of the Hermitian ridge along the white line shown in Fig. 4.4. At the top of the ridge two diffracted phases are created, a Rayleigh-wave (arrow a), and a P-wave (arrow b).

4.3 Convergence Analysis

The foregoing results have provided evidence that the so-called VT approach properly predicts the most important features of earthquake-induced ground motion. Moreover, computational efficiency has also been stated. These outcomes, however, still do not corroborate completely the performance of the methodology. There remain unanswered questions such as how fine must the mesh be in order to get an accurate representation of the solution.

Unfortunately, there is no theoretical solutions available for any 3D topography problem; thus, any attempt to exactly compute the error of the VT approach is still a distant goal. Fortunately, the exact quantitative evaluation of the numerical error is not essential for measuring the performance of numerical approaches. It is well established in numerical modelling that for a solution to be deemed to qualify as sufficient, the numerical approach followed must display a satisfactory convergence rate. Because of the latter, in the the following, some efforts will be devoted to compute convergence error bound estimates for the two parametric studies conducted so far.

The quantitative estimates of the convergence rate presented in Fig. 4.8 were obtained following Goto and Bielak (2008).

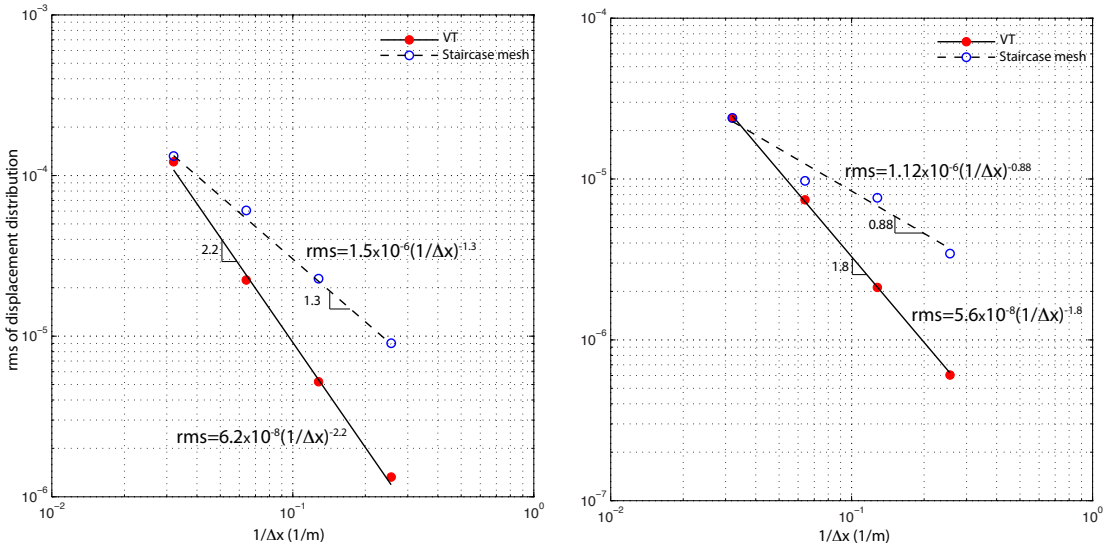

(a) (b)

Figure 4.8: Root-mean-square (rms) of surface ground motion vs the inverse of the element size Δx for the Gaussian mountain (a), and the Hermitian ridge simulations (b) respectively. In both figures, dotted regression lines and their associated hollow blue circles are the results obtained under staircase meshes conditions. Similarly, solid black regression lines and red circles correspond to results obtained by employing the VT scheme.

This technique allows to compute convergence rates of any response parameter even in the absence of an exact solution. In particular, the analysis will compute the root-mean-square (rms) difference of the ground motion distribution at the free-surface in the L2-norm

in space and time. As in any other norm measurement, the metrics are asymptotic error bounds, not absolute. Therefore, of particular note is the evaluation of the convergence rate instead of the error value per se. In order to estimate the error we obtained the spatial distribution of ground motion over the free-surface of each domain, from a hierarchical sequence of five (5) simulations each one conducted by doubling the number of PPW from the previous one. The starting, and final meshes correspond to regular grids $\approx$ 5PPW, and $\approx$ 80PPW respectively. The exact number of elements used in each simulation can be seen in the next table:

Gaussian Hill		Hermitian Ridge	
PPW	Number of Elements	PPW	Number of Elements
$\approx$5	109960	$\approx$5	108056
$\approx$10	846164	$\approx$10	827488
$\approx$20	6630334	$\approx$20	7522848
$\approx$40	52425958	$\approx$40	59518484
$\approx$80	473707504	$\approx$80	417038094

Table 4.1: Total number of elements for each one of the five (5) simulations conducted for the convergence analyses.

As is stated by the Goto and Bielak (2008) technique, the convergence varies according with a power law of the form $c\Delta \mathrm{x}^{-\kappa}$, where c is a constant, and κ is the convergence rate. The faster convergence of the VT approach is shown clearly in Fig. 4.8, and table 4.2.

	Gaussian Hill		Hermitian Ridge	
Method	c	κ	c	κ
VT	6.2×10^{-8}	2.2	5.6×10^{-8}	1.8
Staircase mesh	1.5×10^{-6}	1.3	1.12×10^{-6}	0.88

Table 4.2: Convergence rates for the VT- and the Staircase-based mesh methods for the Gaussian Hill, and the Hermitian Ridge respectively.

Surprisingly, the convergence rates of the VT in both simulations remain very close to each other, and around the theoretical value of 2. This occurs most likely because as the number of PPW increases, the tetrahedra elements of the VT approach tend to the traditional

approach of conforming the targeted geometry in a much more efficient fashion than the staircase condition. A very important conclusion is the low average convergence rate exhibited by the the models based upon stair-shaped meshes (1.09), which provides evidence of the poor behavior of the time histories of displacements in Fig. 4.3.

Chapter 5

The Region of Interest: The Aburrá Valley (Antioquia – Colombia)

5.1 Colombian Seismotectonic Setting

The tectonic environment of Colombia is controlled by the relative movement of three major lithospheric plates, i.e., the South American plate, the Nazca plate, and the Caribbean plate Fig. 5.1. The Nazca oceanic plate is converging eastward relative to the northwestern South America at 6-7 cm/yr, while the Caribbean plate moves 1-2 cm/yr to the E-SE relative to the South American plate (Freymueller et al., 1993; Kellogg and Vega, 1995). A consequence of this intracontinental deformation, which mostly occurred during the late Tertiary and early Quaternary times (París et al., 2000), are the two contrasting physiographic provinces of Colombia (Colletta et al., 1990). First, the Amazonas-Orinoco plain, also known as the eastern Llanos plain, is dominated by a very low flat relief (its maximum elevation hardly reaches 400m) of migmatitic and high-grade metamorphic rocks (Kroonenberg, 1980). Second, the Andean belt which is a deformed, faulted, and folded belt (París et al., 2000) resulted from a continuous process of subduction, obduction, and accretion of oceanic terrains in the western and northwestern margins of Colombia since the Paleozoic times (e..g., Bourgois et al., 1982; McCourt et al., 1984; Bourgois et al., 1987). Since the Andean Colombian range absorbs part of the relative movement between the

Nazca and the South America plate (Taboada et al., 1998), it is a larger contributor of the seismic activity of the country.

The Colombian Andes from west to east consists of three sub-parallel mountain chains, the Occidental, Central and Oriental Cordilleras. These ranges are usually oriented NS, and NE-SW following the contact boundaries of the plates. Volcano activity is mostly associated with the Central Coordillera where topography reaches up to 5500m. Two main geological domains divide the Colombian Andes. The first domain consists of accreted oceanic crust, which includes the Occidental, and western flank of the Central Cordillera (Restrepo and Toussaint, 1988). The second province is a continental deformed basement under the eastern flank of the Central and Oriental Cordilleras (Taboada et al., 2000). These two distinctive geological units are divided by the Romeral Fault System, which extends along the Cauca-Patía Intermontane Depression and the Central Cordillera.

Shallow seismicity in Colombia is mostly constrained to the Andes range, which exhibits a strong correlation with the borders of the Coordilleras (Pulido, 2003). According to París et al. (2000), approximately 47 Quaternary faults are associated with the Colombian Coordilleras. Two major faults, however, are traditionally associated with the largest share of the seismic activity of the country. First, the already mentioned Romeral Fault System (RFS) in the Central Coordillera. With a total length of almost 700 km, it consists of three or four regional fractures with a diverse movement regime due to its long extension (Pulido, 2003). South of $5°$N the RFS has a right-lateral movement related with the oblique subduction of the Nazca plate. North of $5°$N the sense of movement changes to left-lateral, apparently associated with the S-SE convergence of the Choco-Panamá Block (Taboada et al., 2000). Second, the Eastern Frontal fault system is the major geologic limit between the lowlands at the east, and the Andes range in the west. It consists of at least 10 sections with a combined length of 921.4 km that goes from Ecuador to the Venezuelan Andes in a

typical foreland fold and thrust belt setting (París et al., 2000). Seismic activity is mostly restricted to the border of the Oriental Coordillera.

Two subduction processes have a strong influence on the seismic activity of Colombia. Subduction regimes of the Nazca plate are accountable for shallow seismic activity (down to 80 km) along the Colombian trench at the Pacific coast (Vargas et al., 2007). The Nazca, Caribbean, and South America subduction process on the other hand, is a major contributor of deep seismic events in the country's interior (GSM, 2006). An important seismological feature is the high concentration of intermediate to deep earthquakes (≈150 km) originated at the Bucaramanga Nest as a result of an alleged inflection between the Caribbean slab subducted under South America plate (Malavé and Suárez, 1995; Taboada et al., 2000).

Another Colombian system of high seismic activity is the Murindó region. Located at the limit with Panamá, the seismicity of the region has been explained as a consequence of the existence of the North Andes and the Panama microplates (Pennington, 1981; Kellogg and Vega, 1995). GPS measurements give evidence that the North Andes and Panama microplates move independently with respect to the major plates at a convergence rate of 21mm/year (Kellogg and Vega, 1995). According to the Colombia strong motion network, the Murindó region is perhaps the country's most active area. Seismic activity during the 20th century reveals the occurrence of at least 10 $M_s \geq 6.0$ earthquakes, among them, the 18 October 1992 ($M_{\mathrm{W}} = 7.1$) Atrato earthquake which is the largest event registered in the area in modern times (Arvidsson et al., 2002).

5.2 The Aburrá Valley Seismic Setting

The Aburrá Valley (Antioquia, Colombia) is a moderate intra-mountain depression located at the north end of the central range of the Colombian Andean region. Variations in the surrounding mountains and plateaus can reach heights between 2200 to 3000 m.a.s.l., with

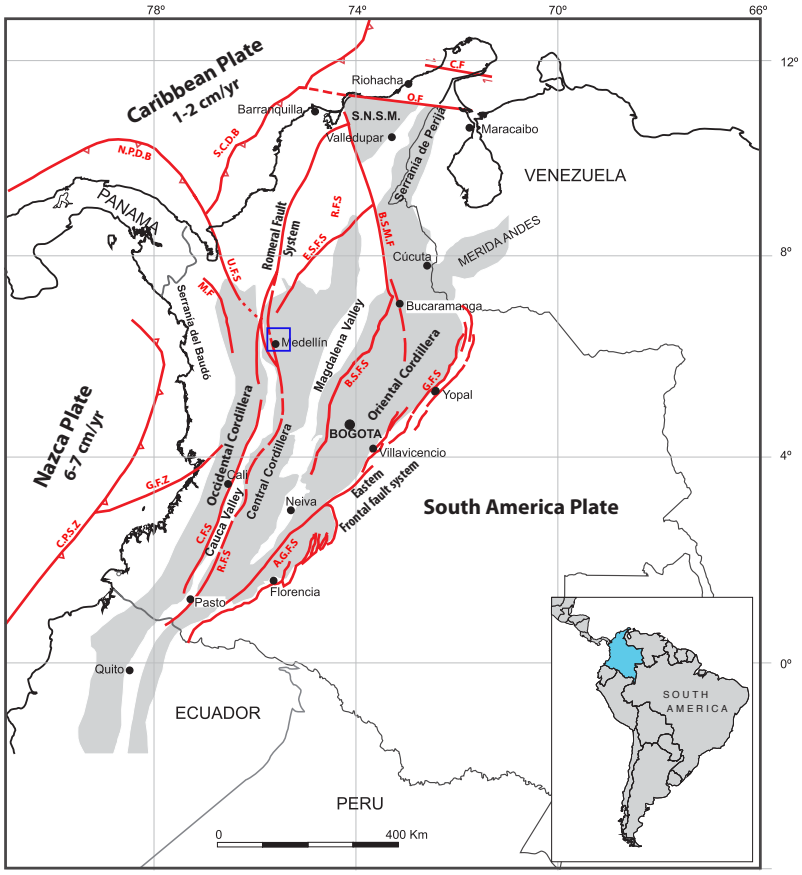

Figure 5.1: Colombia's major tectonic domains. The Nazca oceanic plate is converging eastward relative to the northwestern South America at 6-7 cm/yr, while the Caribbean plate is moving 1-2 cm/yr to the E-SE relative to the South American plate (Freymueller et al., 1993). Gray areas depict the major topographic units. Solid blue square represents the 50×50 km^2, 25 km deep, targeted domain for the 3D ground motion simulations of the Aburrá Valley region. In red are the regional faults: A.G.F.Z Algerias-Garzón fault system; B.S.F.S Buitama and La Salina fault system; B.S.M.F Bucaramanga Santa Marta fault system; C.F. Cuiza fault; C.F.S. Cauca fault system; C.P.S.Z. Colombian Pacific Subduction Zone; E.S.F.S Espiritu Santo fault system; G.F.S. Guaicáramo fault system; G.F.Z. Garrápatas fault zone; H.E. Hess Escarpment; M.F. Murindó fault; N.P.D.B. North Panama Deformed Belt; O.F. Oca fault; R.F.S. Romeral fault system; S.C.D.B. South Caribbean Deformed Belt deformation front; U.F.S. Uramita fault system. Modified map from Barrero et al. (2007).

its lowest level located at 1300 m.a.s.l. The valley's geological setting is composed of (i) a Paleozoic metamorphic basement, (ii) ultrabasic igneous rocks, (iii) a volcano-sedimentary sequence, (iv) intrusive granitoid bodies, and (v) hillslope and alluvial sediments (Maya and Gonzales, 1995). According to Aristizábal et al. (2005), the valley can be divided into three broad geomorphologic sectors: a central portion that consists of broad alluvial plains

bounded by moderate to gentle slopes; whereas the northern and southern parts consist of narrow asymmetric valleys bounded by steep slopes. The Medellín river and its two main tributaries, the Santa Helena and Iguaná streams, have deposited most of the alluvial deposits in the central and lowest portions of the valley, which vary between 3 to 200 m in depth (Adams and Jaramillo, 2002). The steep slopes and most elevated parts of the valley are covered by a thick weathering profile. Depths of these weathered profiles and local conditions vary with position. They are thicker usually at gentle slopes, and become shallower on steep slopes as consequence of erosion (Aristizábal et al., 2005).

Historic records from 1730 report 39 seismic events felt in the city of Medellín with intensities larger than III on the Modified Mercalli (MM) Scale, five of them located under the city of Medellín with Mercalli values from III to V (Ramírez, 1975). Recent seismic activity of relevant intensity for the city of Medellín has been limited to destructive far-field earthquakes (>180 km). The 12 December 1979 Tumaco ($M_{\mathrm{W}} = 7.2$) earthquake, and the 18 October 1992 ($M_{\mathrm{W}} = 7.1$) Atrato earthquake, registered rock PGA of 0.03g, and 0.015g respectively (Adams and Jaramillo, 2002). The 25 January 1999 Eje Cafetero ($M_{\mathrm{W}} = 6.2$), Armenia earthquake which ruptured along a segment of the Romeral Fault System in the Eje Cafetero area, was also felt with important intensity in the Aburrá region.

Colombian seismic regulations estimate a moderate seismic hazard for the Aburrá Valley region (NSR-10, 2010). Geological evidence, however, suggests an important tectonic activity along its main structural systems. In average, each one of the ten municipalities of the metropolitan area of the Aburrá Valley are less than 25 km from a potentially active $M_{\mathrm{W}} = 7$ seismic fault. Of particular note, the Romeral fault system is just 5 km from the municipality of Caldas, and only 15 km from the city of Medellín. A rupture along a nearby segment of the Romeral fault is regarded as the worst-case scenario for the region where PGA up to 0.4g are expected (GSM, 1999). Evidence from recent seismological

surveys indicates that PGAs for a return period of 475 years is dominated by near sources ($\approx 15 - 20$ km) of moment magnitudes $M_{\mathrm{W}} = 6.5$ (GSM, 2006).

5.3 Source and Material Models

In order to be able to perform simulations of ground motion due to potential scenario earthquakes in a region of interest, one needs to first model the potential source and the crustal velocity characteristics of the material within the region. Because the final goal in numerical modelling is to reasonably predict ground motions from recognized seismic sources, both of these models must be as realistic as possible, and capture the most important aspects of their respective processes. In the following, the strategies adopted for the Aburrá Valley region regarding these two inputs will be described. The strategy presented is by no means a final representation of the sesimic characteristics of the region. nonetheless, these strategies, although still approximated, can provide significant insights regarding the expected seismic risk of the area, and are important first steps towards better understanding of earthquake-induced ground motion throughout the region.

5.3.1 Romeral Fault Rupture Scenarios

To investigate the ground motions in the Aburrá Valley Region (ABR) and, specifically, to further illustrate the combined effect of topography, plus near-source rupture scenarios, we propose to analyse the $50\times50\times$ km^2, 25 km deep region shown in Fig. 5.2. This region covers the entire ABR metropolitan area, and several other municipalities of regional importance such as the municipality of Rionegro located 22 km east the city of Medellín. Furthermore, this volume is large enough to include every major topographic irregularity throughout the region, and several rupture scenarios from the Romeral Fault, which, as was previously mentioned, would drive the worst-case scenario in the ABR, if ruptured.

The segment of the Romeral fault enclosed in the proposed domain however, presents long return periods. As a result, strong motion events have not been recorded from this segment thus far, nor have realistic kinematic models been developed for the region either. In the present simulations the effects of the rupture front are obviated by assuming earthquake events of low magnitude ($M_{\mathrm{W}} = 5.0$), which can accurately be modelled as double-couple kinematic point sources. The main purpose of the simulations is to gain insight into the spatial distribution of the ground motion and to examine the effect of topography on it.

We simulate the 3D wave field generated by four source scenarios. All of them assume a Ricker's pulse source time function of maximum frequency f_{max}= 5 Hz, average strike of 160° consistent with the direction of the Romeral fault in our domain, and depth of 10 km. The remaining parameters chosen as representatives of: left-lateral strike-, thrust-, and oblique-faults respectively Fig. 5.2:

Event	Strike°	Dip°	Rake°	Long (E)	Lat (N)	Depth (km)	Foc Mech.
1	160	90	0	831,024	1,163,562	10	
2	160	90	0	819,828	1,196,764	10	
3	160	20	90	827,633	1,172,945	10	
4	160	20	30	824,299	1,184,232	10	

Table 5.1: Double-couple point sources parameters. Latitude and longitude are expressed in the Colombian local coordinate system: 1,000,000N (4°35'56.57"N); 1,000,000E (74°4'51.30"W).

5.3.2 3D Seismic Velocity Model

End-to-end ground motion simulations largely depend upon accurate 3D regional models that define the material properties of the targeted region. Regarding the ABR, to date there has been no attempt to develop a 3D seismic velocity model, nor a unified database defining the internal velocity gradient of the soil deposits throughout the area. Since large-scale

3D ground motion simulation is still an unexplored field in the ABR, scientists have not addressed this problem yet. Soil data collected from two microzonation studies (GSM, 1999, 2006) is perhaps the closest alternative to such a unified database. Graduate projects, and data from engineering companies around the region are also relevant sources of information, although are available mostly in a scattered fashion. During the fist two years of this study, some of these information was gathered and analized in order to build the first version of a velocity model for the region. This effort was done in partnership between the Applied Mechanics Research Group at Universidad EAFIT, and the Quake Group at CMU.

The first version of the Initial Seismic Velocity Model for the Aburrá Valley Region (IVM-AbV) takes the work of Acevedo (2011) as a point of departure. The reference work establishes the internal geometry of the geologic structures, their presumable contact, and eventual deep geologic formations based upon information from local geological studies

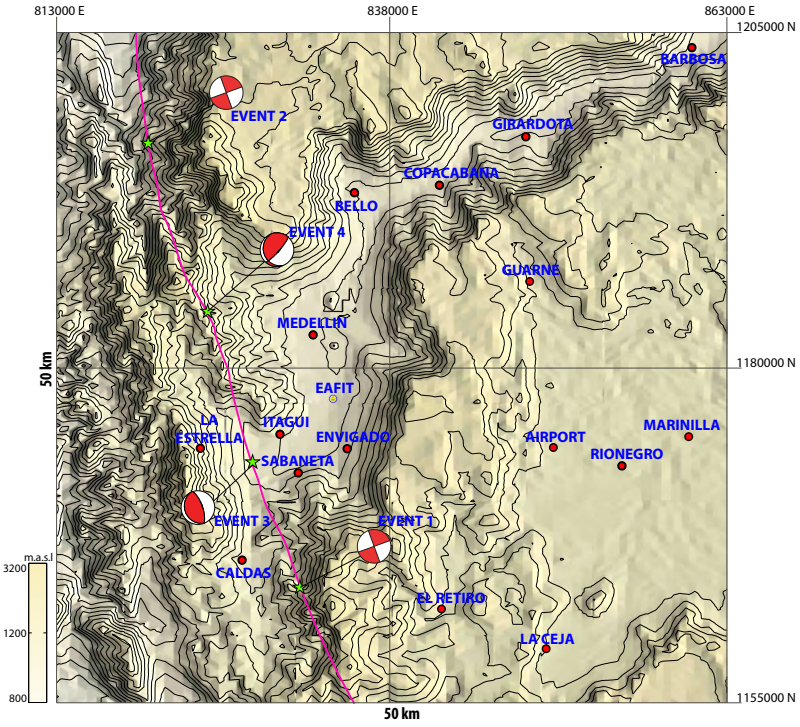

Figure 5.2: Topographic map indicating the 50 km×50 km region of study. Red dots represent the most important municipalities within the region. Magenta line illustrates the segment of the Romeral fault that crosses the region. Stars represent the epicenters of the four 10 km deep rupture scenarios. Beach balls depict the focal mechanisms.

and geophysical data throughout the region. The reference study renders the most likely geological setting, including the terrain elevation through north-south vertical sections every 2 km over a nearly rectangular area of 49.541×40.5 km^2, and extends 30 km in depth. EAFIT's group incorporated the data from these vertical sections into a computer algorithm designed to identify the corresponding geologic unit enclosed by two adjacent sections. The proposed velocity model was built following the same features of similar models (e.g., Magistrale et al., 2008). That is, any material point within the region is queried by latitude, longitude and Z, where Z is the elevation in meters above sea level. Because the proposed region will be slightly larger than the original region covered in the reference study, a fictitious geological structure located at the bottom and left sides of the domain was incorporated into the IVM-AbV in order to fill out this specific zone.

The proposed IVM-AbV then, takes geology as a proxy for shear wave velocity characterization. The use of lithology structures to determine shear-wave velocity and soil-site characterization has been used in numerous studies where even empirical relationships have been proposed for ground-motion amplification studies (e.g., Park and Elrick, 1998; Field and the SCEC Phase III Working Group, 2000; Wills et al., 2000). To correlate geology with wave speed appears as the natural step to follow. This is mainly because quantitative measurements of shear velocity are usually expensive (Field and the SCEC Phase III Working Group, 2000). This impose an important constraint because high-resolution wave velocity models require highly oversampled regions. An example is the velocity model developed by Süss and Shaw (2003) for the Los Angeles basin. This model was based on more than than 85,000 direct measurements from petroleum-industry boreholes and seismic reflection profiles. Attempting a similar work is clearly out of the scope of this work, and becomes a future challenge for the ABR.

Figure 5.3 depicts the free surface shear wave velocities according to the IVM-AbV . As is readily seen, the velocity model reasonably detects the Quaternary deposits along the

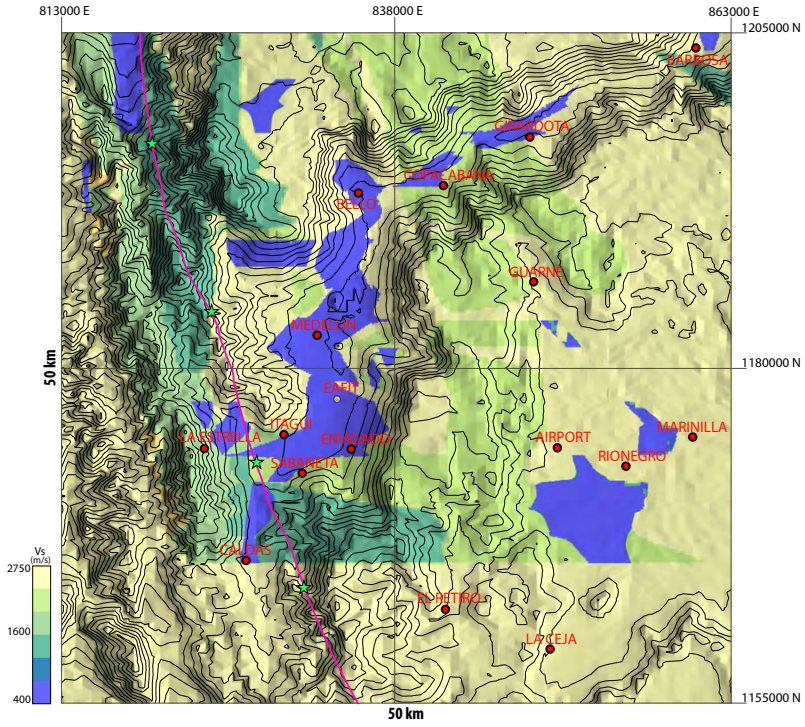

Figure 5.3: Plane view of S-wave velocity at the surface of the targeted domain. The initial velocity model reasonably detects the softer deposits of alluvial sediments (V_s=400 m/s) along the Medellín River bed, as well as the softer soil deposits at the San Nicolas Valley (see the Rionegro region at the center of the bottom right hand side quadrant). Of particular note is the apparent high contrast between the geological units that surround the soft-soil deposits.

Medellín River bed. Softer soil deposits at the San Nicolas Valley (SNV) are also detected (see the Rionegro region at the center of the bottom right hand side quadrant). The slowest shear-wave velocity in the regional model corresponds to these Quaternary deposits (V_s =400 m/s). Compressional velocities are computed by assuming a constant Poisson's ratio in every geologic unit of $\nu = 0.3$. Throughout the entire domain, the density is constrained to lie between 2000 and 3000 kgf/m^3. In this first approximation, we obtained Fig. 5.3 by assuming a homogeneous behavior of the seventeen geologic units in the reference study. This can be seen as an average scheme of any soil heterogeneity around the region. The mechanical properties of each homogeneous body were based upon proposed estimates according to the type of the geological unit. As reported by Hartzell et al. (1997), deeper geologic formations can have a significant or even larger impact over the ground

motion at a given location than shallow shear wave velocity. The homogeneous bodies assumption, preserves the high complexity, heterogeneity, and prominent internal geometric variations of the geological setting which underline possible focusing effects within the region.

Another important aspect is the treatment of topography in the velocity model. Presently, extensively used velocity models such as the Community Velocity Model of the Southern California Earthquake Center (CVM-S) disregard topography by artificially flattening the free surface. This, as a result, modifies the contact between adjacent geologic units. Our proposed velocity model incorporates the region's topography by means of a 50 m grid resolution elevation model. This significant improvement allows the correct representation of near-surface material interfaces, which, once again, drives a more realistic representation of focusing effects throughout the region.

Chapter 6

3D Earthquake Ground Motion Simulations of The Aburrá Valley Region

In order to accommodate the surface topography of the Aburrá Valley Region (ABR) as well as the heterogeneous material model of the initial velocity model of the Aburrá Valley region (IVM-AbV), the numerical analyses will use the Virtual Topography (VT) scheme presented in Chapter 2. In particular, a complete analysis will be performed for each of the double-couple point source scenarios proposed. This gives a total set of four simulations. This relatively large number of simulations will allow to investigate topographic effects on seismic-induced ground motion in conjunction with variations in the source focal mechanisms. Special attention will be given to comparing topographic amplification factors from each rupture scenario. Several parameters of engineering interest such as peak ground velocity (PGV), and peak ground acceleration (PGA), will be computed for every simulation. Different stations throughout the region will also be examined to study local changes in ground motion. Of particular importance will be the analysis of the motion at stations located within the ABR strong ground motion network. An important aspect to be addressed is the extent to which surface topography modifies the amplitude, and frequency characteristics of ground motion of stations located at the base, slopes, and the tops of mountains.

To further examine topography effects, we will conduct an additional series of simulations. The second numerical scenario considers the same four rupture sources but, is performed under classical modelling conditions. That is, traditional large-scale earthquake simulations disregard surface topography by artificially making the free surface flat. Flat-surface approximations are based on either "squashed" or "bulldozed" velocity models (Aagaard et al., 2008). The squashed surface approach levels the top surface at a certain elevation but retains the original thickness of the top layer (Quinay et al., 2012). Bulldozing the surface of the earth on the other hand, strips away any material above some elevation and fills in any voids below this elevation with some generic material (Aagaard et al., 2008). In general, there are no physical bases for any of the two options. Here, the squashed approach is favoured mostly because it preserves the spatial distribution of the material properties at least at the free-surface level.

In the third, and final set of numerical simulations, we isolate the effects of topography. We achieve isolation of topographic effects by considering the realistic topography and simplifying the 3D velocity structure of the IVM-AbV as if it were a homogeneous domain of average material properties: $V_s = 2000$ m/s, $V_p = 4000$ m/s, and $\rho = 2200$ kg/m^3. Again, we consider the four rupture scenarios already mentioned. Parameters of interest will be computed, and comparisons between results will be provided accordingly.

Twelve large-scale numerical simulation were then performed for the ABR, i.e., 4 rupture scenarios $\times$ 3 velocity structure models. Table 6.1 presents the details of the simulations parameters, and the computational resources used.

	3D Velocity Structure		
Analytics	IVM-AbV	Squashed (SQD)	Homogeneous (HMG)
$f_{\max}$	5.0 Hz.	5.0 Hz	5.0 Hz
Topography	Yes.	No.	Yes.
$V_{s\min}$	400 m/s	400 m/s	2000 m/s
PPWL	13.1	13.1	16.3
Min. elem. size	6.10 m	6.10 m	24.41 m
Num. of elements	4,617,025,557	4,181,610,745	3,058,335,221
Num. of nodes	4,707,518,437	4,198,489,003	3,066,223,684
Time step Δt	0.0005 s	0.0005 s	0.0025 s
Sim. time	30 s	30 s	30 s
Num. of cores	9960	9960	3960
Cores usage time	5 hr, 27 min	4 hr, 38 min	1 hr, 42 min

Table 6.1: Summary of simulation parameters and input data. All simulations were run in Kraken, the Cray XT5 parallel supercomputer at the National Institute for Computational Science; US.

6.1 Regional Effects

6.1.1 Wavefields Propagation

We begin to explore the general characteristics of the ground motion by examining snapshots of the vertical (Z) component of the velocity wavefield for each synthetic M_{w}=5.0 earthquake event. Figure 6.1 illustrates the time evolution of the velocity wavefields for the first event. At $t = 3.5$s, the arrival of the first P-waves is apparent in the three models. Results from the HMG simulation preserve the expected P-wave radiation pattern associated with a double-couple strike-slip source, with only minor modifications from the surrounding topography (Fig. 6.1(g)). Conversely, for the IVM-AbV and the SQD models no recognizable radiation pattern is preserved whatsoever. In both simulations the internal velocity gradient dramatically modifies the spatial distribution of the first arrivals, (see Figs., 6.1(d), and 6.1(a)). When these two models are compared between each other their results generally resemble (see Figs., 6.1(d), and 6.1(a)). Although the SQD wavefields

exhibit a smother distribution. The first sign of ground motion modifications due to topographic effects is seen at the top of the mountain between the municipalities of Caldas, and La Estrella.

At $t = 7.5$s a clear S-wave has already reached the surface. Since S-waves exhibit smaller wavelengths than P-waves, their interaction with external irregularities become more important. An example of this interaction is clearly seen from the HMG results. As Fig. 6.1(h) shows, the ABR topography creates an extremely complex pattern of reflected and scattered wavefields as the S-wave travels throughout the domain. Even stronger complexities are exhibited by the wavefronts of the SQD, and the IVM-AbV simulations (see Figs. 6.1(b), and 6.1(e)). In the case of the SQD model, these wavefront distortions are consequence of the low wave-speed velocity Quaternary deposits plus geometric effects from the geologic units. These effects are also present in the IVM-AbV simulations; however, as the larger number of saturated areas presented in Fig. 6.1(b) suggests, the wavefront distortions are larger in the IVM-AbV simulations as a consequence of the ABR topography. Regarding the P-wave, it appears that under homogeneous conditions the ABR topography only creates a minor change in the shape of the wavefront with respect to the zero-topography case. The latter is explained because under no surficial topography the wavefront is a concentric circle with origin at the epicenter. This is almost the case in Fig. 6.1(h). The only noticeable topographic effect is the trace of reflected, and scattered waves left behind the P-wavefront as it moves forward.

As the dynamic phenomenon continues a large amount of energy gets trapped in the domain (see Figs. 6.1(c), 6.1(f), 6.1(i)). A heavily distorted, yet, still S-wave, keeps moving forward in the HMG model (see Fig. 6.1(i)). The P-wavefront on the other hand, has already left the domain although the scattered waves created by the ABR topography are still present. By contrast, substantial variations in the 3D structure are largely responsible for the trapped energy and wave reverberations exhibited by the SQD model (see Fig. 6.1(f)).

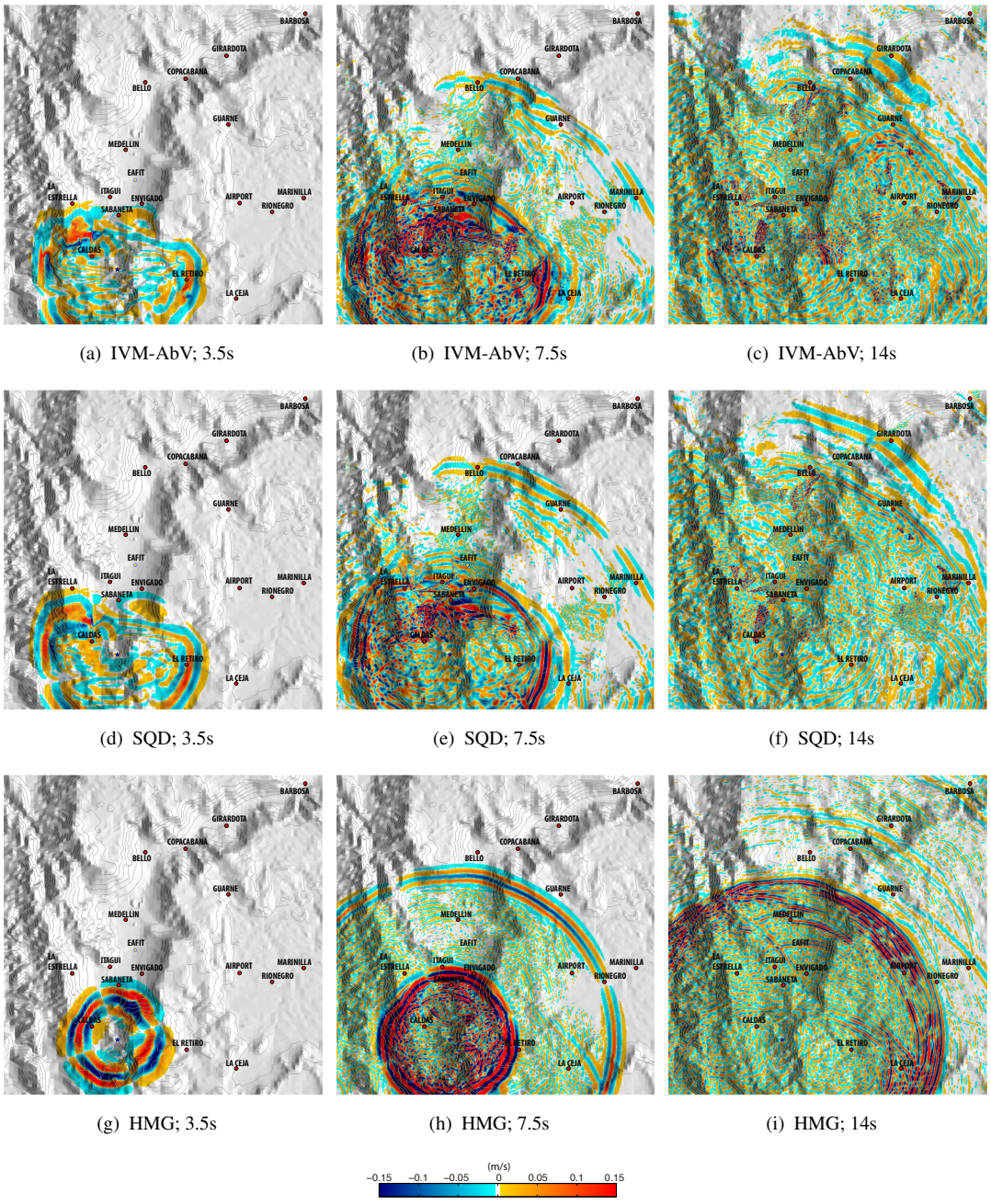

(a) IVM-AbV; 3.5s (b) IVM-AbV; 7.5s (c) IVM-AbV; 14s

(d) SQD; 3.5s (e) SQD; 7.5s (f) SQD; 14s

(g) HMG; 3.5s (h) HMG; 7.5s (i) HMG; 14s

Figure 6.1: Snapshots of the vertical component of the velocity wavefield for the IVM-AbV (Figs., 6.1(a), 6.1(b), 6.1(c)), SQD (Figs., 6.1(d), 6.1(e), 6.1(f)), and HMG (Figs., 6.1(g), 6.1(h), 6.1(i)) models. Columns represent time steps at 3.5s, 7.5s, and 14s respectively. The blue star illustrates the epicenter of the 1st rupture scenario (see Table 5.1 for the epicenter location).

The IVM-AbV model also exhibits effects from the 3D velocity structure although topography effects are again visible. For instance, near the Rionegro and Guarne municipalities,

clear amplifications are noticeable in Fig. 6.1(c). It is important to point out that these municipalities are located at elevated regions compared with that of the epicenter. Therefore, amplification by topographic effects in those areas is consistent with previous findings.

The second simulated earthquake also represents a strike-slip fault rupture, therefore, it shares some similarities with the previous results. In general, HMG results show more clearly the first, and second arrivals than the IVM-AbV or the SQD simulations (Figs 6.2(g), and Fig. 6.2(h)). The epicenter of the second source scenario however, is dominated by a local topography of larger gradients than the first event. This explains in part the larger spatial variability of the radiation patterns during the first stages of the rupture process for the second event. Once again, the effects of the ABR topography over the first, and second arrivals is characterized by complex patterns of reflected and scattered energy. Interestingly, at $t = 7.5$s, results from the SQD, and the IVM-AbV models are very similar. This coinciding behavior is no longer true at $t = 14$s. Here, a closer look at Fig. 6.2(c) shows the presence of topographic effects in the form of a larger number of saturated areas at the top/slopes of the topography near the epicenter.

Source radiation patterns of higher complexity are exhibited by the third, and fourth source models as a result of changes in the direction of the fault movement. Consequently, phases of larger amplitude dominate the seismic response since the beginning of the ground shaking (Figs. 6.3, and 6.4). The strong P-wave seen at $t = 3.5$s is evidence of the latter. Its large amplitude, in combination with the proximity of the epicenters, generate an early response of the Quaternary deposits from the Caldas municipality up to Universidad EAFIT (see Figs. 6.3, and 6.4 at $t = 3.5$s). In general, topography only exhibits a small effect in the IVM-AbV simulation. Source-radiation, and basin effects are the predominant effects during the first stages of the shaking.

Again, the effects of the ABR topography are exposed more clearly by the HMG results. At $t = 7.5$s, the P-wave continues moving forward with an evident circular shape (Fig. 6.3(h)).

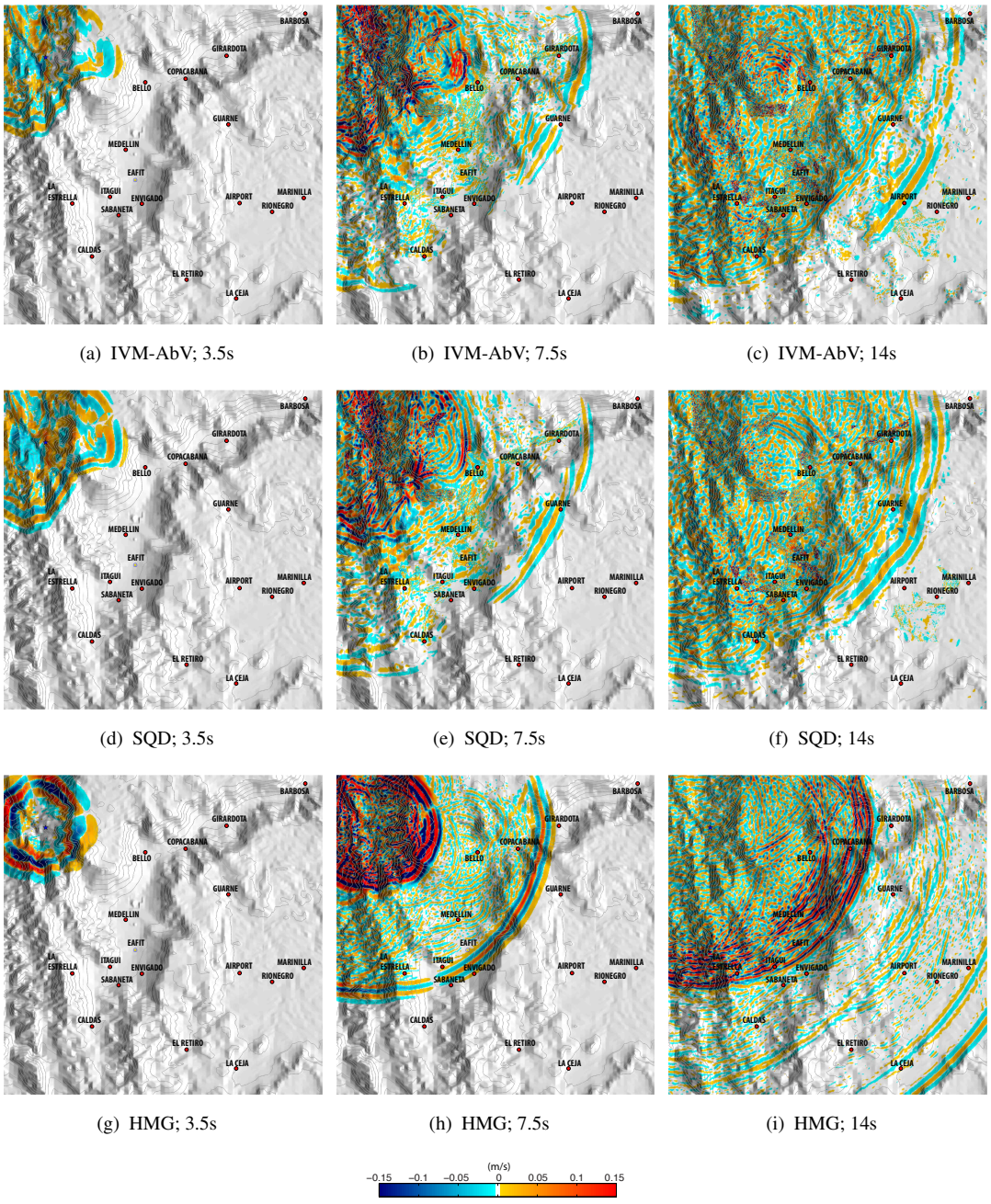

(a) IVM-AbV; 3.5s (b) IVM-AbV; 7.5s (c) IVM-AbV; 14s

(d) SQD; 3.5s (e) SQD; 7.5s (f) SQD; 14s

(g) HMG; 3.5s (h) HMG; 7.5s (i) HMG; 14s

Figure 6.2: Snapshots of the vertical component of the velocity wave field for the IVM-AbV (Figs., 6.2(a), 6.2(b), 6.2(c)), SQD (Figs., 6.2(d), 6.2(e), 6.2(f)), and HMG (Figs., 6.2(g), 6.2(h), 6.2(i)) models. Columns represent time steps at 3.5s, 7.5s, and 14s respectively. The blue star illustrates the epicenter of the 2^{nd} rupture scenario.

Interestingly, for the fourth rupture scenario, the top of the eastern flank of the topography near the Copacabana, and Girardota municipalities trims down the concentric shape of the first arrival (see Fig. 6.4(h)). As in previous analyses, the effects of the ABR topography to

the first arrivals is limited to the generation of small amplitude surface waves. Regarding the effects over the S-wave front, results of the simulations show that most of the scattered energy is carried by high-frequency surface waves, which concentrates along the mountains near the Romeral fault. Figure 6.4(h) provides a compelling example of such a cluster of surface waves. On the other hand, when the 3D velocity structure is considered, its effects remain dominant over the ABR topography at $t = 7.5$s (see Figs. 6.3(b), 6.3(e), 6.4(b), 6.4(e)). Larger spatial variability is in general exhibited by the IVM-AbV simulations.

At $t = 14$s on the other hand, the complex geometry of the surficial topography in the ABR greatly affects the characteristics of ground motion. The S-wavefront is significantly distorted and amplified as it passes through the Aburrá Valley depression, and moves toward the San Nicolas Valley (SNV) as is seen in Figs. 6.3, and 6.4. As the Fig. 6.4(c) clearly shows, important contributions from the Quaternary deposits of the San Nicolas are already present. The SQD model also presents basin response at the SNV, although to a lesser extent (see Fig. 6.4(f)). Of greater relevance are perhaps the differences of the incoming, high-energy wavefront predicted by the SQD, and the IVM-AbV models. According to the SQD model, there is only one large energy wavefront followed by a cluster of small intensity wavefields. By contrast, the IVM-AbV results predict the same initial wavefront, but these are followed by high energy wavefronts of the same intensity. As it can be readily inferred, when the Romeral fault ruptures as the third, or fourth hypothetical events, the response of the Quaternary deposits of the SNV will be more strongly affected by the ground motion from the IVM-AbV model than from traditional SQD simulations.

6.1.2 Topographic Amplification Factors

Observations regarding the impact of the ABR topography take more significance if one examines quantitative evidence in terms of topographic amplification factors (TAF). The

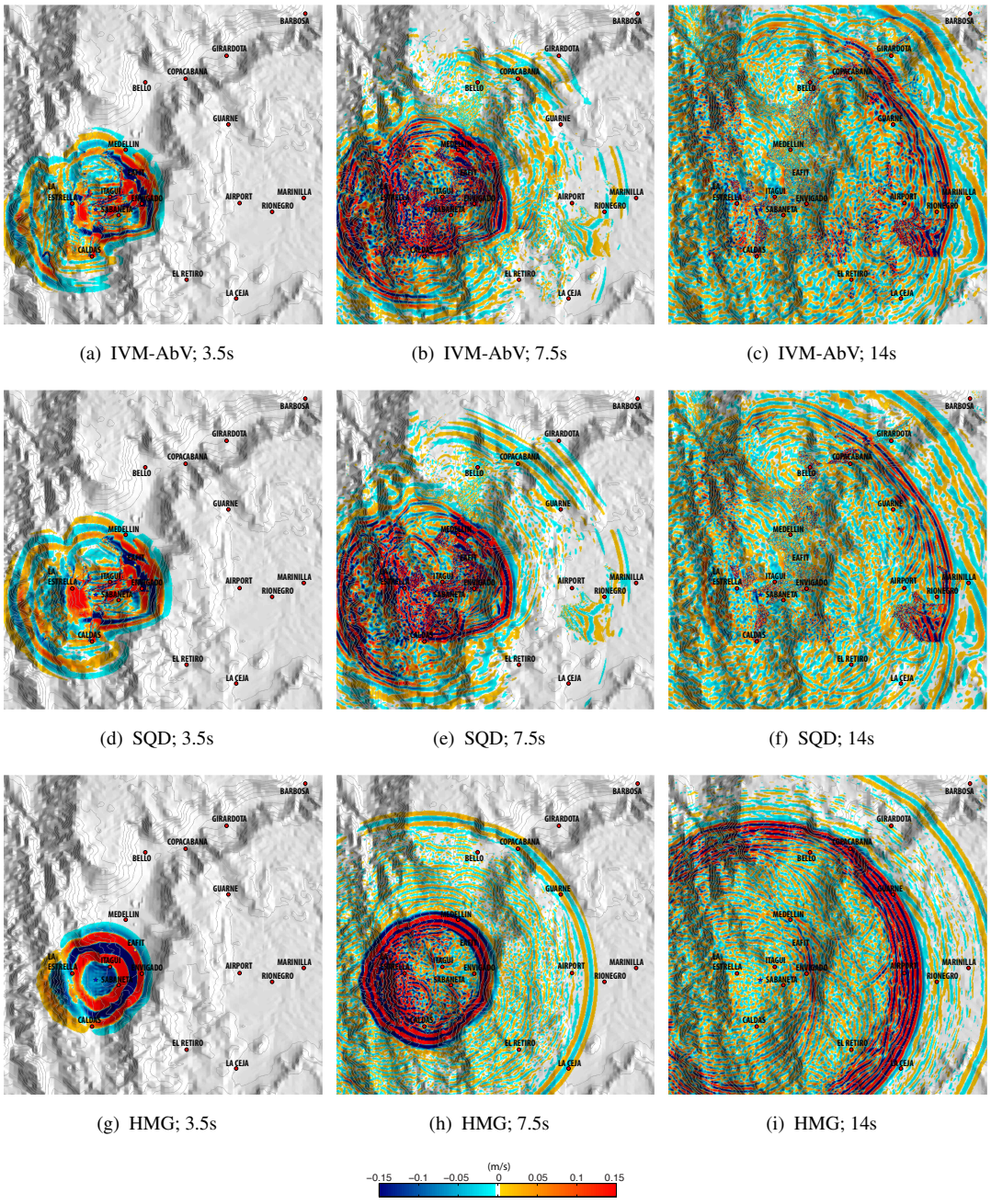

(a) IVM-AbV; 3.5s (b) IVM-AbV; 7.5s (c) IVM-AbV; 14s

(d) SQD; 3.5s (e) SQD; 7.5s (f) SQD; 14s

(g) HMG; 3.5s (h) HMG; 7.5s (i) HMG; 14s

Figure 6.3: Snapshots of the vertical component of the velocity wave field for the IVM-AbV (Figs., 6.3(a), 6.3(b), 6.3(c)), SQD (Figs., 6.3(d), 6.3(e), 6.3(f)), and HMG (Figs., 6.3(g), 6.3(h), 6.3(i)) models. Columns represent time steps at 3.5s, 7.5s, and 14s respectively. The blue star illustrates the epicenter of the 3rd rupture scenario.

site-to-reference spectral ratio method (SRM) (Borcherdt, 1970) is the strategy most commonly used to estimate topographic site effects (e.g., Tucker et al., 1984; Çelebi, 1987; Pedersen et al., 1994). In general, the SRM assumes that the only difference between the

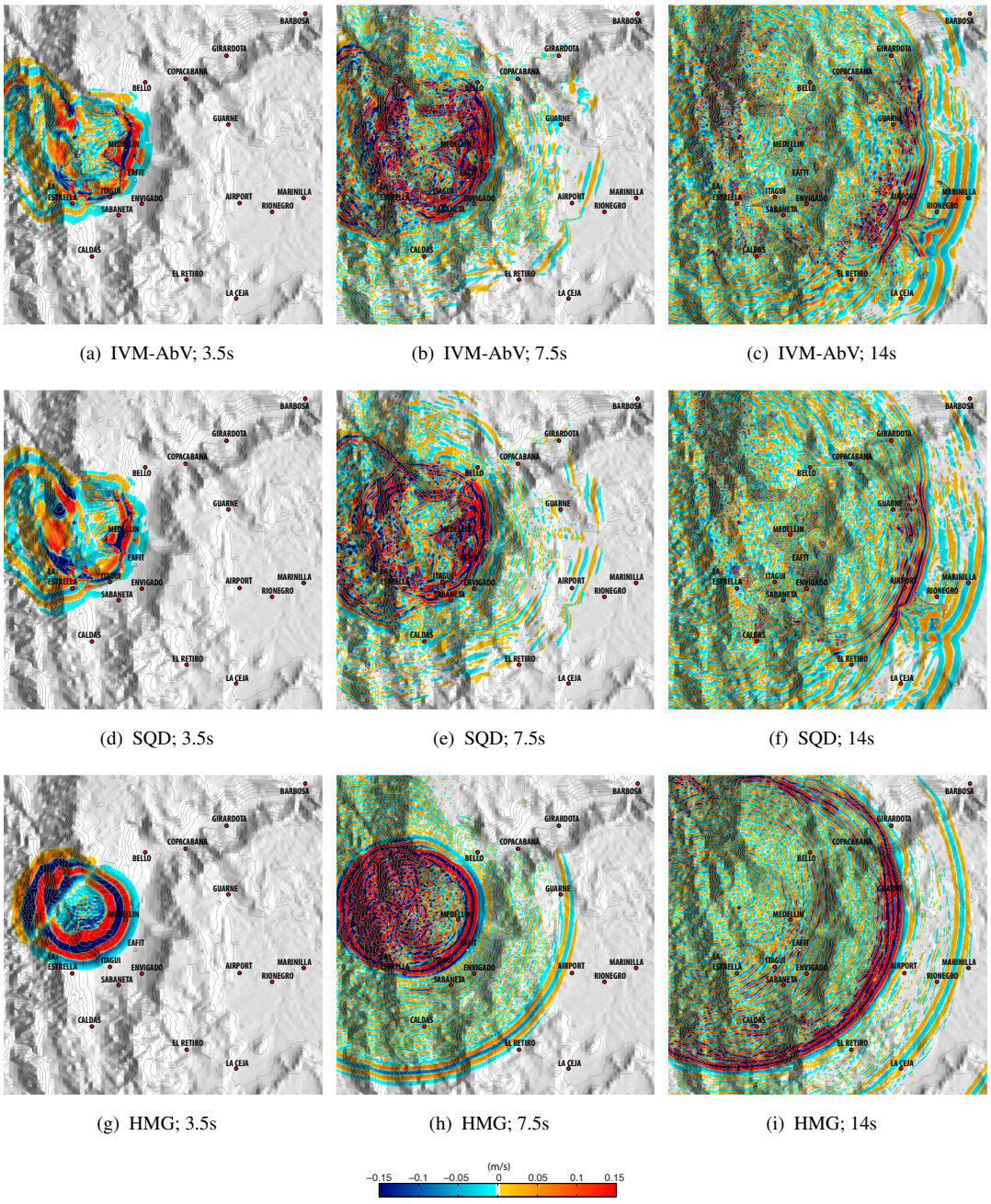

(a) IVM-AbV; 3.5s (b) IVM-AbV; 7.5s (c) IVM-AbV; 14s

(d) SQD; 3.5s (e) SQD; 7.5s (f) SQD; 14s

(g) HMG; 3.5s (h) HMG; 7.5s (i) HMG; 14s

Figure 6.4: Snapshots of the vertical component of the velocity wave field for the IVM-AbV (Figs., 6.4(a), 6.4(b), 6.4(c)), SQD (Figs., 6.4(d), 6.4(e), 6.4(f)), and HMG (Figs., 6.4(g), 6.4(h), 6.4(i)) models. The blue star illustrates the epicenter of the 4^{th} rupture scenario.

measurements of ground motion at two different sites is the presence or absence of topographic features; all other factors remaining constant (Davis and West, 1973; Field and Jacob, 1995). In other words, the SRM implicitly assumes that at two different stations,

effects from the source, directivity, and the internal soil structure are similar. This is obviously not an acceptable assumption for the highly heterogeneous ABR and its near source earthquake scenarios. To overcome this problem some other authors have used results from flat-free simulations as the reference site (e.g., Bouchon and Barker, 1996; Lee et al., 2009a,b). From the numerical point of view this strategy is the natural step to follow since flat-free simulations are the standard scheme. In this work we will follow the same strategy and use the SQD results as the reference site. Specifically, we provide quantitative insight regarding the distribution of amplifications/reductions by topographic effects in terms of topographic amplification factors (TAF) computed as:

$$\mathrm{TAF} = \mathrm{PG}(\bullet)\ \mathrm{Amplification} = \frac{(\mathrm{PG}(\bullet)_{\mathrm{IVM-AbV}} - \mathrm{PG}(\bullet)_{\mathrm{SQD}})}{\mathrm{PG}(\bullet)_{\mathrm{SQD}}} \times 100\%, \qquad (6.1)$$

where $\mathrm{PG}(\bullet)_{\mathrm{IVM-AbV}}$, and $\mathrm{PG}(\bullet)_{\mathrm{SQD}}$ are peak ground velocities (PGV) from the IVM-AbV, and the SQD models respectively. The PGVs are computed as the absolute value of the three components of ground velocity. At some specific sections we also present graphical representations of TAF in terms of peak ground accelerations (PGA), although we favor the representation in terms of ground velocity because it is closely related with the kinetic energy of the system.

Figures 6.5, and 6.6 present the peak ground velocity (PGV) distribution for the IVM-AbV, and the SQD simulations. These results show the largest values shifted north from the epicenter and located somewhere between the Caldas and the Sabaneta municipalities. The shifting, spatial distribution, and PGV values are quite similar (Figs. 6.5(a); 6.5(b)). This resemblance indicates that topography contributes only moderately to the PGVs of the zone close to the epicenter of the first source scenario. The large amplitude values are likely source effects related to the proximity to the rupture zone. On the other hand, focusing effects due to the substantial variations in the 3D structure might have been the reason for

the shifting from the epicenter. More significant modifications arise at the elevated regions NE from the epicenter. Here, at the SNV near the airport, the PGV is distributed in a more scattered fashion as a consequence of the topographic irregularities. For the same region, the PGV distribution in the absence of topography is smother, and does not exhibit saturated areas of maxima Fig. 6.5(b). PGV reductions due to topography are also visible. An example of *shielding* effects from the ABR topography are seen east the epicenter up to the El Retiro municipality. For this source scenario, it appears that the proximity of the epicenter to the foot of the surficial irregularity creates a zone of destructive interference along the slopes of the local topography.

The shielding effect between the epicenter of the first event and the El Retiro municipality is now more evident from the dark blue colors exhibited by the TAF in Fig. 6.5(c). Even more, it is now clear that such a shielding effect spreads NE along the top of the eastern flank of the Aburrá Valley depression. Other zones of de-amplification previously hidden by the scale of the PGV schematics become clear. Among those, the relatively flat area of the mountains behind the Bello, and Copacabana locations exhibit TAF of less than 100 percent. On the other hand, the complex geometry of the ABR clearly generates the amplification patterns seen all over the SNV. Regarding the metropolitan area of the Aburrá Valley, there is a mixed response depending on the position, though trending towards amplification.

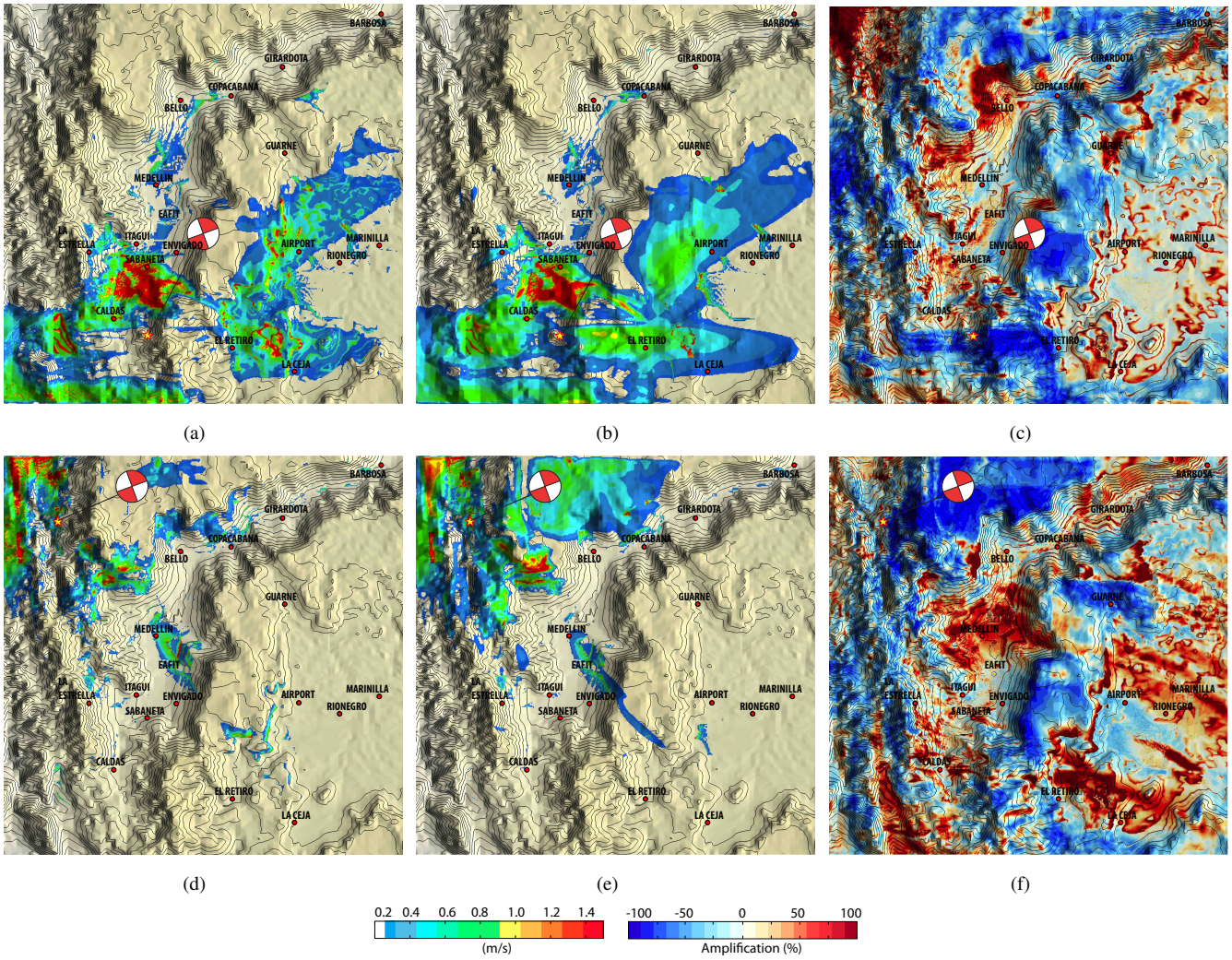

Figure 6.5: PGV maps for events 1, and 2. The 1^{st}, and 2^{nd} cols illustrate the results from the IVM-AbV, and the SQD models. The 3^{rd} col depicts TAF according to eqn. (6.1). Warmer/Cooler colors indicate amplification/reductions by the ABR topography.

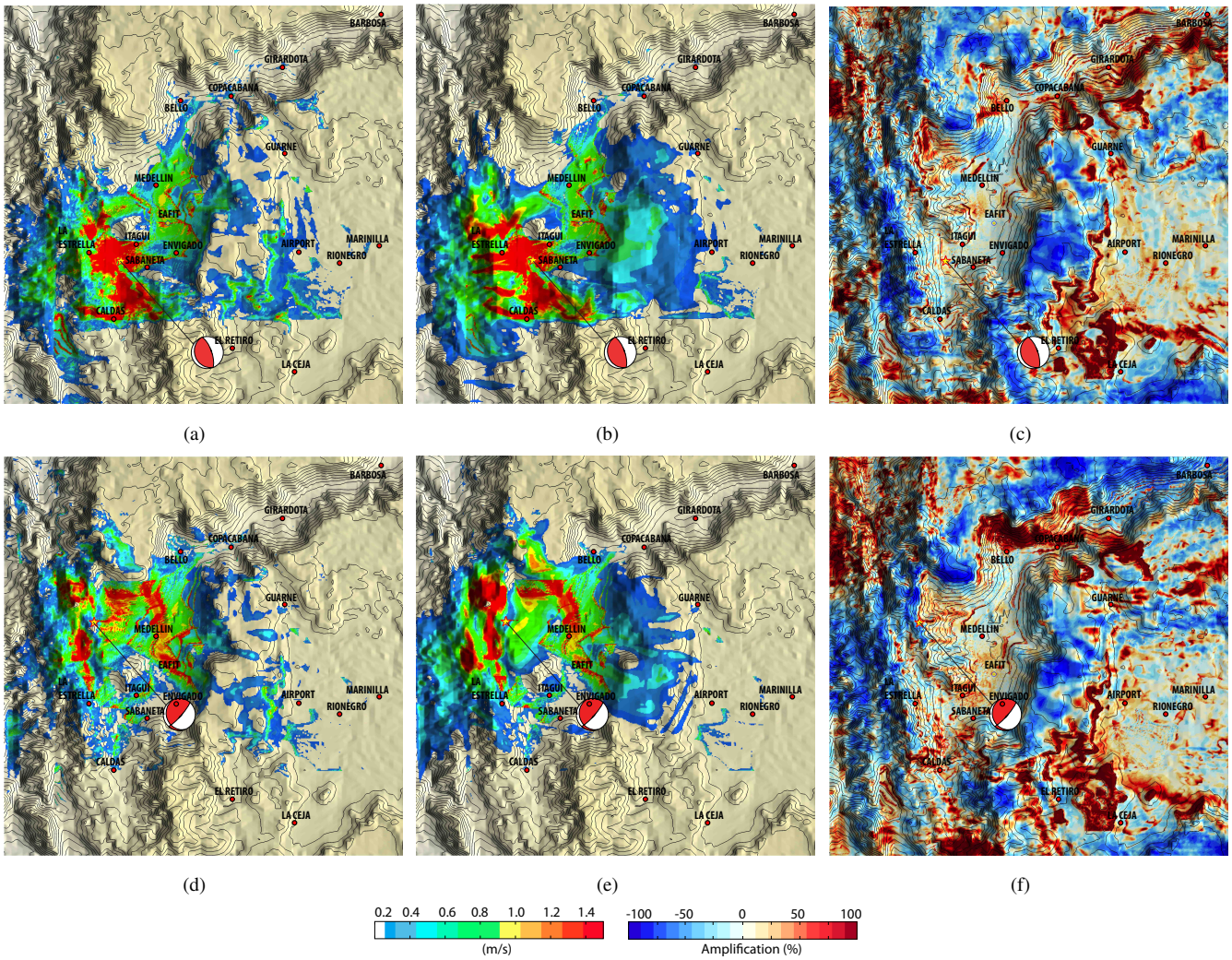

Figure 6.6: PGV maps for events 3, and 4. The 1^{st}, and 2^{nd} cols illustrate the results from the IVM-AbV, and the SQD models. The 3^{rd} col depicts TAF according to eqn. (6.1). Warmer/Cooler colors indicate amplification/reductions by the ABR topography.

Of particular note is the amplification at the slopes of the mountain that partially surrounds the Bello community. As the contour lines suggest, the local topography consists of particularly steep slopes. In addition, the Bello area is located along a straight line directly from the epicenter of the first event (see Fig. 6.1(h)); therefore, seismic energy is directly radiated towards it. Such a combination of effects might be the reason for the strong pattern of local amplification.

The PGV distribution for the second rupture scenario focuses most of its larger values near the epicenter as in the first scenario (see second row of Fig. 6.5), although in a relatively smaller area. This is basically the case of the IVM-AbV results where wavefield interactions with the ABR topography dissipate most of the seismic energy; see Fig. 6.5(d). The similarities with the first source scenario regarding the impact of strike-slip earthquakes near the foot of local topographic variations are particularly noteworthy. As readily seen from Fig. 6.5(d), the slopes, and the top of the mountain just to the east of the epicenter present considerable reductions in their PGVs with respect to the model without topography Fig. 6.5(e). Again, the shielding effect is evident from Fig. 6.5(f). Notice that for this rupture scenario, the steep slopes around the Bello municipality exhibit major reductions as consequence of the shielding effect. Zones of amplification due to the combined effect of local topography and source radiation are now observed at the re-entrant corner found midway between Medellín city and the Airport. This particular geologic feature is locally known as the river bed of the Santa Elena stream, one of the major tributaries of the Medellín river.

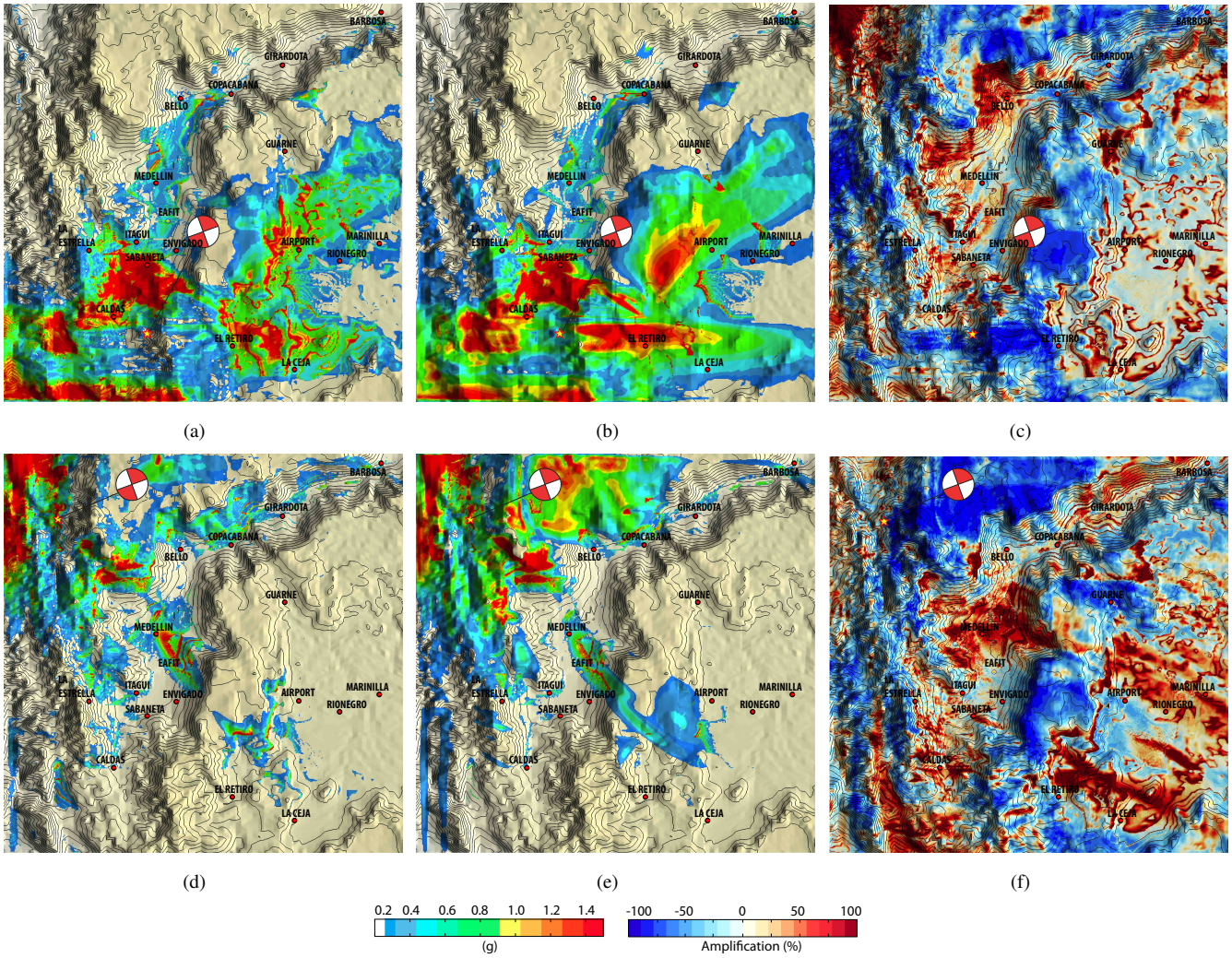

Figure 6.7: PGA maps for events 1, and 2. The 1^{st}, and 2^{nd} cols illustrate the results from the IVM-AbV, and the SQD models. The 3^{rd} col depicts TAF according to eqn. (6.1). Warmer/Cooler colors indicate amplification/reductions by the ABR topography.

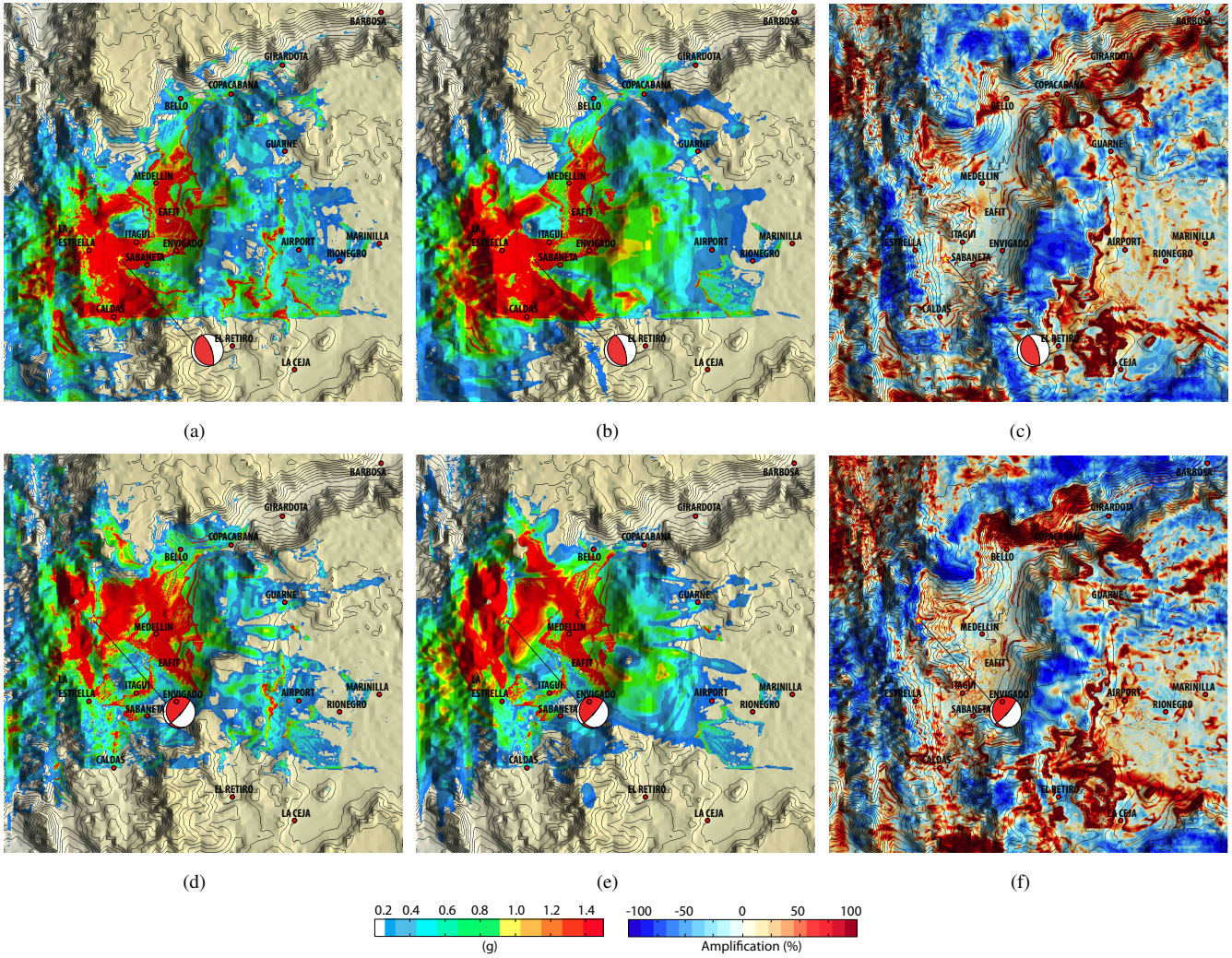

Figure 6.8: PGA maps for events 3, and 4. The 1^{st}, and 2^{nd} cols illustrate the results from the IVM-AbV, and the SQD models. The 3^{rd} col depicts TAF according to eqn. (6.1). Warmer/Cooler colors indicate amplification/reductions by the ABR topography.

Because the third and fourth earthquake scenarios are closer to the center of the domain their PGV spatial distributions exhibit larger spreading and greater effects from basin interactions than the strike-slip scenarios Fig. 6.6. Evidence of the latter can be found in the relatively low PGV amplification factors exhibited along the Quaternary deposits of the metropolitan area of the ABR (see Figs. 6.6(c), and 6.6(c)). Evidence of major topographic effects, however, appears again as patterns of amplification throughout the SNV, and along the steep slopes of the mountain close to Bello, and Copacabana cities. As already mentioned, the shielding effect along the top of the eastern flank of the Aburrá Valley depression is also visible.

Regarding the ground motion accelerations, all the simulated earthquake scenarios produce the largest PGA in the neighbourhood of their epicenters (see Figs. 6.7, and 6.8). Both IVM-AbV, and SQD simulations exhibit this pattern. The PGA distribution however, is not uniform, and greatly depends upon the source location. The spreading pattern generally follows the same shape exhibited in the PGV maps, although covering a broader area. Again, effects from surficial irregularities generate more complex patterns of the PGA spatial distribution due to interactions of trapped energy with the undulating topography. In general, simulation results depict larger PGAs at the southern municipalities i.e., Caldas, Itagui, Envigado, Medellín, while the northern urban centers exhibit a more moderate seismic response. This is in agreement with seismic studies conducted for the ABR. Deterministic seismic hazard results for the Caldas municipality for instance, give to the Romeral fault a PGA = 0.78g for a distance to the rupture of 4.05 km. Conversely, no seismic hazard is associated with the Romeral fault for the Barbosa municipality (GSM, 2006, pp 360).

Basin effects from the soil deposits become more evident in the PGA plots due to the stronger dependence of soft-soil deposits to accelerations. This takes even grater significance due to the shallow nature of the earthquake scenarios considered. This might explain

the large saturated areas of PGA >> 1.5g spread over a considerable portions of the Quaternary deposits along the Aburrá Valley metropolitan area seen in Figs. 6.7, and 6.8. Similarly, in the SNV region, some saturated areas of PGA are also visible although of a lesser amount.

The strong similarities between the TAF computed from the PGA with those obtained from the PGV estimates are particularly interesting. It is generally accepted that contributions from rupture directivity and radiation patterns dominate the low-frequency velocity waveforms (Wald et al., 1996). On the other hand, site effects associated with soil deposits tend to be affected by the higher frequencies. As a result, traditional site effects are usually more prominently displayed by histories of ground motion acceleration. If the TAFs as computed here are in effect independent of the response parameter used, this could bring important benefits for computing TAF effects from field studies. Further analyses regarding this alleged invariance are, however, needed.

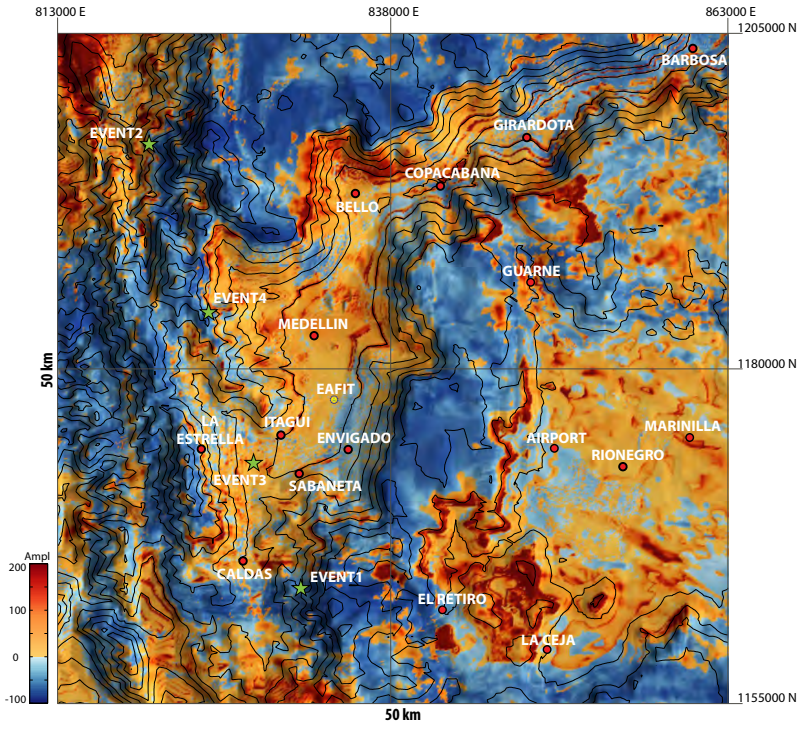

Figure 6.9: Envelopes of topographic amplification factors (TAF).

.

Figure 6.9 consolidates the TAF so far presented. The envelope shows the maximum value (preserving the sign) among results from Figs. 6.5(c); 6.5(f); 6.6(c); and 6.6(f). At least three different areas exhibiting noticeable amplification are identified by the envelope response. The first is the zone close to the top left-hand corner of the domain ($\approx$ 1200 m.a.s.l) where amplifications due to topographic effects reach values larger than 200 percent. The second occurs throughout the Aburrá Valley ($\approx$ 1500 m.a.s.l). This valley presents an average amplification between 100 and 150 percent, although areas of rapid differential motion are identified over its slopes. Some saturated areas are also visible. Detailed analyses carried out later on will reveal that some of these saturated zones can reach values up to 500 percent. Interestingly, the slope near Universidad EAFIT and Envigado city exhibits zones of amplification close to zero, i.e., simulations with, and without topography coincide. On the other hand, amplifications larger than 200 percent occur throughout the slopes of the mountain around the Bello municipality. The third amplification area is the San Nicolas Valley ($\approx$ 2000 m.a.s.l). Here, generalized amplifications of around 150 percent are observed. Interestingly, there are also zones of deamplification within the domain. These are also clearly identifiable. For instance, the top of both flanks of the Aburrá Valley show deamplifications greater 100 percent at both sides.

6.2 Local Response

Next, we examine more clearly the characteristics of the ground motion from the IVM-AbV, and the SQD simulations by analyzing synthetics of the ground velocity from: i) three west-east vertical sections, and ii) selected receivers throughout the region. Results from the fourth source model are used for the sections analyses, while those from the first rupture scenario are used for the analyses at the station level.

6.2.1 Synthetic Waveforms along Vertical Sections

Section 20N-20N located at lat: 1,175,000N (20 km north from the bottom of the domain). Figure 6.10 presents the 3D velocity structure of section for the IVM-AbV (top-left), and the SQD (top-right) models along with their corresponding synthetics of the free-surface vertical (Z) ground velocity. The geometric changes associated with the SQD model become now evident. Every geologic interface experiences a geometric modification, the extent of which increases with the topographic gradient of the geologic structure. Regarding the IVM-AbV, this reasonably detects the geologic structures along the section. The two Quaternary deposit (gray zones) at the Aburrá, and the San Nicolas valleys, are seen clearly.

Both cuts of synthetics exhibit in general a similar behavior during the initial stages of the wave motion. As noted in the analyses of snapshots, the first phases at $t < 5$s, which consist mostly of P-waves (and some already scattered wavefields as a result of 3D effects), are basically the same, and dominated by the response of the Quaternary deposits. Interaction between material interfaces begin also to emerge. The transmitted wave at the right-hand side corner of the Quaternary deposits of the Aburrá Valley (arrow a in Fig. 6.10) is an example of this. On the other hand, the second transmitted wave (arrow b), only appears in the IVM-AbV simulations, thus, is likely to be consequence of topographic effects.

The arrival of the S-waves is characterized by a very dramatic process of scattering and diffraction of seismic energy at distances between 10 and 20 km. These regions of focused amplification occur near the areas covered by soft-soil deposits in both models. Patterns of amplification due to topographic effects in these areas are also clearly seen. For instance, a cluster of seismic energy due to constructive interference is seen at $t \approx 17$s for distances close to 12 km in the IVM-AbV model alone. Around 18 km, the IVM-AbV results exhibit a more convoluted process characterized by significant scattering. This could be explained in part as a consequence of the three geologic units that converge near 18 km. Interestingly,

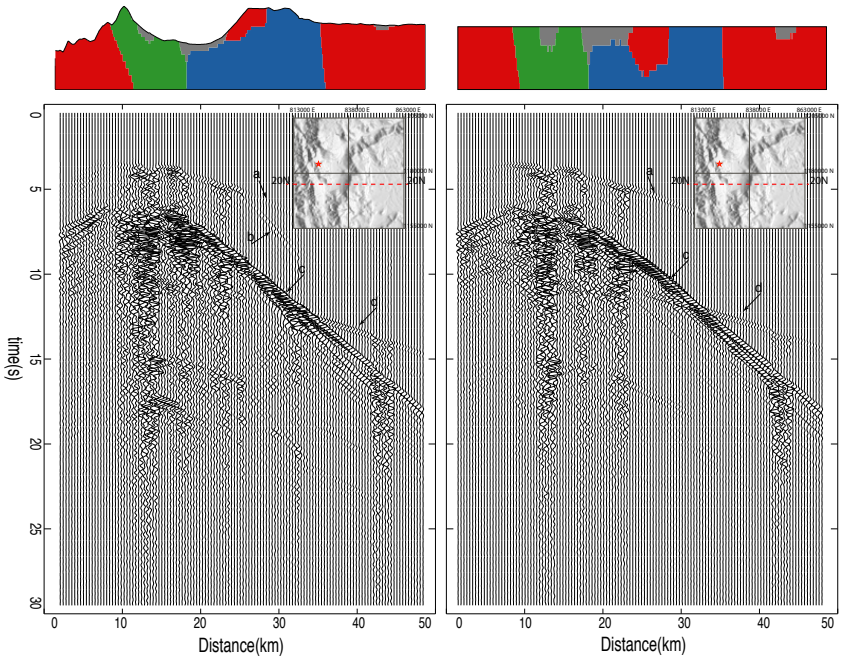

Figure 6.10: Section 20N-20N. The section is located 20km north from the bottom side of the domain (see snippet at the top for general location). The figure illustrates the 3D velocity structure and synthetics of the Z component of ground velocity due to the 4^{th} event, corresponding to the IVM-AbV (top-left; bottom-left), and the SQD (top-right; bottom right) models.

at this same location, is visible the generation of a very strong scattered wave travelling east (arrow c in Fig. 6.10). Source directivity and focusing effects from changes in the 3D velocity structure are the most likely reasons for the observed scattered wave.

The input of seismic energy in the San Nicolas valley region is largely controlled by S-phases associated with source directivity, and further scattered by focusing effects at the Aburrá Valley (arrow c Fig. 6.10). Noticeable changes due to topographic effects take place in these wavefields before they reach the elevated eastern region. The eastern flank of the mountain causes the amplitudes of the wavefields to increase. These attain their maxima close to the foot of the local topography feature at around a distance of 32 km. In addition, the wavefieds exhibit larger dispersion than those from the SQD simulation, which in turn modifies their patterns of constructive/destructive interference. Surprisingly, after crossing the geologic interface at 35 km, the wavefield exhibits a considerable amplitude reduction.

Consequently, the overall effect of this wave over the Quaternary deposits of the SNV is smaller than the effects of the analogous wave from the SQD simulation. Both models show a modest phase (arrow d) at the interface of the geologic units at 35 km. The effect of this phase in the Quaternary deposits of the SNV on the other hand, appears to be larger for the IVM-AbV simulations.

Figure 6.11 illustrates the section 30N-30N, located at lat:1,185,000N (30 km north from the bottom of the domain), and according to Table 5.1 it almost coincides with the local latitude of the fourth source model. Section 30N-30N exhibits a similar behavior as the previous cross-section. Here, the combination of source directivity and basin effects from the Quaternary deposits of the Aburrá Valley are again responsible of the dominant seismic wave travelling east. A shielding effect however is created by the eastern topography, which scatters and diffracts most of the seismic energy at distances greater than 30 km. Consequently the eastern side region experiences lower amplitudes.

Basin effects are the dominant feature in the central region of the 30N-30N section. Since topography reflects back part of the seismic energy into the basin, the amplitudes and duration of shaking are visibly increased. Evidence of basin-topography interaction is seen also between $t = 15$s, and $t = 20$s. Here, a package of seismic energy entering transversely to the the section due to 3D effects is amplified to a greater extent for the IVM-AbV model than for the SQD simulation.

At the western side of the section IVM-AbV the results show again a clear distortion of the seismic waves associated with the irregular topography. Here, reverberations of the wavefields with the surficial irregularity create larger patterns of amplification, and an evident increase of seismic response.

Section 40N-40N shows a more complex 3D velocity structure as well as more pronounced topographic gradient (Fig. 6.12). The relatively flat terrain on the east are in great contrast with the highly irregular topographic features on the west. The central portion of the Aburrá

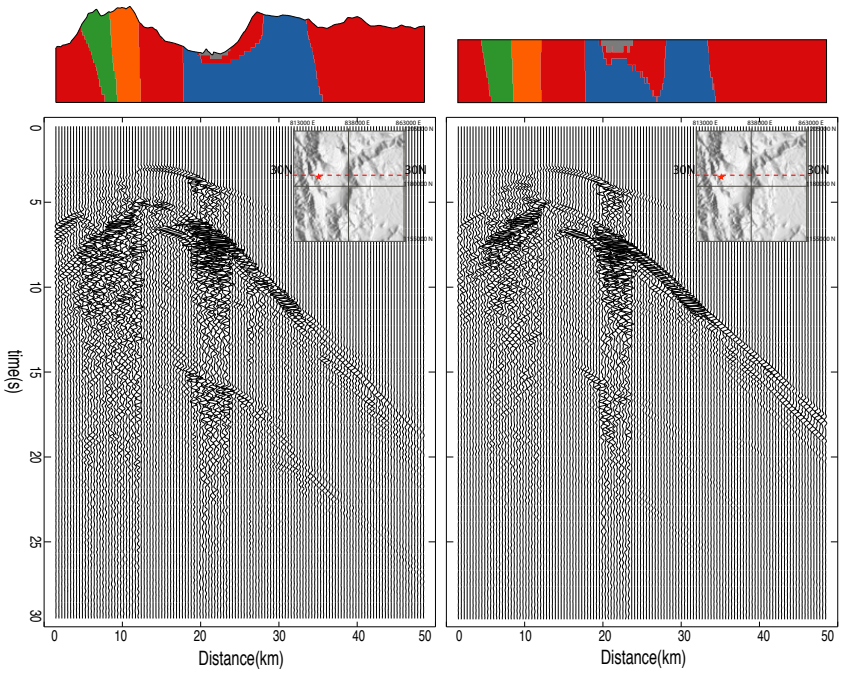

Figure 6.11: Section 30N-30N. The section is located 30km north from the bottom side of the domain (see snippet at the top for general location). The figure illustrates the 3D velocity structure and synthetics of the Z component of ground velocity due to the 4^{th} event, corresponding to the IVM-AbV (top-left; bottom-left), and the SQD (top-right; bottom right) models.

Valley also exhibits noticeable topographic features. Both simulations present an important reduction of the seismic response in the eastern part of the domain. This is expected as source radiation patterns decrease with distance. As expected, the larger share of seismic response intensifies in the smaller zones of Quaternary deposits and around the area near the epicenter of the fourth event. Interestingly, the concentration of seismic energy from the first arrival appears to be larger for the SQD model than for the IVM-AbV simulation. The subsequent scattering on the other hand, is more pronounced in the IVM-AbV simulation due to topographic effects.

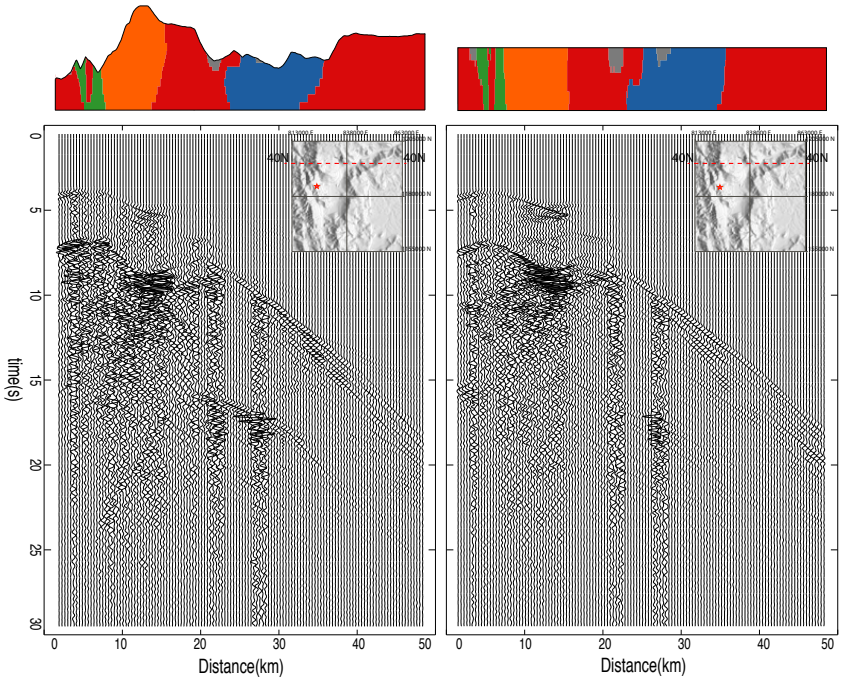

Figure 6.12: Section 40N-40N. The section is located 40km north from the bottom side of the domain (see snippet at the top for general location). The figure illustrates the 3D velocity structure and synthetics of the Z component of ground velocity due to the 4^{th} event, corresponding to the IVM-AbV (top-left; bottom-left), and the SQD (top-right; bottom right) models.

6.2.2 Topographic Amplification Factors on Vertical Sections

Figure 6.13 presents the TAF exhibited at the free-surfaces of 20N-20N; 30N-30N; and 40N-40N respectively. The computed TAFs are however slightly different in the sense that they are computed independently for each one of the three components of the synthetics of ground velocity. Moreover, Fig. 6.13 includes also the effects from the whole set of source scenarios. This throws additional light into the impact of topographic variations on the free-surface ground motion.

The topographic irregularities generate positive TAF values (amplification) of up to 500 percent at some specific locations. Reductions, although also present, always remain within the 0 to 100 percent range, and more frequently closer to zero. The specific patterns of topographic amplification depend strongly on the particular component of ground motion,

and greatly correlate with soft-sedimentary deposits, source-radiation effects, and material interface effects.

Section 20N-20N for instance exhibits a concentration of local maxima at its eastern side. This could be related with source directivity effects; see Fig. 6.13(a). The TAF for each

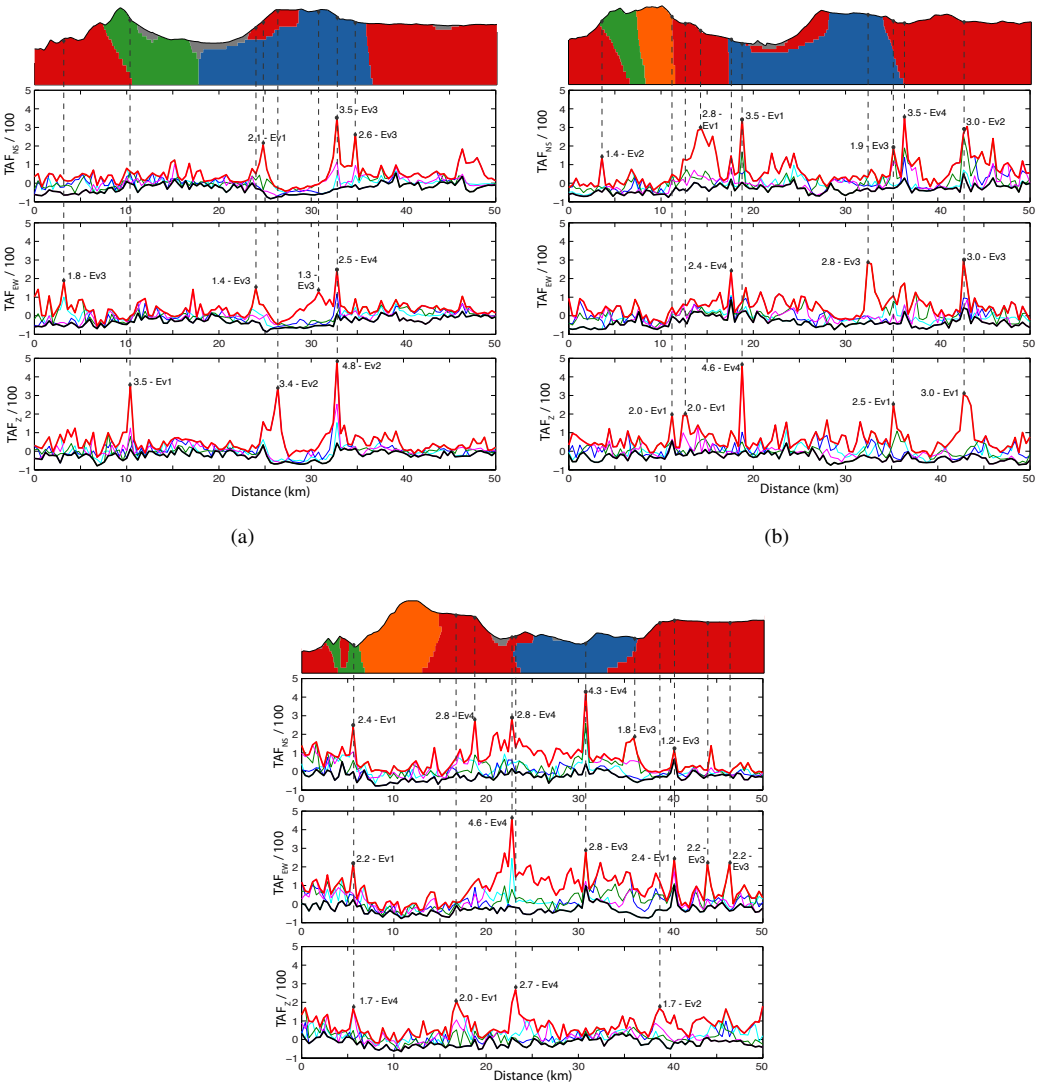

(a) (b)

(c)

Figure 6.13: TAF for sections: 20N-20N (6.13(a)); 30N-30N (6.13(b)); and 40N-40N (6.13(c)). The TAF are computed independently for the three components of the the ground velocity vector. Thick red and black lines represent the upper and lower bounds from all events. Cyan lines depict the TAF from the 1^{st} source scenario. The blue, green, and magenta lines depict the TAF results from the 2^{nd}, 3^{rd}, and 4^{th} rupture models.

velocity component is clearly correlated with topography. Maxima at the same location however, are triggered by different seismic sources. Moreover, some components of ground motion are more sensitive to topographic amplification than others. An example of this is the site around 10 km in section 20N-20N. Here, the first earthquake event yields a vertical amplification of 350 percent, while the EW, and NS components exhibit only a minor topographic effect.

Section 30N-30N shows a larger number of local maxima over the western mountain of the Aburrá Valley depression. Specifically, these local amplifications occur along the right slopes of the western mountain. Curiously, the top of the western mountain does not exhibit a significant topographic amplification. Our results challenge the traditional idea that topographic effects always are stronger at the top of the mountains. The first rupture scenario emerges as the major contributor of topographic amplification for the vertical component of the ground velocity vector, although the largest amplification, near 500 percent, is generated by the fourth source model. On the other hand, the third, and fourth source models contribute to the largest TAF in the EW velocity component. The NS velocity component does not show a particular preference for any of the four rupture scenarios.

Section 40N-40N presents substantial amplifications in the three components of ground velocity. All of them generated by the fourth rupture scenario. The NS velocity component shows a TAF of 430 percent at the foot hill of a local topographic feature located 30 km east of the left side of the domain. The EW, and Z components on the other hand, exhibit their maxima halfway up the slope around 23km east, with TAF of 460 and 270 percent respectively Fig. 6.13(c).

6.3 Synthetic Time Histories at RAVA and RAM Stations

To examine the effects of topography at a local scale we analyze synthetics of ground velocity at selected receivers throughout the Aburrá Valley metropolitan area. We choose the locations of the observation points to coincide with the stations of the strong ground motion network of the region. The position of the stations of the Strong Motion Accelerograph Network of the city of Medellín (RAM) consisting of 22 stations, and the Strong Motion Accelerograph Network of the Aburrá Valley (RAVA), consisting of 6 stations are shown in Fig. 6.14.

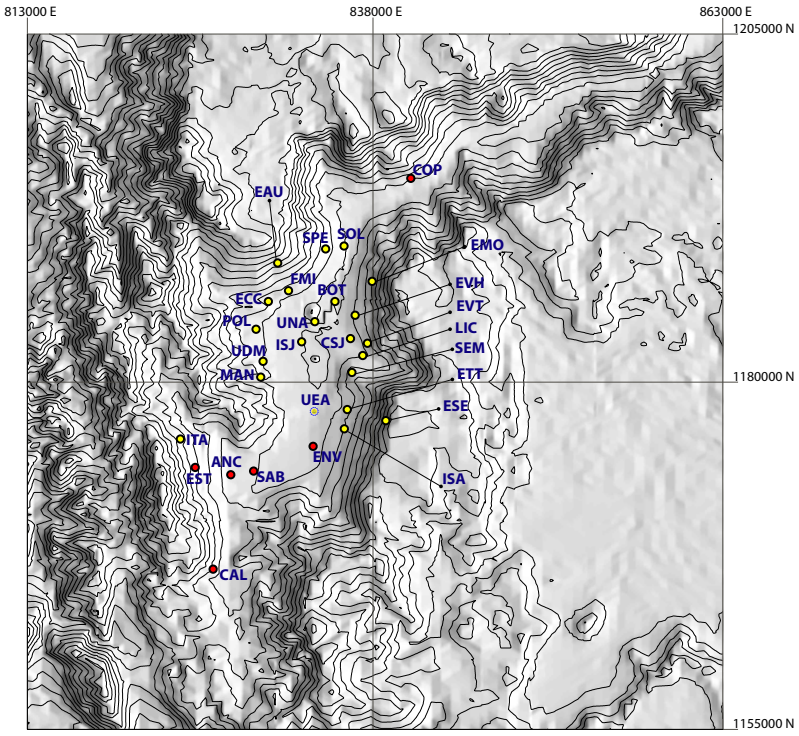

Figure 6.14: Stations of the strong motion accelerograph network of the city of Medellín (RAM) consisting of 22 stations (yellow dots), and the strong motion accelerograph network of the Aburrá Valley (RAVA) consisting of 6 stations (red dots).

6.3.1 Time Synthetics

Figures 6.15 shows the time histories of ground velocity from the first earthquake scenario at the locations of five of ABR seismic stations (Synthetic histories for the whole set of stations are provided in Appendix A). Synthetic records in the frequency domain for the parallel to fault (V_{PL}), and the normal to fault (V_N) components of the velocity vector are also provided on the last two rightmost columns. We benchmark again the results from the IVM-AbV simulation with those from the SQD model.

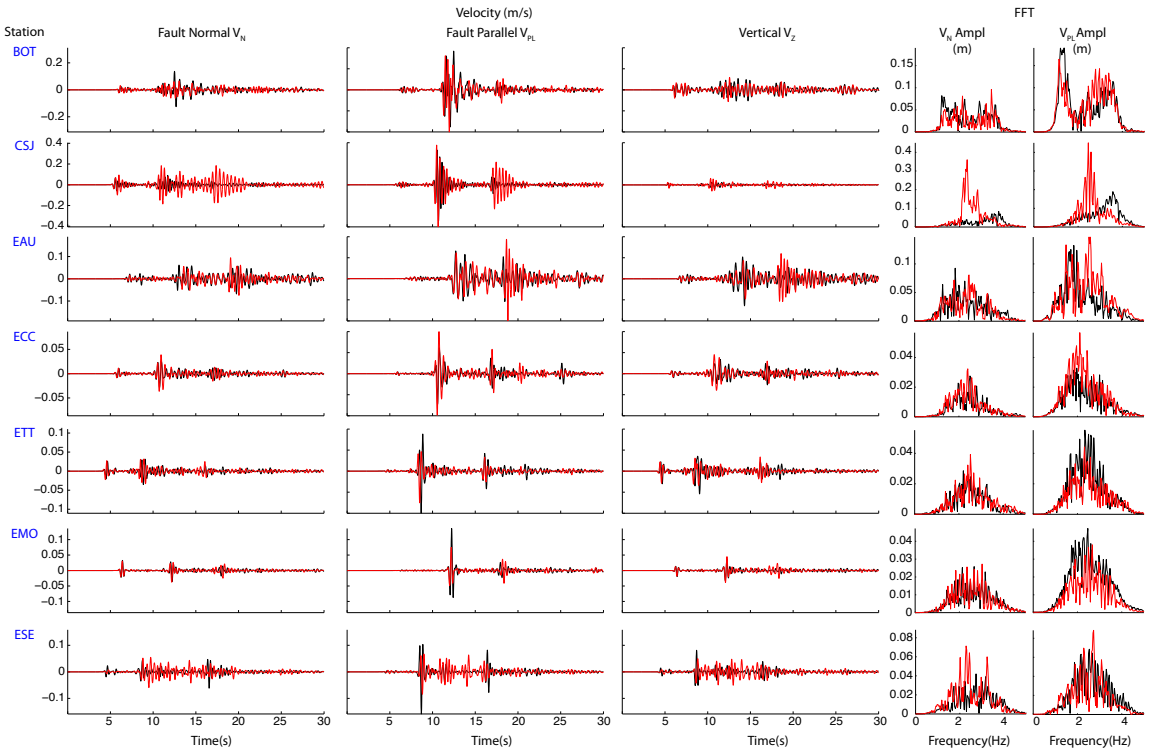

Figure 6.15: Synthetic time histories at five stations of the strong ground motion network of the ABR from earthquake scenario No 1. Red lines depict results from the IVM-AbV simulation. Black lines illustrate SQD results.

In all cases the fault-parallel component from both models exhibits the larger amplitudes as a consequence of the strike-slip nature of the first earthquake source. Additionally, the Z component exhibits amplitudes of the same order of magnitude as the fault normal component. This indicates near source effects. As expected, the first arrivals almost coincide in

the two models, although with slightly different travel-times. Late phases on the other hand present noticeable differences. At station CSJ, the presence of strong late arrivals of large amplitude due to topographic effects are evident in both the fault normal and fault parallel velocity components. Similar topographic effects in the form of strong late phases are displayed by two stations: 1) station EAU; which is located halfway up to the NW plateau of the Aburrá Valley; 2) ESE station located right at the top of the slope behind Universidad EAFIT and the Envigado municipality (see Fig. 6.14).

The Fourier spectra of the horizontal components further illustrate the topographic effects. IVM-AbV results for station CSJ exhibit a dramatic increase in its Fourier amplitude at around $f = 2.5$ Hz in both horizontal components. For the SQD results such an increment occurs shifted to the right at around $f = 3.8$ Hz, except that only for the fault parallel component. No other station shows this dramatic shifting in its fundamental frequency. Patterns of amplification/reduction such as those at the fault parallel components of the ETT, and EMO stations are noticeable. Another interesting phenomenon is exhibited by the Fourier amplitude spectra of the BOT station. Two dominant frequencies $f \approx 1$Hz, and $f \approx 3$Hz are identified by both models for the fault parallel component. Interestingly, the near zero amplification is close to $f = 2$ Hz i.e., the central frequency of the Ricker's pulse. Notice the alternating pattern of amplification. At $f \approx 1$Hz, the SQD results show the maximum Fourier amplitude, while at $f \approx 3$Hz the IVM-AbV simulation predicts the larger response. A direct explanation of such a peculiar behavior is not clear. Further analyses are the needed to explore potential causes.

6.3.2 Topographic Amplification Factors at RAVA-RAM Stations

Here we focus again on providing additional quantitative evidence of topographic amplification in terms of TAF. As in the analyses of vertical sections, we compute disaggregated TAF for each component of the ground velocity vector. The whole set of 28 observations

points representing the RAM, and RAVA stations as well as the four rupture scenarios are used 6.16.

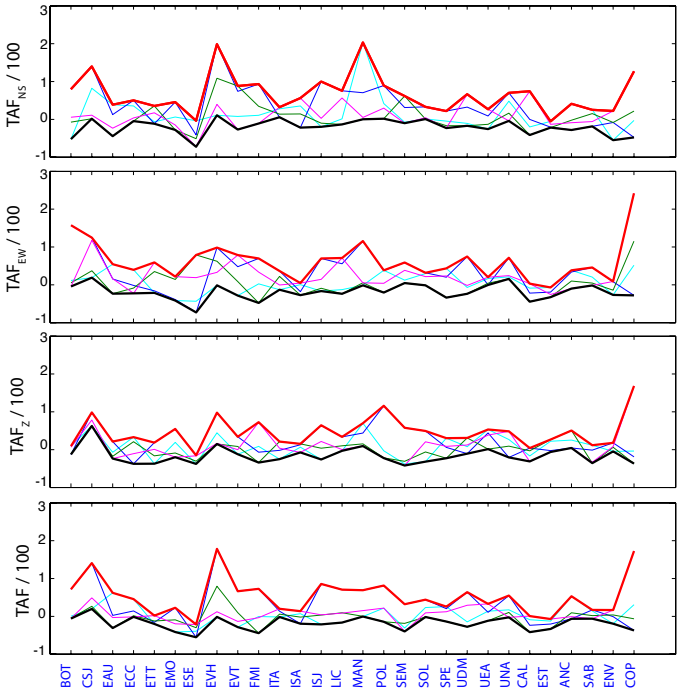

Figure 6.16: Topographic amplification factors at receivers coinciding with the RAM, and RAVA seismic networks. In descending order the figures illustrate the TAF for the NS, WE, Z, and full amplitude of the ground velocity vector. The cyan, blue, green, an magenta lines depict the results associated with the $1^{\text{st}}, 2^{\text{nd}}, 3^{\text{rd}}, 4^{\text{th}}$ rupture models. The solid red, and black lines depict the upper and lower bounds of the respective figure.

Amplifications take values in the zero to two range, while de-amplifications stay in the zero to one range. The same pattern of reduction was established when analyzing the vertical sections. In contrast with our previous findings, it appears that obtaining TAF from only 28 stations tends to underpredict the impact of topography according to our metrics. To further examine these results, Fig. 6.17 compares the spatial distribution of TAF from the RAM-RAVA stations results, with those presented in Fig. 6.9(a). The latter is based on a 100 m grid resolution. In order to determine the combined geometric coverage of RAM, and RAVA, we projected the stations locations onto a 2D triangular mesh, and then linearly interpolated the nodal values Fig. 6.17(a). Figure 6.17(b) presents the results from the highly oversampled synthetic grid in which the projected coverage area is highlighted for

comparison purposes. The contrast between results is evident. As intuitively expected, the undersampling of the RAM-RAVA networks clearly result in a poor representation of the spatial distribution of TAF throughout the Aburrá Valley. The larger differences appear near the CAL station. Figure 6.17(a) predicts an almost constant reduction pattern along the path from station CAL to ESE. Although zones of reduction at the slopes near Universidad EAFIT are also visible, a more complex spatial pattern of amplification/reductions is shown by the finer mesh results. Similar inaccuracies are exhibited NW of the CAL station towards the ITA and EST stations. The source of these discrepancies is understood immediately. Since stations such as CAL and COP are the most isolated of the entire network, their values, whatever they are, will control the response of their neighbouring area even at those locations that exhibit large spatial variations.

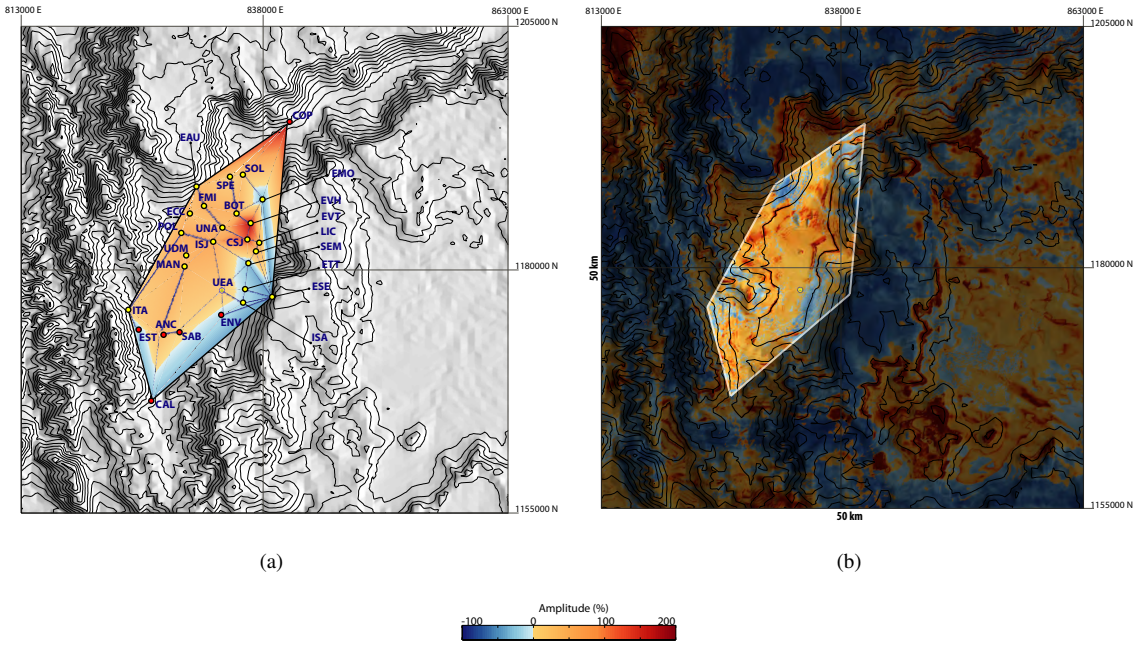

Figure 6.17: TAF maps from 28 synthetic observation points representing the RAM and RAVA strong ground motion stations (Fig. 6.17(a)) vs., TAF results from a 100 m grid resolution (Fig. 6.17(b)). The combined geometric coverage of RAM and RAVA was obtained by projecting the stations locations onto a 2D triangular mesh. Results at the vertices were further interpolated to obtain the TAF spatial variation. Figure 6.17(b) was obtained by illuminating the coverage area of RAM and RAVA from Fig. 6.9

.

Even when these remarks are based upon idealized earthquake scenarios, and no validation with real data is yet available, they highlight the importance of topography-related site effects, and the significant variations in ground motion created at very small distances. Moreover, comparisons such as those presented in Fig. 6.17 could be used as important tools for designing and/or improving existent strong ground motion networks developed initially toward the detection of site-effects due to soil amplification.

Chapter 7

Concluding Remarks

This dissertation set out to fulfill two specific goals. First, to present a numerical scheme based upon a finite element framework for the numerical modeling of earthquake-induced ground motion in the presence of realistic topographical variations of the Earth's crust. Second, to conduct a comprehensive set of deterministic 3D ground motion numerical simulations in an earthquake-prone region that exhibits moderate-to-strong surficial irregularities known as the Aburrá Valley in the department (state) of Antioquia - Colombia.

The first goal was accomplished by adopting ideas widely used in micro-, and fracture-mechanics into the realm of elastodynamics. Specifically, we proposed to follow a non-conforming meshing scheme for the numerical representation of the surficial irregularity. This allowed us to obviate the treatment of strong localized geometrical variations very likely to occur in realistic topographic settings. As a result, peaks, troughs, and re-entrant corners of the targeted relief, which under traditional conforming schemes would demand the use of special mesh refinements in order to avoid negative Jacobians or ill-conditioned finite elements, are easily managed with our technique. In particular, we proposed a two-step numerical scheme. In the first step the targeted topography is accommodated by a unstructured octree mesh. This allowed us to use the attractive features of the multiresolution cubic finite elements. In the second step, we subdivide the outer cubic elements into

five linear tetrahedral elements. The stiffness matrix of each tetrahedron is further scaled according to the topographic volume occupied by the element. The stiffness matrix of the parent cubic finite element is generated by conventional matrix assemblage. Stiffness scalability for the exterior topographic elements is the most salient feature of the method. Scalability holds, as one needs to compute only five generic stiffness matrices at the beginning of the simulation. Consequently, we showed that the computational advantages of octree-based finite element method are preserved even in the presence of surficial topography. We tested the benefits of this strategy (called Virtual Topography VT) by benchmarking its results against those from two reference examples. Our qualitative comparisons showed an excellent agreement between the various sets of results. Moreover, the close agreement was obtained using the same mesh refinement as in traditional flat-free simulations. We also showed that staircase meshes can also render acceptable results. However, such meshes require a refinement on the order of 50 points per wavelength. This is unacceptable for large-scale 3D ground motion simulations. Quantitative comparisons in the form of convergence analysis verified that the VT approach preserves the convergence of the L2-Norm. By contrast, stairlike meshes lead to a significant degradation of the convergence rate.

We accomplished our second goal after implementing the VT scheme into Hercules, the octree-based finite-element earthquake simulator developed by the Quake Group at Carnegie Mellon University. We developed a model of $50\times50\times25$ km^3, of the Aburrá Valley region, a moderate intra-mountain depression located at the northern end of the central range of the Colombian Andes. We conducted a series of simulations based upon four $M_{\mathrm{w}} = 5$ rupture scenarios along the segment of the Romeral fault. Our results confirmed the importance of surface topography on the synthetics of ground motion throughout the region. In particular, our findings for the Aburrá Valley region showed that:

- The interaction of surficial topography with near-source scenarios and heterogeneous

3D velocity structures creates extremely complex patterns of scattering and reflection of seismic energy. As the wavefields propagate through the valley, the interaction with the undulating topography generates a significant number of high-frequency surface waves that continue reverberating long after the passage of the main wavefronts, and consequently, increase the duration of shaking. This was clearly confirmed in the snapshots of the third earthquake model. Here, the characteristics of the rupture directed most of the seismic energy NE which after crossing the right flank of the Aburrá Valley left a dramatic trail of high amplitude surface waves.

- The impact of topography in the lower parts of the metropolitan area of the Aburrá Valley characterizes by a tendency toward ground motion amplification when compared with results that omit topography. The slopes of the valley act as barriers that bounce back part of the seismic energy into the valley generating zones of constructive/destructive interference. Moreover, it appears that substantial variations of the 3D velocity structure enhance this behavior. This was confirmed by the elevated Topographic Amplification Factors (TAF 500) that were found along the free surfaces of sections 30N-30N, and 40N-40N near strong lateral material interfaces.

- The slopes of the Aburrá Valley exhibit a contrasting distribution of amplifications/reductions that seems to correlate with source-directivity effects, the steepness of the slope, and local variations of the topographic relief. For instance, along the eastern slopes close to Universidad EAFIT, and the Envigado municipality, our results show spots of amplification, at the same time that the overall behavior is towards reductions. These reductions are minor and do not exceed 50 percent. By contrast, the slopes behind the Bello municipality, characterized by steep-slopes and a prominent re-entrant corner exhibit amplifications that exceed 200 percent. Similar patterns of amplification are exhibited at other re-entrant corners such as the riverbed of the Santa Elena tributary stream.

- The San Nicolas valley region is largely affected by topographic effects. Located at the eastern side of the domain the region exhibits TAF between 50 and 100 percent. Some reduction areas were found although to a lesser extent. For the San Nicolas valley, which is located on an elevated plateau, the overall amplification pattern exhibited is consistent with conclusion from other studies.

Our results underline the impact of topography-related site effects, and their importance in studying the characteristics of ground motion in metropolitan areas located in mountainous regions. For the specific case of the Aburrá Valley metropolitan area, the refinement of the velocity and source models would definitely help shed light into the characteristics of ground motion throughout the region. More detailed results based on improved velocity and source models could in the future drive the efforts for incorporating topographic amplification factors into local seismic standards. In addition, results from studies such as the present one can be used to define appropriate locations for new strong ground motion seismic stations that would be aimed at providing realistic estimates of the spatial variability of earthquake ground motion, including estimates of the topography effects.

Appendix A

Synthetics of ground motion at the stations of the RAM and RAVA seismic networks. Earthquake source No:1

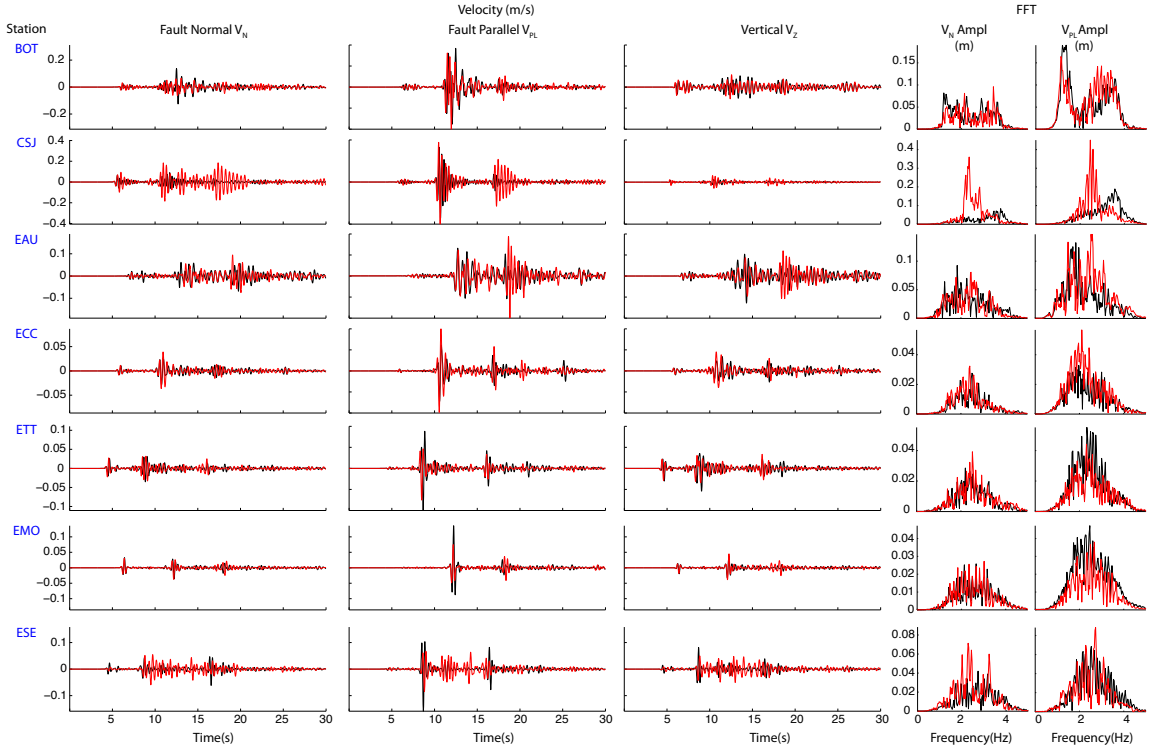

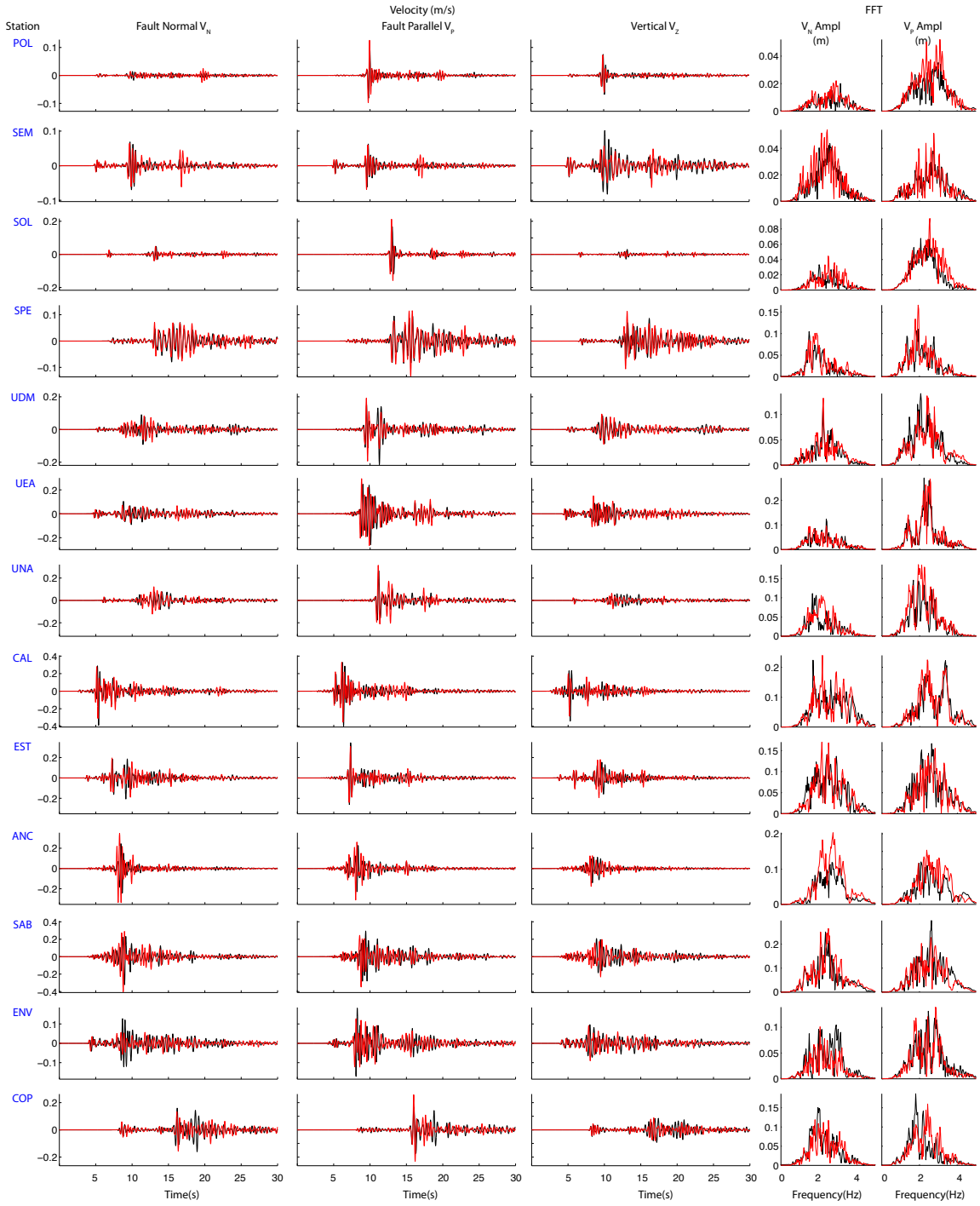
Velocity (m/s)
FFT
Station
Fault Normal V_N
Fault Parallel V_P
Vertical V_Z
V_N Ampl (m)
V_P Ampl (m)
POL
SEM
SOL
SPE
UDM
UEA
UNA
CAL
EST
ANC
SAB
ENV
COP
Time(s)
Time(s)
Time(s)
Frequency(Hz)
Frequency(Hz)

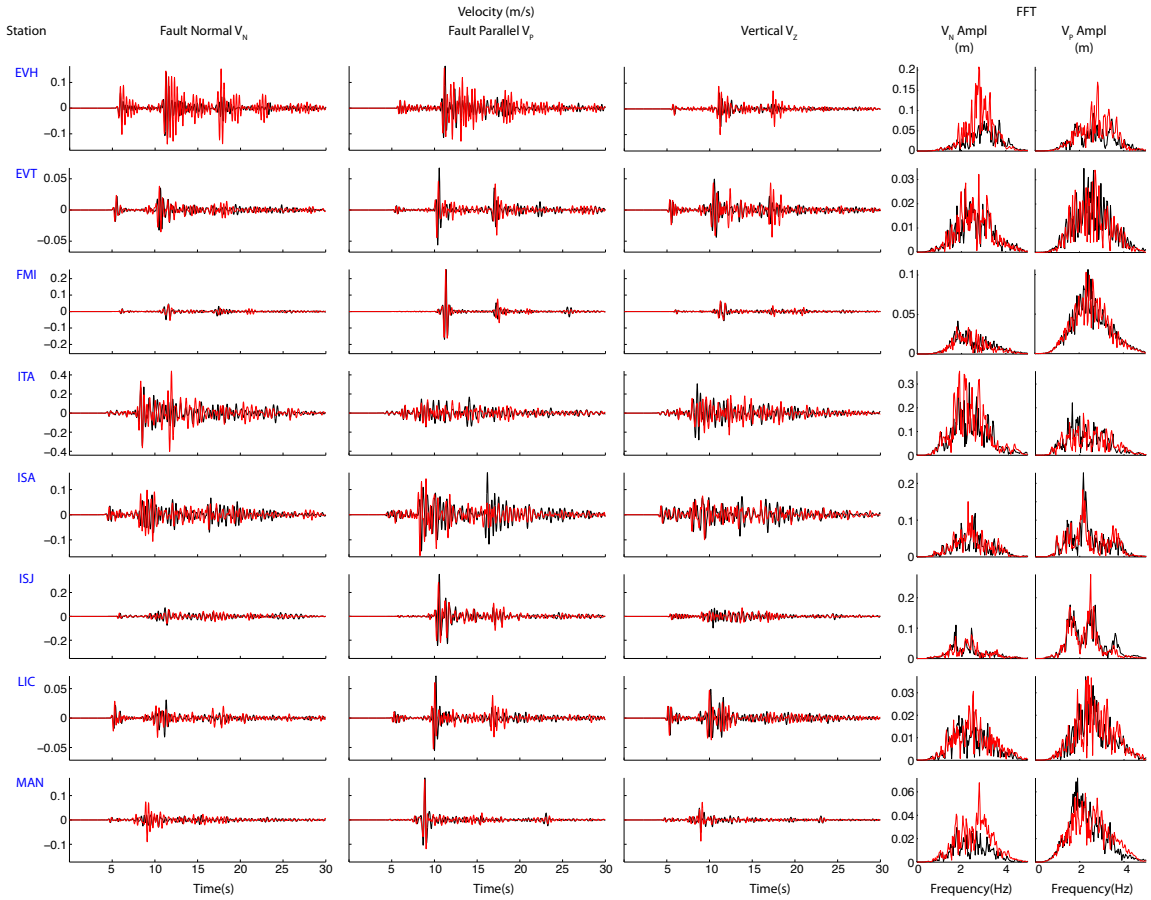

Figure A.1: Synthetic time histories at the twenty eight stations of the strong ground motion network of the ABR from earthquake scenario No 1. Red lines depict results from the IVM-AbV simulation. Black lines illustrate SQD results.

Bibliography

Aagaard, B., Brocher, T., Dolenc, D., Dreger, D., Graves, R., Harmsen, S., Hartzell, S., Larsen, S., and Zoback, M. (2008). Ground-motion modeling of the 1906 San Francisco earthquake, Part I: Validation using the 1989 Loma Prieta earthquakes. *Bulletin of the Seismological Society of America*, 98(2):989–1011.

Acevedo, A. (2011). Construcción de un modelo interpretativo 3D hasta 30km de profundidad de la corteza alrededor del Valle de Aburrá. Master's thesis, Universidad EAFIT.

Adams, B. M. and Jaramillo, J. D. (2002). A two-dimensional study on the weak-motion seismic response of the Aburra Valley, Medellín, Colombia. *Bulletin Of The New Zealand Society For Earthquake Engineering*, 35(1):17–41.

Aki, K. (1993). Local site effects on weak and strong ground motion. *Tectonophysics*, 218(1):93–111.

Aki, K. and Larner, K. L. (1970). Surface motion of a layered medium having an irregular interface due to incident plane SH waves. *Journal of Geophysical Research*, 75(5):933 – 954.

AlMuhaidib, A. M., Fehler, M. M., Toksöz, M. N., and Zhang, Y. M. (2011). Finite difference elastic wave modeling including surface topography. In *2011 SEG Annual Meeting*.

Aristizábal, E., Roser, B., and Yokota, S. (2005). Tropical chemical weathering of hillslope deposits and bedrock source in the Aburrá Valley, northern Colombian Andes. *Eng Geol*, 81(4):389 – 406.

Arvidsson, R., Boutet, J. T., and Kulhanek, O. (2002). Foreshocks and aftershocks of the M_w= 7.1, 1992, earthquake in the Atrato region, Colombia. *Journal of seismology*, 6(1):1–11.

Assimaki, D. and Gazetas, G. (2004). Soil and topographic amplification on canyon banks and the 1999 Athens earthquakes. *Journal of Earthquake Engineering*, 8(01):1–43.

Assimaki, D., Gazetas, G., and Kausel, E. (2005a). Effects of local soil conditions on the topographic aggravation of seismic motion: Parametric investigation and recorded field evidence from the 1999 Athens earthquakes. *Bulletin of the Seismological Society of America*, 95(3):1059–1089.

Assimaki, D., Kausel, E., and Gazetas, G. (2005b). Wave propagation and soil–structure interaction on a cliff crest during the 1999 Athens Earthquake. *Soil Dynamics and Earthquake Engineering*, 25(7):513–527.

Athanasopoulos, G., Pelekis, P., and Leonidou, E. (1999). Effects of surface topography on seismic ground response in the Egion (Greece) 15 June 1995 earthquakes. *Soil Dyn Earthq Eng*, 18(2):135 – 149.

Baher, S., Davis, P. M., and Fuis, G. (2002). Separation of site effects and structural focusing in Santa Monica, California: A study of high-frequency weak motions from earthquakes and blasts recorded during the Los Angeles region seismic experiment. *Bulletin of the Seismological Society of America*, 92(8):3134–3151.

Baher, S. A. and Davis, P. M. (2003). An application of seismic tomography to basin focusing of seismic waves and Northridge earthquake damage. *Journal of Geophysical Research, B: Solid Earth*, 108(B2).

Bao, H., Bielak, J., Ghattas, O., Kallivokas, L. F., O'Hallaron, D. R., Shewchuk, J. R., and Xu, J. (1996). Earthquake ground motion modeling on parallel computers. In *Supercomputing Conference*.

Bao, H., Bielak, J., Ghattas, O., Kallivokas, L. F., O'Hallaron, D. R., Shewchuk, J. R., and Xu, J. (1998). Large-scale simulation of elastic wave propagation in heterogeneous media on parallel computers. *Comput Method Appl M*, 152:85–102.

Bard, P.-Y. (1982). Diffracted waves and displacement field over two-dimensional elevated topographies. *Geophysical Journal of the Royal Astronomical Society*, 71(3):731–760.

Bard, P.-Y. (1997). Local effects on strong ground motion: Basic physical phenomena and estimation methods for microzoning studies. In *Proceedings of SERINA Seismic Risk: an Integrated Seismological, Geotechnical and Structural Approach, Thessaloniki, Greece, pp. 229299.*

Barrero, D., Pardo, A., Vargas, C., and Martínez, J. (2007). Colombian sedimentary basins: Nomenclature, boundaries and petroleum geology, a new proposal. *Agencia Nacional de Hidrocarburos*, pages 78–81.

Belytschko, T. and Black, T. (1999). Elastic crack growth in finite elements with minimal remeshing. *International Journal for Numerical Methods in Engineering*, 45(5):601–620.

Benowitz, B. A. and Waisman, H. (2013). A spline-based enrichment function for arbitrary inclusions in extended finite element method with applications to finite deformations. *International Journal for Numerical Methods in Engineering*.

Bielak, J., Ghattas, O., and Kim, E. J. (2005). Parallel octree-based finite element method for large-scale earthquake ground motion simulation. *Comput Model Eng Sci*, 10(2):99–112.

Bielak, J., Loukakis, K., Hisada, Y., and Yoshimura, C. (2003). Domain reduction method for three-dimensional earthquake modeling in localized regions, Part I: Theory. *Bulletin of the Seismological Society of America*, 93(2):817–824.

Bielak, J., Xu, J., and Gattas, O. (1999). Earthquake ground motion and structural response in alluvial valleys. *J Geotech Geoenviron*, 125:413–423.

Bohlen, T. and Saenger, E. H. (2006). Accuracy of heterogeneous staggered-grid finite-difference modeling of Rayleigh waves. *Geophysics*, 71(4):T109–T115.

Boore, D. (1973). The effect of simple topography on seismic waves: Implications for the accelerations recorded at Pacoima dam, San Fernando Valley, California. *Bulletin of the Seismological Society of America*, 63(5):1603–1609.

Boore, D. M. (1972). A note on the effect of simple topography on seismic SH waves. *Bulletin of the Seismological Society of America*, 62(1):275–284.

Borcherdt, R. (1970). Effects of local geology on ground motion near San Francisco Bay. *Bulletin of the Seismological Society of America*, 60(1):29–61.

Bouchon, M. (1973). Effect of topography on surface motion. *Bulletin of the Seismological Society of America*, 63(2):615–632.

Bouchon, M. and Barker, J. S. (1996). Seismic response of a hill: The example of Tarzana, California. *Bulletin of the Seismological Society of America*, 86(1A):66–72.

Bourgois, J., Calle, B., Tournon, J., and Toussaint, J.-F. (1982). The andean ophiolitic megastructures on the Buga-Buenaventura transverse (Western CordilleraValle Colombia). *Tectonophysics*, 82(3):207–229.

Bourgois, J., Toussaint, J.-F., Gonzalez, H., Azema, J., Calle, B., Desmet, A., Murcia, L. A., Acevedo, A. P., Parra, E., and Tournon, J. (1987). Geological history of the Cretaceous ophiolitic complexes of northwestern South America (Colombian Andes). *Tectonophysics*, 143(4):307–327.

Buech, F., Davies, T. R., and Pettinga, J. R. (2010). The Little Red Hill seismic experimental study: Topographic effects on ground motion at a bedrock-dominated mountain edifice. *Bulletin of the Seismological Society of America*, 100(5A):2219–2229.

Casarotti, E., Stupazzini, M., Lee, S. J., Komatitsch, D., Piersanti, A., and Tromp, J. (2008). CUBIT and seismic wave propagation based upon the spectral-element method: An advanced unstructured mesher for complex 3D geological media. In *Proceedings of the 16th International Meshing Roundtable*, pages 579–597. Springer.

Çelebi, M. (1987). Topographical and geological amplifications determined from strong-motion and aftershock records of the 3 March 1985 Chile earthquakes. *Bulletin of the Seismological Society of America*, 77(4):1147–1167.

Çelebi, M., Bazzurro, P., Chiaraluce, L., Clemente, P., Decanini, L., DeSortis, A., Ellsworth, W., Gorini, A., Kalkan, E., Marcucci, S., et al. (2010). Recorded motions of the 6 April 2009 M_w 6.3 L'Aquila, Italy, earthquake and implications for building structural damage: Overview. *Earthquake Spectra*, 26(3):651–684.

Chávez-García, F., Sánchez, L., and Hatzfeld, D. (1996). Topographic site effects and HVSR. A comparison between observations and theory. *Bulletin of the Seismological Society of America*, 86(5):1559–1573.

Colletta, B., Hebrard, F., Letouzey, J., Werner, P., and Rudkiewicz, J. (1990). Tectonic style and crustal structure of the Eastern Cordillera (Colombia) from a balanced cross-section. *Petroleum and tectonics in mobile belts: Paris, Editions Technip*, pages 81–100.

Cupillard, P., Delavaud, E., Burgos, G., Festa, G., Vilotte, J.-P., Capdeville, Y., and Montagner, J.-P. (2012). RegSEM: A versatile code based on the spectral element method to compute seismic wave propagation at the regional scale. *Geophysical Journal International*, 188(3):1203–1220.

DAMIAN (2010). *version 1.1*. Universidad EAFIT.

Daux, C., Mos, N., Dolbow, J., Sukumar, N., and Belytschko, T. (2000). Arbitrary branched and intersecting cracks with the extended finite element method. *International Journal for Numerical Methods in Engineering*, 48(12):1741–1760.

Davis, L. and West, L. (1973). Observed effects of topography on ground motion. *Bulletin of the Seismological Society of America*, 63(1):283–298.

Davis, P. M., Rubinstein, J. L., Liu, K. H., Gao, S. S., and Knopoff, L. (2000). Northridge earthquake damage caused by geologic focusing of seismic waves. *Science*, 289(5485):1746–1750.

Donati, S., Marra, F., and Rovelli, A. (2001). Damage and ground shaking in the town of Nocera Umbra during Umbria-Marche, central Italy, earthquakes: The special effect of a fault zone. *Bulletin of the Seismological Society of America*, 91(3):511–519.

Dréau, K., Chevaugeon, N., and Moës, N. (2010). Studied X-FEM enrichment to handle material interfaces with higher order finite element. *Computer Methods in Applied Mechanics and Engineering*, 199(29):1922–1936.

Dunant, C. F., Bary, B., Giorla, A. B., Péniguel, C., Sanahuja, J., Toulemonde, C., Tran, A.-B., Willot, F., and Yvonnet, J. (2013). A critical comparison of several numerical methods for computing effective properties of highly heterogeneous materials. *Advances in Engineering Software*, 58:1–12.

Faccioli, E., Maggio, F., Paolucci, R., and Quarteroni, A. (1997). 2D and 3D elastic wave propagation by a pseudo-spectral domain decomposition method. *Journal of Seismology,*, 1(3):237–251.

Field, E. and Jacob, K. (1995). A comparison and test of various site-response estimation techniques, including three that are not reference-site dependent. *Bulletin of the Seismological Society of America*, 85(4):1127–1143.

Field, E. H. (1996). Spectral amplification in a sediment-filled valley exhibiting clear basin-edge-induced waves. *Bulletin of the Seismological Society of America*, 86(4):991–1005.

Field, E. H., Johnson, P. A., Beresnev, I. A., and Zeng, Y. (1997). Nonlinear ground-motion amplification by sediments during the 1994 Northridge earthquake. *Nature*, 390(6660):599–602.

Field, E. H. and the SCEC Phase III Working Group (2000). Accounting for site effects in probabilistic seismic hazard analyses of Southern California: overview of the SCEC phase III report. *Bulletin of the Seismological Society of America*, 90(6B):S1–S31.

Frankel, A. (1993). Three-dimensional simulations of ground motions in the San Bernardino Valley, California, for hypothetical earthquakes on the San Andreas fault. *Bulletin of the Seismological Society of America*, 83(4):1020–1041.

Frankel, A. and Vidale, J. (1992). A three-dimensional simulation of seismic waves in the Santa Clara Valley, California, from a Loma Prieta aftershocks. *Bulletin of the Seismological Society of America*, 82(5):2045–2074.

Freymueller, J. T., Kellogg, J. N., and Vega, V. (1993). Plate motions in the North Andean region. *Journal of Geophysical Research, B: Solid Earth*, 98(B12):21853–21863.

Fries, T.-P. and Belytschko, T. (2010). The extended/generalized finite element method: An overview of the method and its applications. *International Journal for Numerical Methods in Engineering*, 84(3):253–304.

Gaffet, S. and Bouchon, M. (1989). Effects of two-dimensional topographies using the discrete wavenumber-boundary integral equation method in P–SV cases. *The Journal of the Acoustical Society of America*, 85:2277.

Gao, S., Liu, H., Davis, P., and Knopoff, L. (1996). Localized amplification of seismic waves and correlation with damage due to the Northridge earthquake: Evidence for focusing in Santa Monica. *Bulletin of the Seismological Society of America*, 86(1B):S209–S230.

Gazetas, G., Kallou, P., and Psarropoulos, P. (2002). Topography and soil effects in the M_s 5.9 Parnitha (Athens) earthquake: The case of Adámes. *Natural Hazards*, 27(1-2):133–169.

Geli, L., Bard, P.-Y., and Jullien, B. (1988). The effect of topography on earthquake ground motion: A review and new results. *Bulletin of the Seismological Society of America*, 78(1):42–63.

Gilbert, F. and Knopoff, L. (1960). Seismic scattering from topographic irregularities. *Journal of Geophysical Research*, 65(10):3437–3444.

Goto, H. and Bielak, J. (2008). Galerkin boundary integral equation method for spontaneous rupture propagation problems: SH-case. *Geophysical Journal International*, 172(3):1083–1103.

Graves, R. W. and Pitarka, A. (2010). Broadband ground-motion simulation using a hybrid approach. *Bulletin of the Seismological Society of America*, 100(5A):2095–2123.

GSM (1999). Grupo de Sismología de Medellín: Instrumentación y microzonificación sísmica del área urbana de medellín. Technical report, Sistema Municipal Para la Prevención y Atención de Desastres, Alcaldía de Medellín.

GSM (2006). Grupo de Sismología de Medellín: Microzonificación sísmica detallada de los municipios de Barbosa, Girardota, Copacabana, Sabaneta, La Estrella, Caldas y Envigado. Technical report, Area Metropolitana del Valle de Aburrá.

Haber, E., Holtham, E., Granek, J., Marchant, D., Oldenburg, D., Schwarzbach, C., and Shekhtman, R. (2012). *An adaptive mesh method for electromagnetic inverse problems*, chapter 117, pages 1–6. SEG Technical Program Expanded Abstracts 2012.

Hartzell, S., Cranswick, E., Frankel, A., Carver, D., and Meremonte, M. (1997). Variability of site response in the Los Angeles urban area. *Bulletin of the Seismological Society of America*, 87(6):1377–1400.

Hartzell, S. H., Carver, D. L., and King, K. W. (1994). Initial investigation of site and topographic effects at Robinwood Ridge, California. *Bulletin of the Seismological Society of America*, 84(5):1336–1349.

Hayashi, K., Burns, D. R., and Toksöz, M. N. (2001). Discontinuous-grid finite-difference seismic modeling including surface topography. *Bulletin of the Seismological Society of America*, 91(6):1750–1764.

Hough, S. E., Yong, A., Altidor, J. R., Anglade, D., Given, D., and Mildor, S.-L. (2011). Site characterization and site response in Port-au-Prince, Haiti. *Earthquake Spectra*, 27(S1):S137–S155.

Hudson, J. (1967). Scattered surface waves from a surface obstacle. *Geophysical Journal of the Royal Astronomical Society*, 13(4):441–458.

Hudson, J. and Boore, D. (1980). Comments on 'scattered surface waves from a surface obstacle' by J.A Hudson. *Geophysical Journal of the Royal Astronomical Society*, 60(1):123–127.

Ichimura, T., Hori, M., and Kuwamoto, H. (2007). Earthquake motion simulation with multiscale finite-element analysis on hybrid grid. *Bulletin of the Seismological Society of America*, 97(4):1133–1143.

Kamalian, M., Gatmiri, B., and Sohrabi-Bidar, A. (2003). On time-domain two-dimensional site response analysis of topographic structures by BEM. *Journal of seismology and earthquake engineering*, 5(2):35–45.

Kamalian, M., Gatmiri, B., Sohrabi-Bidar, A., and Khalaj, A. (2007). Amplification pattern of 2D semi-sine-shaped valleys subjected to vertically propagating incident waves. *Communications in Numerical Methods in Engineering*, 23(9):871–887.

Kamalian, M., Sohrabi-Bidar, A., Razmkhah, A., Taghavi, A., and Rahmani, I. (2008). Considerations on seismic microzonation in areas with two-dimensional hills. *Journal of Earth System Science*, 117(2):783–796.

Kawase, H. and Aki, K. (1990). Topography effect at the critical SV-wave incidence: Possible explanation of damage pattern by the Whittier Narrows, California, earthquake of 1 October 1987. *Bulletin of the Seismological Society of America*, 80(1):1–22.

Kellogg, J. N. and Vega, V. (1995). Tectonic development of Panama, Costa Rica, and the Colombian andes: Constraints from global positioning system geodetic studies and gravity. *Geological Society of America special paper*, 295:75.

Kim, H. J. and Swan, C. C. (2003). Algorithms for automated meshing and unit cell analysis of periodic composites with hierarchical tri-quadratic tetrahedral elements. *International journal for numerical methods in engineering*, 58(11):1683–1711.

Koketsu, K., Fujiwara, H., and Ikegami, Y. (2004). Finite-element simulation of seismic ground motion with a voxel mesh. *Pure and Applied Geophysics*, 161(11-12):2183–2198.

Komatitsch, D., Liu, Q., Tromp, J., Süss, P., Stidham, C., and Shaw, J. H. (2004). Simulations of ground motion in the Los Angeles basin based upon the spectral-element method. *Bulletin of the Seismological Society of America*, 94(1):187–206.

Komatitsch, D. and Tromp, J. (2002a). Spectral-element simulations of global seismic wave propagationI. Validation. *Geophysical Journal International*, 149(2):390–412.

Komatitsch, D. and Tromp, J. (2002b). Spectral-element simulations of global seismic wave propagationII. Three-dimensional models, oceans, rotation and self-gravitation. *Geophysical Journal International*, 150(1):303–318.

Komatitsch, D., Tsuboi, S., and Tromp, J. (2005). The spectral-element method in seismology. *Seismic Earth*, pages 205–227.

Komatitsch, D. and Vilotte, J.-P. (1998). The spectral element method: An efficient tool to simulate the seismic response of 2D and 3D geological structures. *Bulletin of the Seismological Society of America*, 88(2):368–392.

Kroonenberg, S. (1980). Petrografía y edad de algunos Neises Cordieríticos del Guainía. *Amazonia Colombiana: Revista CIAF*, 5:213–218.

Lan, H. and Zhang, Z. (2011). Three-dimensional wave-field simulation in heterogeneous transversely isotropic medium with irregular free surface. *Bulletin of the Seismological Society of America*, 101(3):1354–1370.

LeBrun, B., Hatzfeld, D., Bard, P., and Bouchon, M. (1999). Experimental study of the ground motion on a large scale topographic hill at Kitherion (Greece). *Journal of seismology*, 3(1):1–15.

Lee, S., Komatitsch, D., Huang, B., and Tromp, J. (2009a). Effects of topography on seismic-wave propagation: An example from northern Taiwan. *Bulletin of the Seismological Society of America*, 99(1):314–325.

Lee, S.-J., Chan, Y.-C., Komatitsch, D., Huang, B.-S., and Tromp, J. (2009b). Effects of realistic surface topography on seismic ground motion in the Yangminshan region of Taiwan based upon the spectral-element method and LiDAR DTM. *Bulletin of the Seismological Society of America*, 99(2A):681–693.

Lee, S.-J., Chen, H.-W., Liu, Q., Komatitsch, D., Huang, B.-S., and Tromp, J. (2008). Three-dimensional simulations of seismic-wave propagation in the Taipei basin with realistic topography based upon the spectral-element method. *Bulletin of the Seismological Society of America*, 98(1):253–264.

Lovati, S., Bakavoli, M., Massa, M., Ferretti, G., Pacor, F., Paolucci, R., Haghshenas, E., and Kamalian, M. (2011). Estimation of topographical effects at Narni ridge (Central Italy): comparisons between experimental results and numerical modelling. *Bulletin of Earthquake Engineering*, 9(6):1987–2005.

Luzón, F., Sánchez-Sesma, F., Rodríguez-Zúñiga, J., Posadas, A., García, J., Martin, J., Romacho, M., and Navarro, M. (1997). Diffraction of P, S and Rayleigh waves by three-dimensional topographies. *Geophysical Journal International*, 129(3):571–578.

Lysmer, J. and Kuhlemeyer, R. L. (1969). Finite dynamic model for infinite media. *J Eng Mech Div-ASCE*, 95(EM4):859–877.

Ma, S., Archuleta, R. J., and Page, M. T. (2007). Effects of large-scale surface topography on ground motions, as demonstrated by a study of the San Gabriel mountains, Los Angeles, California. *Bulletin of the Seismological Society of America*, 97(6):2066–2079.

Magistrale, H., Olsen, K., and Pechmann, J. (2008). Construction and verification of a Wasatch Front community velocity model: Collaborative research with San Diego State University and the University of Utah. *US Geol. Surv. Final Tech. Rept. Submitted to NEHRP*.

Malavé, G. and Suárez, G. (1995). Intermediate-depth seismicity in northern Colombia and western Venezuela and its relationship to Caribbean plate subduction. *Tectonics*, 14(3):617–628.

Maufroy, E., Cruz-Atienza, V., and Gaffet, S. (2012). A robust method for assessing 3-D topographic site effects: A case study at the LSBB underground laboratory, France. *Earthquake Spectra*, 28(3):1097–1115.

Maya, M. and Gonzales, H. (1995). Unidades litodémicas en la Cordillera Central de Colombia. *Boletín Geológico*, 35:43–57.

McCourt, W., Aspden, J., and Brook, M. (1984). New geological and geochronological data from the Colombian Andes: continental growth by multiple accretion. *Journal of the Geological Society*, 141(5):831–845.

Menouillard, T., Réthoré, J., Combescure, A., and Bung, H. (2006). Efficient explicit time stepping for the eXtended Finite Element Method (x-fem). *International Journal for Numerical Methods in Engineering*, 68(9):911–939.

Moczo, P. and Bard, P.-Y. (1993). Wave diffraction, amplification and differential motion near strong lateral discontinuities. *Bulletin of the Seismological Society of America*, 83(1):85–106.

Moczo, P., Kristek, J., Galis, M., Pazak, P., and Balazovjech, M. (2007a). The finite-difference and finite-element modeling of seismic wave propagation and earthquake motion. *Acta Physica Slovaca.*, 57(2):177–406.

Moczo, P., Robertsson, J. O., and Eisner, L. (2007b). The finite-difference time-domain method for modeling of seismic wave propagation. *Advances in Geophysics*, 48:421–516.

Moës, N., Cloirec, M., Cartraud, P., and Remacle, J.-F. (2003). A computational approach to handle complex microstructure geometries. *Computer methods in applied mechanics and engineering*, 192(28):3163–3177.

Moës, N., Dolbow, J., and Belytschko, T. (1999). A finite element method for crack growth without remeshing. *International Journal for Numerical Methods in Engineering*, 46:131–150.

Mogi, H. and Kawakami, H. (2007). Analysis of scattered waves on ground with irregular topography using the direct boundary element method and Neumann series expansion. *Bulletin of the Seismological Society of America*, 97(4):1144–1157.

Mohammadi, S. (2008). *Extended finite element method: For fracture analysis of structures*. John Wiley & Sons.

Nava, S. J., Munsey, J. W., and Johnston, A. C. (1989). First fault plane identification in the Southern Appalachians: The mbLg Vonore, Tennessee, earthquake of March 27, 1987. *Seismological Research Letters*, 60(3):119–129.

Nguyen, K.-V. and Gatmiri, B. (2007). Evaluation of seismic ground motion induced by topographic irregularity. *Soil dynamics and earthquake engineering*, 27(2):183–188.

NSR-10 (2010). *Reglamento Colombiano de Construcción Sismo Resistente. NSR-10.* Ley 400 de 1997.

Olsen, K. B. and Archuleta, R. J. (1996). Three-dimensional simulation of earthquakes on the Los Angeles fault system. *Bulletin of the Seismological Society of America*, 86(3):575–596.

Paolucci, R. (2002). Amplification of earthquake ground motion by steep topographic irregularities. *Earthquake engineering & structural dynamics*, 31(10):1831–1853.

París, G., Machette, R., Dart, R., and Haller, K. (2000). Database and map of Quaternary faults and folds of Colombia and its offshore regions, Open–file Report 00–0284: http. *pubs. usgs. gov/of/2003/opf-00-0284*.

Park, J. H., Choo, J. F., and Cho, J.-R. (2013). Dynamic soil-structure interaction analysis for complex soil profiles using unaligned mesh generation and nonlinear modeling approach. *KSCE Journal of Civil Engineering*, 17(4):753–762.

Park, S. and Elrick, S. (1998). Predictions of shear-wave velocities in southern California using surface geology. *Bulletin of the Seismological Society of America*, 88(3):677–685.

Pedersen, H., Le Brun, B., Hatzfeld, D., Campillo, M., and Bard, P. (1994). Ground-motion amplitude across ridges. *Bulletin of the Seismological Society of America*, 84(6):1786–1800.

Pelties, C., Käser, M., Hermann, V., and Castro, C. E. (2010). Regular versus irregular meshing for complicated models and their effect on synthetic seismograms. *Geophysical Journal International*, 183(2):1031–1051.

Pennington, W. D. (1981). Subduction of the eastern Panama Basin and seismotectonics of northwestern South America. *Journal of Geophysical Research, B: Solid Earth*, 86(B11):10753–10770.

Pischiutta, M., Cultrera, G., Caserta, A., Luzi, L., and Rovelli, A. (2010). Topographic effects on the hill of Nocera Umbra, central Italy. *Geophysical Journal International*, 182(2):977–987.

Pitarka, A., Irikura, K., Iwata, T., and Sekiguchi, H. (1998). Three-dimensional simulation of the near-fault ground motion for the 1995 Hyogo-Ken Nanbu (Kobe), Japan, earthquakes. *Bulletin of the Seismological Society of America*, 88(2):428–440.

Pulido, N. (2003). Seismotectonics of the northern Andes (Colombia) and the development of seismic networks. *Bull Int Inst Seismol Earthq Eng*, pages 69–76.

Quinay, P., Ichimura, T., and Hori, M. (2012). Waveform inversion for modeling three-dimensional crust structure with topographic effects. *Bulletin of the Seismological Society of America*, 102(3):1018–1029.

Ramírez, J. E. (1975). Historia de los terremotos en Colombia. *Documentación Geográfica*.

Reinoso, E., Wrobel, L., and Power, H. (1997). Three-dimensional scattering of seismic waves from topographical structures. *Soil Dynamics and Earthquake Engineering*, 16(1):41–61.

Restrepo, J. and Toussaint, J. (1988). Terranes and continental accretion in the Colombian Andes. *Episodes*, 11(3):189–193.

Rozycki, P., Moës, N., Bechet, E., and Dubois, C. (2008). X-FEM explicit dynamics for constant strain elements to alleviate mesh constraints on internal or external boundaries. *Computer Methods in Applied Mechanics and Engineering*, 197(5):349–363.

Sánchez-Sesma, F. J. (1983). Diffraction of elastic waves by three-dimensional surface irregularities. *Bulletin of the Seismological Society of America*, 73(6A):1621–1636.

Sánchez-Sesma, F. J. (1985). Diffraction of elastic SH waves by wedges. *Bulletin of the Seismological Society of America*, 75(5):1435–1446.

Sánchez-Sesma, F. J. and Campillo, M. (1991). Diffraction of P, SV, and Rayleigh waves by topographic features: A boundary integral formulation. *Bulletin of the Seismological Society of America*, 81(6):2234–2253.

Sato, T., Graves, R. W., and Somerville, P. G. (1999). Three-dimensional finite-difference simulations of long-period strong motions in the Tokyo metropolitan area during the 1990 Odawara earthquake (M_J 5.1) and the great 1923 Kanto earthquake (M_S 8.2) in Japan. *Bulletin of the Seismological Society of America*, 89(3):579–607.

Satoh, T., Kawase, H., and Sato, T. (1995). Evaluation of local site effects and their removal from borehole records observed in the Sendai region, Japan. *Bulletin of the Seismological Society of America*, 85(6):1770–1789.

Seriani, G. (1998). 3-D large-scale wave propagation modeling by spectral element method on Cray T3E multiprocessor. *Comput Method Appl M*, 64(12):235247.

Seriani, G. and Priolo, E. (1994). Spectral element method for acoustic wave simulation in heterogeneous media. *Finite Elem Anal Des*, 16(3-4):337–348.

Sohrabi-Bidar, A. and Kamalian, M. (2013). Effects of three-dimensionality on seismic response of Gaussian-shaped hills for simple incident pulses. *Soil Dynamics and Earthquake Engineering*, 52:1–12.

Sohrabi-Bidar, A., Kamalian, M., and Jafari, M. (2009). Time-domain BEM for three-dimensional site response analysis of topographic structures. *International journal for numerical methods in engineering*, 79(12):1467–1492.

Sohrabi-Bidar, A., Kamalian, M., and Jafari, M. K. (2010). Seismic response of 3-D Gaussian-shaped valleys to vertically propagating incident waves. *Geophysical Journal International*, 183(3):1429–1442.

Spudich, P., Hellweg, M., and Lee, W. H. K. (1996). Directional topographic site response at Tarzana observed in aftershocks of the 1994 Northridge, California, earthquake: Implications for mainshock motions. *Bulletin of the Seismological Society of America*, 86(1B):S193–S208.

Strouboulis, T., Copps, K., and Babuska, I. (2000). The generalized finite element method: An example of its implementation and illustration of its performance. *International Journal for Numerical Methods in Engineering*, 47(8):1401–1417.

Stupazzini, M., Paolucci, R., and Igel, H. (2009). Near-fault earthquake ground-motion simulation in the Grenoble Valley by a high-performance spectral element code. *Bulletin of the Seismological Society of America*, 99(1):286–301.

Sukumar, N., Chopp, D., Moës, N., and Belytschko, T. (2001). Modeling holes and inclusions by level sets in the extended finite-element method. *Comput Method Appl M*, 190(46):6183–6200.

Süss, M. P. and Shaw, J. H. (2003). P wave seismic velocity structure derived from sonic logs and industry reflection data in the Los Angeles basin, California. *Journal of Geophysical Research, B: Solid Earth*, 108(B3).

Taboada, A., Dimaté, C., and Fuenzalida, A. (1998). Sismotectónica de Colombia: Deformación continental activa y subducción. *Física de la Tierra*, (10):111–148.

Taboada, A., Rivera, L. A., Fuenzalida, A., Cisternas, A., Philip, H., Bijwaard, H., Olaya, J., and Rivera, C. (2000). Geodynamics of the northern andes: Subductions and intracontinental deformation (Colombia). *Tectonics*, 19(5):787–813.

Taborda, R. and Bielak, J. (2013). Ground-motion simulation and validation of the 2008 Chino hills, California, Earthquakes. *Bulletin of the Seismological Society of America*, 103(1):131–156.

Toulemonde, C., Masson, R., and El Gharib, J. (2008). Modeling the effective elastic behavior of composites: A mixed finite element and homogenisation approach. *Comptes Rendus Mécanique*, 336(3):275–282.

Trifunac, M. D. (2012). Earthquake response spectra for performance based designa critical review. *Soil Dynamics and Earthquake Engineering*, 37:73–83.

Trifunac, M. D. and Hudson, D. E. (1971). Analysis of the Pacoima dam accelerogram – San Fernando, California, earthquake of 1971. *Bulletin of the Seismological Society of America*, 61(5):1393–1411.

Tsaur, D. (2011). Scattering and focusing of SH waves by a lower semielliptic convex topography. *Bulletin of the Seismological Society of America*, 101(5):2212–2219.

Tsaur, D. and Chang, K. (2009). Scattering and focusing of SH waves by a convex circular-arc topography. *Geophysical Journal International*, 177(1):222–234.

Tu, T., Yu, H., Ramirez-Guzman, L., Bielak, J., Ghattas, O., Ma, K.-L., and O'Hallaron, D. R. (2006). From mesh generation to scientific visualization: An end-to-end approach to parallel supercomputing. In *Proceedings of the 2006 ACM/IEEE conference on Supercomputing*, page 91. ACM.

Tucker, B., King, J., Hatzfeld, D., and Nersesov, I. (1984). Observations of hard-rock site effects. *Bulletin of the Seismological Society of America*, 74(1):121–136.

Vargas, C. A., Pujades, L. G., and Montes, L. (2007). Seismic structure of south-central Andes of Colombia by tomographic inversion. *Geofísica internacional*, 46(2):117–127.

Wald, D. J., Heaton, T. H., and Hudnut, K. W. (1996). The slip history of the 1994 Northridge, California, earthquake determined from strong-motion, teleseismic, GPS, and leveling data. *Bulletin of the Seismological Society of America*, 86(1B):S49–S70.

Wills, C., Petersen, M., Bryant, W., Reichle, M., Saucedo, G., Tan, S., Taylor, G., and Treiman, J. (2000). A site-conditions map for California based on geology and shear-wave velocity. *Bulletin of the Seismological Society of America*, 90(6B):S187–S208.

Zhang, W. and Chen, X. (2006). Traction image method for irregular free surface boundaries in finite difference seismic wave simulation. *Geophysical Journal International*, 167(1):337–353.

Zhang, W., Zhang, Z., and Chen, X. (2012). Three-dimensional elastic wave numerical modelling in the presence of surface topography by a collocated-grid finite-difference method on curvilinear grids. *Geophysical Journal International*, 190(1):358–378.

Zhou, H. and Chen, X. (2006). A new approach to simulate scattering of SH waves by an irregular topography. *Geophysical Journal International*, 164(2):449–459.

Zohdi, T. and Wriggers, P. (2001). Aspects of the computational testing of the mechanical properties of microheterogeneous material samples. *International Journal for Numerical Methods in Engineering*, 50(11):2573–2599.

Zohdi, T. I. and Wriggers, P. (2008). *An introduction to computational micromechanics*, volume 20. Springer.